A Comparison of Methods for the Registration of Tractographic Fibre Images

by

Dan Golding

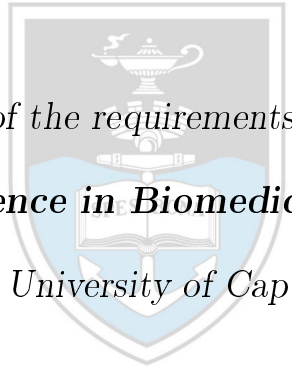

In fulfilment of the requirements for the degree

Master of Science in Biomedical Engineering

at the University of Cape Town

Medical Imaging Research Unit,
University of Cape Town Medical Campus,
Cape Town, South Africa.

Supervisor: Prof. T. Douglas

March 2011

Declaration

I, Dan Golding, hereby declare that the work on which this dissertation/thesis is based is my original work (except where acknowledgements indicate otherwise) and that neither the whole work nor any part of it has been, is being, or is to be submitted for another degree in this or any other university.

I empower the university to reproduce for the purpose of research either the whole or any portion of the contents in any manner whatsoever.

Signature: .....
D. Golding

Date: .....

Abstract

Diffusion tensor imaging (DTI) and tractography have opened up new avenues in neuroscience and are allowing previously unexplored areas of neuroanatomy and function to be researched. The tractographic fibre images that result from tractography have found applications in, amongst others, surgical planning, reducing postoperative neurological deficit, the development of white matter atlases and the ability to study the relationship between structure and function in the brain by allowing researchers to image connectivity. Most of these applications require precise spatial localization of the fibre images which is achieved through image registration.

The vast majority of research and applications that use tractographic fibre images register the DTI images prior to tractography. DTI registration, which requires voxel reorientation apart from the normal spatial transformations, is an actively researched and open problem. The fibre tracking process itself accumulates errors along the tracts and thus is sensitive to small changes in the DTI images. Thus registration of the tractographic fibre images rather than the DTI images may produce more accurate and less distorted images than those produced from tractography based on registered DTI images. This study investigates available techniques for direct registration of fibre images and explores novel adaptations of these.

Registering tractographic fibres is a complex problem which has had little attention in the available literature. This work undertakes four investigations. The first is to implement a nonlinear fibre registration using the transformations from a demons based registration of the fractional anisotropy (FA) images. These transformations are in the form of displacement fields. To apply them to the fibre images, the displacement field must be interpolated as the fibre images cannot be. This is done using Delaunay triangulation to find a suitable neighbourhood of vectors from which to interpolate. The second experiment uses an affine registration rather than a nonlinear registration. The third experiment represents the bundles as volumes and finds local affine transformations for each bundle but looks into less computationally expensive alternatives to representing the bundles as probability density functions (PDF). The final experiment combines the volumetric representations of the bundles from the previous method into a single volume for each brain image. These are used to find a global affine transformation to investigate if this much simpler method produces results comparable to the local affine method.

The alignment of fibre bundles is assessed by converting each fibre volume into a binary volume. The alignments are quantified using correlation coefficients, Cohen's kappa and four volume overlap metrics. The volume-based local affine method produced the best results with an average increase in correlation of 0.13 (from 0.34 before registration) per bundle as opposed to an increase of between 0.04 and 0.06 for the global methods. Binary volumes were used instead of the PDFs for the volume-based registrations, which greatly reduced computation time. The FA-based nonlinear method was the only method to fail as it decreased alignment and distorted the individual fibres.

The paper demonstrates that a volume-based local affine registration produces the best results and that alignment can be achieved using binary volumes, rather than computationally expensive probability density functions, to represent the volumes. The use of binary volumes reduces the computation time from over a day to under a second for each bundle. The global affine approaches, though much simpler, do not achieve the same degree of alignment as the local affine method as they are unable to account for the variability of the internal structures in the human cerebral cortex.

Acknowledgements

I would like to express my sincere gratitude to the following people and organizations: To my supervisor, Prof. Tania Douglas, for her support and guidance, and to Dr. Alfred Anwander and Dr. Marc Tittgemeyer for their advice and for providing the experimental data. To the Council for Scientific and Industrial Research (CSIR) South Africa for their generous funding. To the University of Cape Town, the Max-Planck Institute for Neurological Research in Cologne, Germany and the Max-Planck Institute for Human Cognitive and Brain Science in Leipzig, Germany for providing funding and facilities. Without these people and organizations this project would not have been possible and so I extend my sincere thanks to them all. I would also like to thank Carla Goldstein for proofreading the draft.

Contents

List of Figures

List of Tables

Chapter 1

Introduction

1.1 Problem Statement

Diffusion tensor imaging (DTI) is a relatively new magnetic resonance imaging (MRI) modality (Basser *et al.*, 1994) and is the first technique that allows the spatial structure of neuronal fibres, forming the white matter of the cerebrum, to be visualized in vivo (O'Donnell and Westin, 2007; Leemans, 2010). This is achieved via an estimation technique known as tractography, the process of tracking fibres from a DTI image. DTI images are voxel-based with tensor models stored in each voxel, while tractographic images are images of fibres described in continuous space. Although DTI can be used to image any ordered tissue fibres, the white matter in the brain, forming the connections of the various nuclei, is of particular interest as the 3D orientations of its fibres are in complex arrangements (Le Bihan *et al.*, 2001). Before DTI, the only ways to observe the morphology of white matter structures were either through post mortem dissections, which is made difficult by the complexity of white matter fibre structures, or by observing the effects of lesions in living patients, and so very little was known about the connections in the human brain (Crick and Jones, 1993). Understanding these connections is a key step to understanding brain function.

Image registration is an important and frequently used preprocessing tool in the analysis of medical images (Maintz and Viergever, 1998), including those from DTI (Xue *et al.*, 2010). Registration is the process of transforming an image to resemble another image as closely as possible (Zitova, 2003). Registration therefore spatially rearranges the voxels of an image. As DTI images have directional information associated with each voxel, the registration of these images is more complex. Aside from the voxels moving spatially, the directional information within each voxel needs to be re-oriented accordingly (Alexander *et al.*, 1999). The extent to which this affects tractography has started to be considered (Yang *et al.*, 2008; Xue *et al.*, 2010; Jia *et al.*, 2011; Ingalhalikar *et al.*, 2010) but is not yet fully understood. The vast majority of research and applications that use tractographic fibre images register the DTI images prior to tractography. The direct registration of tractographic images, i.e. images of tracked fibres, is a near untouched subject. This project aims to investigate the few attempts that have performed registration directly on the tracked fibre images (Leemans *et al.*, 2006; Ziyan *et al.*, 2007; Mayer and Greenspan, 2008; Shadmi *et al.*, 2010) and experiment with untried methods.

1.2 Motivation

The ability to image white matter fibre orientation in vivo has many practical implications. DTI gives more detailed structural information than conventional MRI does for white matter (Mori, 2007, Ch.4). This means that in cases of white matter deformation such as in brain tumour patients, DTI provides information about the shapes and locations of white matter structures that conventional MRI cannot. DTI has found a variety of clinical applications such as the evaluation of suspected ischemic stroke and diagnosis of pyogenic infections, masses and trauma associated with white matter (Mukherjee *et al.*, 2008*a*). The information provided by tractography is essential to fields such as surgical planning and to minimize postoperative neurological deficit (Maddah *et al.*, 2008; Merhof *et al.*, 2004). DTI provides researchers with a powerful new tool to build white matter atlases and models (Johansen-Berg and Behrens, 2006; Mori *et al.*, 2008) as well as to study brain development and aging (Maddah *et al.*, 2008). It is also the first technology that will allow for the study of the relationship between structure and function in the brain (Mukherjee *et al.*, 2008*a*; Schlösser *et al.*, 2007).

There is already much clinical work and research making use of tractographic images produced from *registered* DTI images (O'Donnell and Westin, 2007; Ciccarelli *et al.*, 2008; Danielian *et al.*, 2010; Okada *et al.*, 2006; Müller *et al.*, 2009; Hodaie *et al.*, 2010). Tractography is a fragile process in that small changes to a voxel of a DTI image will be amplified along the rest of the tracked fibre (Johansen-Berg and Behrens, 2009, Ch.15; Mori, 2007, Ch.9). This makes tractography very sensitive to initial conditions, which are altered by the registration process. Fibre tracking is not robust to deviations caused by noise, or the changes made by registration to the DTI images. DTI registration is still an open field and registration accuracy is affected by re-orientation and interpolation algorithms that are showing promising results but are not yet perfect.

It is not clear whether the fibre images produced from unregistered DTI images are more reliable than those produced from registered images. It seems highly probable that the results of tractography are more reliable when it is performed prior to registration, as this way the conditions for choosing seed points remain unaltered and there is no extra error introduced on the directional linking of the diffusion data from voxel to voxel. This implies that a registration performed after tractography, i.e. directly on the fibre images, may have less impact on the final images than if it is performed on the DTI images prior to tractography. But before this notion can be tested it is necessary to ascertain whether or not registration can be applied directly to fibre images. With as few as four available publications to the author's knowledge at the time of research, this is a field that has not been afforded enough attention in terms of research and thus is worthy of investigation. This project aims to explore different methods of registering fibre images.

1.3 Objectives

This project aims to:

1. review the available literature on registering fibre images,
2. implement different fibre registration algorithms and compare them,
3. experiment with algorithm adaptations in an attempt to find improvements.

1.4 Overview

Four experiments are undertaken in this study. The first two find nonlinear and affine registrations of fractional anisotropy (FA) images respectively using conventional methods and then reapply the transformations to the corresponding fibre images. The fibre images used are manually segmented fibre bundles. The third experiment investigates the conversion of fibre bundles to volumes in an efficient way such that these volumes may be registered to find a suitable transformation for each bundle. The final experiment combines all the volumes from experiment 3 into a single volume for each brain. These volumes are registered and this global affine registration is applied to the fibre data. Registrations are validated by looking at the volumetric similarity of the volumes derived from the fibre bundles.

Chapter 2 presents the background to the study. Chapter 3 contextualizes the project and strengthens the motivation of each experiment based on the current literature. Chapter 4 details the methods used. It begins by describing the data used for testing and then explains the methods used for the four experiments described above. The results of these investigations are presented in Chapter 5. The final chapter provides a discussion on these results and draws conclusions about the registration of tractographic fibres.

Chapter 2

Background

2.1 White Matter

Nervous tissue is classified as being either grey matter or white matter based on its visual appearance in a cadaver. The difference in colour is a result of the difference in composition of the tissue. Grey matter contains densely packed neuronal cell bodies, their dendrites and glial cells. White matter also contains glial cells but is predominately myelinated axons or nerve fibres (Johansen-Berg and Behrens, 2009, Ch.5; Sherwood, 2005, Ch.5). Functionally, the axons serve to relay signals from one neuron to the next, much like a wire conducting an electrical signal. White matter structures are groups of axons connecting functionally related areas of grey matter in the brain.

Three classes of white matter fibres in the cerebral hemispheres are distinguished by their courses and connections (Mori *et al.*, 2008; Mamata *et al.*, 2002; Reid, 1996, Ch.13) as follows:

1. *Projection fibres* are those connecting the cerebral cortex with the thalamus and the nuclei of the brain stem including:
    - The corticofugal fibres arising in cells of the frontal lobe and ending in the nuclei of the pons. Also known as the frontopontine fibres, they collectively form the corticofugal tract (CFT) (Lindberg *et al.*, 2007).
    - The anterior thalamic radiations (ATR) which connect the frontal lobe with the thalamus (Mori *et al.*, 2002).
    - The internal capsule.
    - The corona radiata.
2. *Association fibres* are connections restricted to a single hemisphere. This class of fibres has a wide range of lengths. Noteworthy structures made of these fibres include:
    - The cingulum (CIN) which surrounds the corpus callosum (Reid, 1996, Ch.15).
    - The inferior longitudinal fasciculus (ILF) passing from the occipital lobe to the temporal lobe (Reid, 1996, Ch.15).
    - The superior longitudinal fasciculus (SLF) passing from the frontal lobe to the occipital lobe (Reid, 1996, Ch.15).

- The fasciculus uncinatus or uncinate fasciculus (UNC) which is the group of hooked fibres connecting the temporal lobe with the frontal lobe (Mamata *et al.*, 2002).
- The arcuate fasciculus (ARC) links the lateral temporal cortex with the frontal cortex via an arching dorsal projection and is involved in human language (Rilling *et al.*, 2008).
- The inferior fronto-occipital fasciculus (IFO), also known as the occipitofrontal fasciculus, passes backwards from the frontal lobe into the occipital and temporal lobes (Wakana *et al.*, 2004; Mori *et al.*, 2002).

3. *Commissural fibres* connect similar parts of the two hemispheres. Important commissural structures are:
   - The corpus callosum (CC) connecting a large portion of the medial surfaces of the hemispheres (Reid, 1996, Ch.15).
   - The anterior commissure and the posterior commissure. These are often used as landmarks to find the midsagittal plane (O'Donnell and Westin, 2007).
   - The habenular commissure.
   - The optic chiasma.

The above fibre examples are of anatomical regions. When dealing with tractography data it can be more useful to segment the brain into tracts. Where a region is a special area of white matter, a tract is the white matter connecting two anatomical regions. These definitions are not always clearly separated in the field of white matter anatomy (Mori *et al.*, 2008). There are advantages to both ways of viewing white matter. Important examples of tracts are the *corticospinal tract* and the *cerebellar peduncles*.

Damage to these white matter structures due to trauma, tumours, strokes or pathologies like multiple sclerosis have severe implications and are associated with high morbidity and mortality rates, making white matter an important area in medical research. The difficulties in imaging white matter in the past, especially in living subjects, has restricted research both into the function of white matter tracts and into the symptoms of damage to them. Diffusion tensor imaging is an important new technique and has already made significant impact in white matter research (Johansen-Berg and Behrens, 2006; Lindberg *et al.*, 2007; Sundgren *et al.*, 2004).

2.2 Diffusion Tensor Imaging and Tractography

This section will present a brief background into the mechanisms and uses of DTI and tractography. DTI cannot be understood without first understanding conventional MRI. For a more complete explanation of the technologies, readers are referred to the works of Hashemi *et al.* (2010) and Mori (2007).

2.2.1 Magnetic Resonance Imaging

Magnetic resonance imaging is a widely used and important medical imaging technique. Its ability to offer high contrast images of soft tissue, such as muscle or the nervous tissue of the brain, offers a productive complement to x-rays and CT-scans which are used

to image hard tissue such as bone. MRI utilizes the phenomenon of nuclear magnetic resonance (NMR) to image the interior of the body non-invasively. This section will first present the physics of NMR and then show how this is used for image formation.

2.2.1.1 Nuclear Magnetic Resonance

When magnetic nuclei are exposed to an external magnetic field and an applied electromagnetic pulse, the nuclei will absorb energy and radiate it. This property of matter is known as NMR. The most common nuclei in the human body are the protons of the hydrogen atoms in water molecules. Although NMR is not exclusively exhibited by these protons, they are the particles used for MRI and will be the only particles considered in this section.

All elementary particles have a fundamental property known as spin. Spin was originally thought of as being a rotation of the particle about its own axis, much like the rotation of the earth (Andrew, 2009). Although this analogy is lacking, it is a convenient way to visualize the quantum phenomenon. Protons either have a spin quantum number of $\frac{1}{2}$ or $-\frac{1}{2}$, also known as up and down respectively. We can treat these as rotations in opposite directions. This spin creates a magnetic dipole moment (MDM) for each proton. The axes of proton spins in tissue have random orientations under normal circumstances, however, when exposed to a strong external magnetic field, referred to as B_0, they line up with the direction of the field. Roughly half will be parallel to the field and half will be antiparallel and thus the resultant magnetic field due to the MDMs will be zero. Over time a fraction of the antiparallel MDMs, only about one per million, will flip and become parallel to the external magnetic field. This causes the tissue to magnetize over time, slowly increasing towards a maximum. This is because the down state is at a slightly higher energy level. The growth of this magnetization, M_z, is described as a function of time, t, by

$$M_z(t) = M_0(1 - e^{-t/T_1}) \tag{2.1}$$

where M_0 is the maximum magnetic field produced by the tissue and T_1 is a time constant, that is T_1 is a constant that describes the rate at which M_z approaches M_0. The reason for the subscript z is that the coordinate system used in MRI defines the direction of B_0 as the z-axis.

There is another relevant phenomenon that occurs when hydrogen is exposed to an external magnetic field. This is that the axes of the spin of the protons are not exactly aligned with B_0 but rather precess around it. This is illustrated by Figure 2.1. The frequency of precession, ω, is known as the *Larmor frequency* and is described by the *Larmor equation*:

$$\omega = \gamma B_0 \tag{2.2}$$

where γ is the gyromagnetic ratio, a constant in this case. It is important to note that M_z does not precess. This is because the spins' precessions are not in phase, as shown in Figure 2.2a, and M_z is the *net* magnetization. At this point M_z only has a component in the z direction which is termed longitudinal. The x-y-plane is known as the transverse.

Applying a radio frequency (RF) pulse at the Larmor frequency and orthogonal to B_0 has two effects. Firstly, it adds energy to the system because ω is the resonant frequency of the system. This is absorbed by the excess protons with an up spin causing them to flip to a down spin, and in doing so reduces M_z to zero over time. Secondly, it causes the spin axes to precess in phase. This effect is illustrated in Figure 2.2b. This gives the net magnetization a transverse component, M_{xy}. This means that the resultant M is

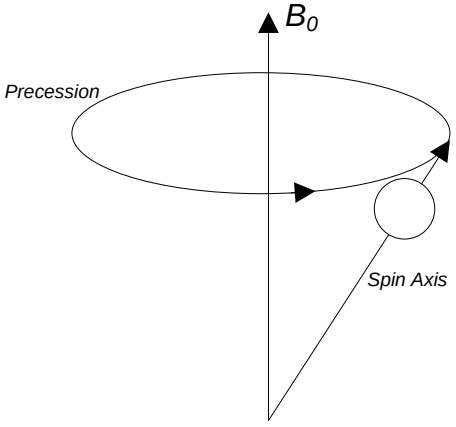

Figure 2.1: Precession of spin axis around the direction of an applied magnetic field, B_0.

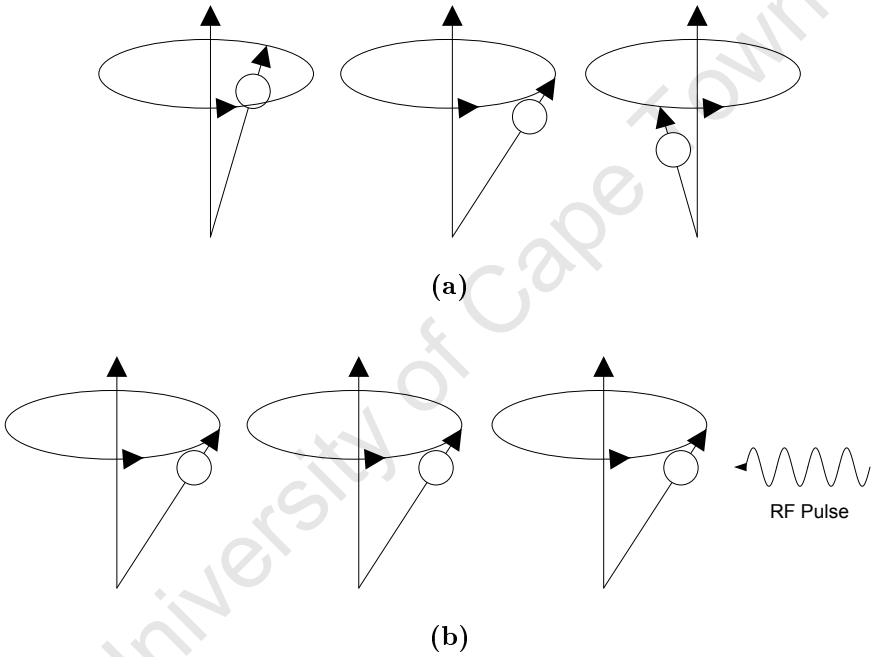

Figure 2.2: (a) The precessions of protons about the B_0 axis are out of phase. (b) When a suitable RF pulse is applied they precess in phase with one another.

now at an angle with the z-axis. This is known as the flip angle and will be represented by θ. The length of the RF pulse and its strength both have an influence on θ. It is also important to understand that θ is caused by two independent effects. These are the reduction of M_z due to the reversing of some of the spins, and the increase of M_{xy} caused by the precessions becoming in phase. It is also worth distinguishing between the angle of precession and θ which is the angle of the net magnetization caused by the cumulative effect of the precession of all the protons.

When the RF pulse stops, M_z is restored according to Equation 2.1 and M_{xy} returns to zero according to the equation:

$$M_{xy}(t) = M_0 e^{-t/T_2} \tag{2.3}$$

This gives a second time constant, T_2. The T_1 and T_2 time constants are independent

of one another. T_1 is a measure of the rate at which M_z grows whereas T_2 is the rate at which M_{xy} decreases.

Equation 2.3 shows that at the time the RF pulse is stopped, $t = 0$ in terms of the equation, there is an M_{xy} component. The signal that this component induces in the receiver coil is the MRI signal. The equations also show that this signal decreases over time. This is known as free induction decay (FID). The increase over time of M_z shown by Equation 2.1 is known as longitudinal relaxation.

2.2.1.2 MRI Image Formation

Different tissue types in the body have different inherent T_1 and T_2 values. Thus if we can weight the voxel intensities of our images by either T_1 or T_2 we can create images that contrast tissue types. The clinical application will determine if it is more appropriate to choose a T_1-weighted image or a T_2-weighted image.

In practice these time constants are not measured directly. A carefully timed sequence of RF pulses and measurements of FID are used to infer T_1 and T_2. Important parameters are T_R, the time between RF pulses, and T_E, the time between an RF pulse and the measurement of the FID. The choice of T_R and T_E determine whether the image will be T_1 or T_2 weighted.

If B_0 is left as a homogeneous field, then an RF pulse will excite the entire patient and the FID received will be from every part of the patient. This leaves the problem of spatial encoding, that is of isolating signals as a function of 3D space. This is done by creating gradients in the magnetic field.

Before understanding the gradients it is worth considering what we are trying to image. MRI can create many types of images. This explanation will use 3D MRI of the head as an example. In this case the head is aligned so that a cross section lies on the x-y-plane. In other words a line from the base of the neck to the top of the head would be parallel to the z-axis, and thus to B_0. Our gradients need to be able to localize the signal in 3 dimensions and so we need 3 gradients.

The first gradient is in the direction of B_0, i.e. along the z-axis, and is called the *slice selection* gradient. It is used to isolate the signals to a specific z value, i.e. an x-y-plane or a cross sectional slice of the patient. The gradient means that each z value of the patient has a different B value and thus according to Equation 2.2 is sensitive to a different Larmor frequency. This allows us to excite a cross section, or a *slice*, of the patient by adjusting the frequency of the RF pulse, hence the name slice selection gradient.

The slice selection gradient is turned on during the RF pulse and turned off after the pulse. A gradient in the x direction is applied during the signal acquisition. This causes each x value on the slice to produce a signal at a different frequency and so it is termed the *frequency encoding* gradient. A fourier transform of the signal thus allows spatial discrimination in the x direction. There are two options to achieve spatial information in the y direction. Either through a back projection process similar to CT scans, or by applying a *phase encoding* gradient in the y direction. The image prior to the fourier transform is said to be in *K-space*.

A *pulse sequence* is the timing sequence of RF pulses and gradients used to traverse spatial coordinates of the patient. There are many different pulse sequences but as this is a simple introduction to MRI, an explanation of pulse sequences will not be presented. For this, readers are referred to Bernstein *et al.* (2004).

2D cross sectional examples of both a T_1-weighted image and a T_2-weigthed image are shown in Figure 2.6 in Section 2.2.2. These images show the contrast between different

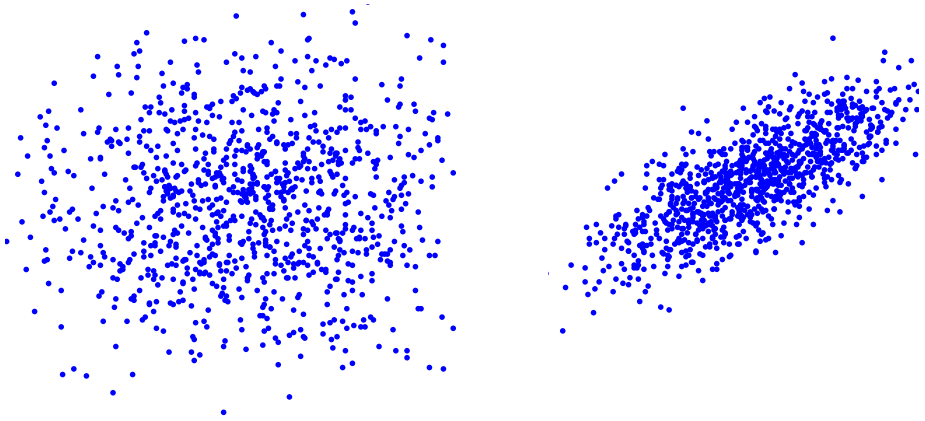

(a) (b)

Figure 2.3: Matlab simulations of (a) isotropic diffusion and (b) anisotropic diffusion.

types of tissue and even to some extent between white and grey matter. They offer no information about the orientation and direction of the fibrous structure of tissue. DTI extends conventional MRI making it possible to image this structural information.

2.2.2 Diffusion Imaging

2.2.2.1 Diffusion and Anisotropy

Diffusion tensor magnetic resonance imaging, or simply diffusion tensor imaging, enhances conventional MRI, enabling it to image the 3D structure of fibrous tissue by taking advantage of water diffusion. Water diffusion is the thermally driven, random walk type motion of water molecules (Beaulieu, 2002). It is isotropic, that is water has an equal likelihood of diffusing in any direction, assuming motion is uninhibited. Cell membranes are permeable to water molecules, but the movement of a water molecule across a cell membrane is slightly inhibited. This means that the likelihood of water diffusing across a cell membrane is slightly lower than in any other direction. This makes the diffusion of water in tissue consisting of long, thin cells anisotropic (Jellison *et al.*, 2004). Water diffusing in tissue of this sort will have a higher rate of diffusion in the direction of the cell bodies and a lower rate across them. Thus the rate of water diffusion can be used to model the structure of fibrous tissue. Figure 2.3 illustrates the difference between isotropic and anisotropic diffusion. Myelin is a major inhibitor of diffusion (Beaulieu, 2002), and its presence in white matter makes the tissue a suitable candidate for DTI studies.

DTI produces images with voxel resolution in the order of mm^3, whereas the diameter of myelinated fibres is between $3\mu m$ and $12\mu m$ (Jacobs and Love, 1985). As thousands of axons pass through each voxel, gaining useful information about cellular structure appears beyond the capabilities of DTI. However, water diffusion occurs on at scale small enough to probe cellular structure. The information stored in each voxel of a DTI image can be thought of as a statistical sampling, performed by the water molecules, of the cellular arrangement of the tissue of that voxel. This is how DTI can infer information about structures far beyond the minimum scales that its resolution should allow.

The fact that each voxel represents such a statistical sampling has another important implication. That is that DTI is not a deterministic or precise imaging of cellular structure. DTI provides aggregate information for thousands of cells per voxel, and this

information is based on a stochastic process. This is an important fact to bear in mind when viewing or analysing DTI images and their derivatives, particularly those of deterministic tractography as presented in Section 2.2.3, as these images look deceptively like the trajectories of the individual axons themselves.

2.2.2.2 Diffusion Weighted Imaging

DTI images summarize these *statistical samplings* of cellular structure by fitting a tensor model to each voxel. Before this can be done, an imaging process called diffusion-weighted imaging (DWI) is needed. A DWI image, in contrast to T_1 or T_2-weighted images, is an image in which each voxel represents the component of the rate of diffusion in one direction only. This is done by applying a diffusion gradient. At least 6 DWI images, but preferably many more, with gradients in different directions are required to build a tensor model as well as one unweighted image which is termed the b_0 image (Mukherjee *et al.*, 2008*a*).

The diffusion gradient is not the same as the gradients described in Section 2.2.1. The spatial encoding gradients are still needed and are present here, usually within either a single shot echo planar imaging (EPI) pulse sequence (Mukherjee *et al.*, 2008*b*; Mori, 2007) or a T_2 spin echo pulse sequence (Mukherjee *et al.*, 2008*a*). When a diffusion gradient, which is also a linear gradient of the external magnetic field, is applied it causes the nuclei in each slice of the image to precess at a different frequency. This means that if the spin precession of each slice began in phase, after the diffusion gradient has been applied and stopped each slice will be out of phase with the other slices. Note that slice here refers to a plane orthogonal to the diffusion gradient. This diffusion gradient is known as the dephasing gradient. A second diffusion gradient, the exact opposite of the dephasing gradient, is then applied. This is the rephasing gradient. When it stops the slices are all in phase again. There is however some *signal loss* and this is what is used to quantify diffusion. Before this is explained it is worth clarifying that the application of a dephasing gradient and a rephasing gradient create only one of the required DWI images and that each DWI image will have diffusion gradients in only one direction.

The primary source of the signal loss mentioned in the above paragraph is diffusion, specifically diffusion in the direction of the dephasing and rephasing gradients or across the slices. If the time between the dephasing and rephasing gradients is long enough, water molecules will diffuse across the slices. This means that there is now a slight inhomogeneity of phase in each slice. Said another way, any molecule that has moved into another slice has the incorrect phase for its new slice. When the rephasing gradient is applied, it will alter the phase of each molecule according to the slice it is currently in. Thus the few molecules that have diffused across slices will not return to their original phase and this accounts for the signal loss. The four stages of this process are shown in Figure 2.4. Molecules that diffused within their slice, i.e. in a direction orthogonal to the gradients, will still be in the correct plane for their phase and this will not contribute to the signal loss. The signal loss is thus a quantifiable measurement of diffusion in the direction, and only in the direction, of the applied diffusion gradient. This is the simplest of many gradient schemes that can be used for DWI. In practice more efficient methods are used but the concepts behind them are all very similar.

2.2.2.3 Diffusion Tensor Imaging

The next step is to use these DWI images to fit tensor models of diffusion direction to each voxel. The mathematics behind this is complicated but a physical interpretation as

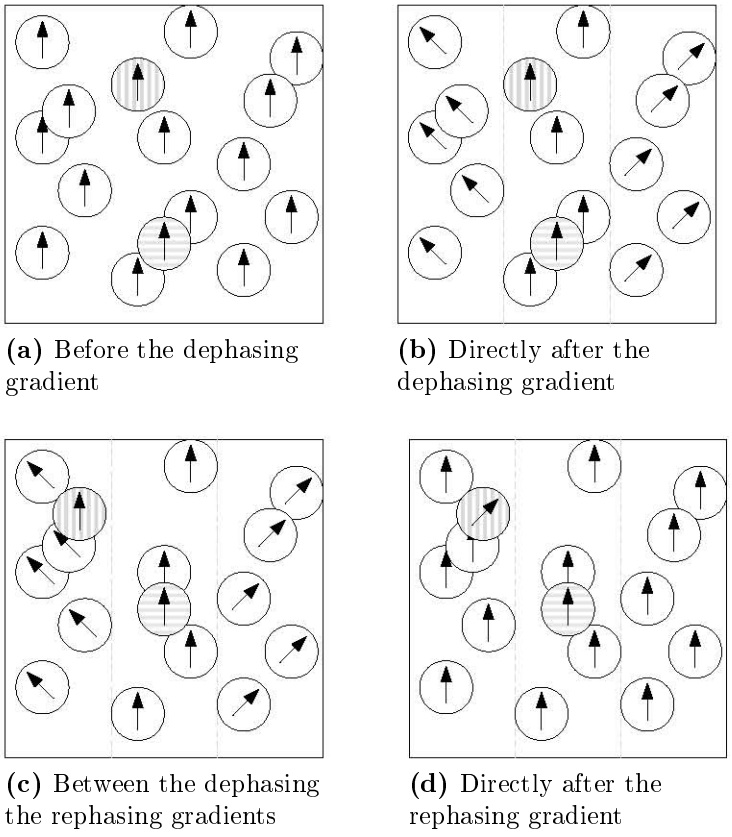

(a) Before the dephasing gradient

(b) Directly after the dephasing gradient

(c) Between the dephasing the rephasing gradients

(d) Directly after the rephasing gradient

Figure 2.4: This figure shows four stages of the diffusion gradient process. The arrow in each water molecule represents the *phase* of precession, not the direction of the external magnetic field. Two molecules have been highlighted to illustrate how gradients are used to measure diffusion. Note that none of the images occurs *during* a gradient. **(a)** All the molecules are precessing in phase. **(b)** A magnetic field gradient is applied horizontally. This is the *dephasing* gradient. The dotted vertical lines show the divisions of the slices that this gradient creates. During the gradient, the molecules precess at different frequencies. This image shows that after the gradient has stopped, although the molecules are once again all precessing at the same frequency, each slice has moved out of phase with the other slices. **(c)** This image shows the diffusion of two molecules. The top molecule is diffusing across the slices, the bottom molecule is diffusing within its slice. This occurs after the dephasing gradient but before the rephasing gradient. **(d)** A *rephasing* gradient changes the phase of each slice in the exact opposite way to the dephasing gradient. Once again, this image shows that after the rephasing gradient has stopped, all the molecules are once again in phase. However the molecule that diffused across the slices is now out of phase. This accounts for the signal loss and is how we measure diffusion. The amount the intensity of the signal has dropped is proportional to the rate of diffusion in the direction of the gradient. Note that the molecule that diffused within its slice remains at the correct phase and thus does not contribute to the signal loss. This is why each DWI only measures diffusion in the direction of the gradient.

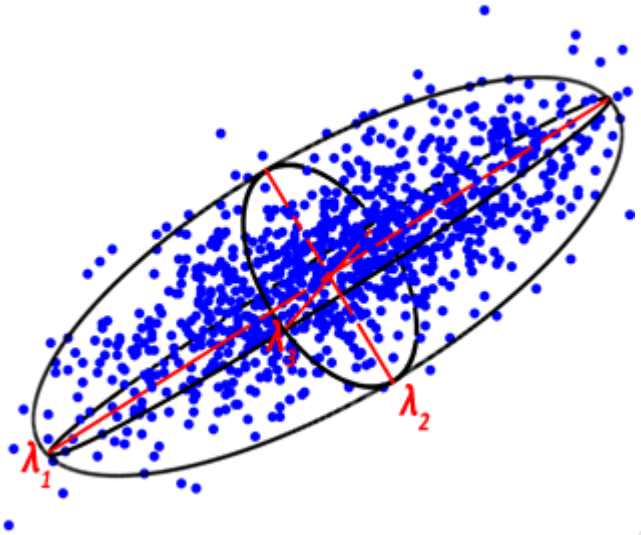

Figure 2.5: Anisotropic diffusion visualized as an ellipsoid. The three diameters describing the ellipsoid are proportional to the eigenvalues of the diffusion tensor and their directions are the same as the corresponding eigenvectors.

well as an understanding of the limitations of the tensor models can be achieved without the mathematical details. The tensor model aims to describe anisotropy. Figure 2.5 shows that the overall shape of an anisotropic diffusion can be described by an imaginary ellipsoid (Mukherjee *et al.*, 2008*a*). This is a useful interpretation of anisotropy, as the magnitude of a vector taken from the centre to an arbitrary point on the surface of the ellipsoid gives us the rate of diffusion in the direction of that vector (Jellison *et al.*, 2004).

We can see from Figure 2.5 that an ellipsoid requires 6 parameters to be completely defined: the lengths of the three diameters and their respective directions in 3D space. The tensor models are created in such a way that they have three eigenvalues, λ_1, λ_2 and λ_3, which are proportional to the lengths of the three imaginary diameters (Yang *et al.*, 2008) and that the corresponding eigenvectors, $\vec{e_1}$, $\vec{e_2}$ and $\vec{e_3}$, will have the same directions as their respective diameters (Mukherjee *et al.*, 2008*a*). To find a tensor that fits these 6 requirements, we need at least 6 DWI images measuring diffusion in 6 different directions.

We can make two very distinct classes of images from DTI namely *photometric* images and *morphometric* images (Mori, 2007, Ch.7). Photometric images are composed of voxel intensities. The image is a simple 3D spatial mapping, such as those produced by conventional MRI which are spatial mappings of the T_1 or T_2 properties of tissue. Morphometric images contain information about the size and shape of separate structures. Morphometeric images are produced from DTI through a process known as tractography which is explained in Section 2.2.3.

One of the most common types of photometric image produced from DTI images is the fractional anisotropy (FA) image. These images map anisotropy by assigning each voxel an FA value (Basser and Pierpaoli, 1996). FA measures how directional diffusion is (Mukherjee *et al.*, 2008*a*). FA is defined using the eigenvalues of the diffusion tensor according to the equation:

$$FA = \sqrt{\frac{\left((\lambda_1 - \lambda_2)^2 + (\lambda_2 - \lambda_3)^2 + (\lambda_3 - \lambda_1)^2\right)}{2\left(\lambda_1^2 + \lambda_2^2 + \lambda_3^2\right)}} \tag{2.4}$$

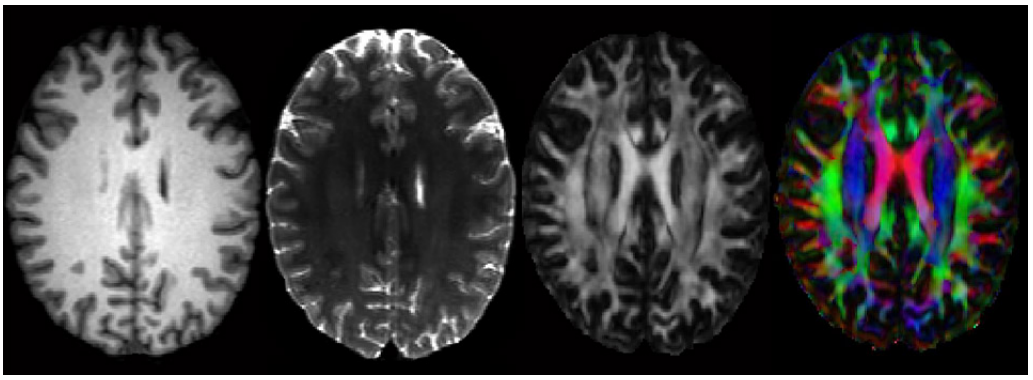

(a) (b) (c) (d)

Figure 2.6: A comparison of conventional MRI with DTI indices. (a) shows a T_1-weighted image, (b) a T_2-weighted image, (c) an FA image and (d) a DTI colour mapping.

Even though FA images lose all the directional information of the diffusion tensors, they create images with sharp contrast between white matter and grey matter. Compare the FA image in Figure 2.6c with the T_2 image of the same brain in Figure 2.6b. The FA image shows structures that are not discernable in the T_2 image.

The directional information can be visualized using photometric images known as colour mappings (Mori, 2007, Ch.7). A primary colour is used to represent each axis. Red for the medial-lateral axis, green for the anterior-posterior axis and blue for the superior-inferior axis. An image can be created by colouring each voxel according to the direction of the principle eigenvector. The intensities of the primary colours are then proportional to the component of the vector in the three directions. Thus a pure yellow would indicate a 45° direction in the cross sectional plane. The diffusion tensors are meaningless for isotropic regions and so these colour mappings should be multiplied by FA to eliminate voxels with low diffusion information. Figure 2.6 shows a comparison of colour mappings and FA images with conventional T_1-weighted and T_2-weighted MRI images.

The colour maps take the colour of the principal eigenvector, but there is not always an eigenvalue that is clearly larger than the other two. For example the ellipsoid that would model isotropic diffusion would be a sphere. Here the eigenvalues are all equal. However a sphere has zero FA and thus is not a problematic case. There are, however, ellipsoids representing categories of anisotropy with high FA. Consider an oblate spheroid. This is a sphere with one diameter reduced in length while the other two remain the same giving it a squashed or disk-like appearance. There is no principal eigenvector in this case but it is still anisotropic and thus will have a high FA. This is most likely caused by bundles of axons crossing in this voxel. A major limitation of DTI is that it cannot model crossing or branching of fibres. Furthermore, an ellipsoid might not be the best description of the diffusion. There are alternatives to the tensor model such as fitting multiple tensors per voxel (Pasternak *et al.*, 2008), high-angular resolution diffusion imaging (HARDI) (Anderson, 2005), Q-ball imaging (Tuch, 2004) and spherical deconvolution (Tournier *et al.*, 2004) that can find higher order better fitting models which can incorporate arbitrary shaped anisotropy and account for crossing and branching. They have their own drawbacks such as very high hardware and software requirements. These methods are beyond the scope of this project but are mentioned to illuminate some of the limitations of DTI which is the most commonly used method (Mori, 2007, Ch.8).

Westin *et al.* (2002) proposed an alternative to FA to account for the possibility of

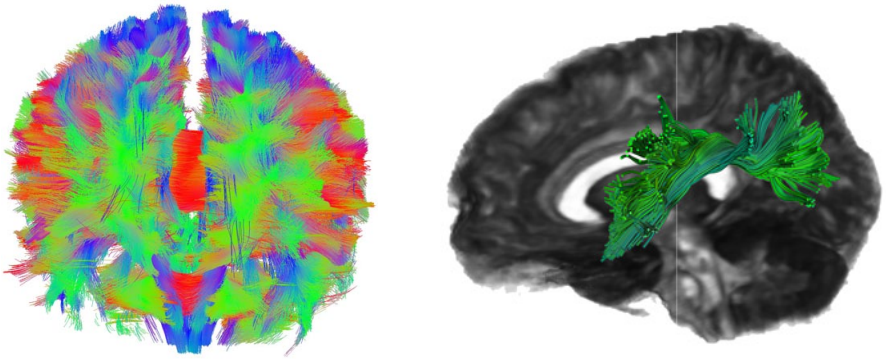

(a) (b)

Figure 2.7: Example of deterministic tractography or fibre tracking. (a) shows whole brain tractography and (b) shows a region of interest extracted from whole brain tractography superimposed over a 3D rendering of its corresponding FA image to provide a visual aid to anatomical localization. The tracking and images were produced using MedInria (Fillard *et al.*, 2007).

oblate or normal spheroids using tensors. The three so called *Westin metrics* describe how close a tensor is to the three generic cases of line, C_l, disk or plane, C_p and the isotropic case of sphere, C_s and are given by

$$C_l = \frac{\lambda_1 - \lambda_2}{\lambda_1}, \quad C_p = \frac{\lambda_2 - \lambda_3}{\lambda_1}, \quad C_s = \frac{\lambda_3}{\lambda_1} \tag{2.5}$$

2.2.3 Tractography

White matter fibres in the brain often follow convoluted trajectories. This makes it difficult to analyse their 3D structures from the 2D slice-by-slice images of DTI colour maps (Mori, 2007, Ch.9). 3D images of the fibres themselves can be constructed from the DTI information through a process known as tractography (Basser *et al.*, 2000). Figure 2.7 shows the output of deterministic tractography. The images produced by tractography are morphometric and contain the structural information of the fibres.

There are two approaches to tractography: deterministic and probabilistic. The probabilistic approach attempts to define the probability distribution of possibly connected voxels beginning at some seed point. This probability distribution is defined spatially and known as a tractogram (Anwander *et al.*, 2007). A simple probabilistic tractography method would be to first choose a seed voxel. A simulated particle is placed at this seed voxel and allowed to diffuse through the DTI image with the tensor of each voxel defining the probability of diffusion in any direction. This process is repeated thousands of time until a large enough sample of the probability distribution has been taken. Probabilistic tractography has many applications, such as quantifying the connectivity between two regions of interest or tracking in regions of low FA (Klein *et al.*, 2010*b*), but is computationally expensive and less suitable to the clinical environment (Danielian *et al.*, 2010).

This project will focus on the deterministic approach which builds fibre trajectories by following the path of maximum likelihood. This process is also called *fibre tracking* and aims to determine the structural connections between voxels implied by the diffusion tensors (Mukherjee *et al.*, 2008*a*). It creates continuous morphometric images from the discrete DTI images.

One of the simplest and more popular methods of deterministic tractography is fibre assignment by continuous tracking (FACT) (Mukherjee *et al.*, 2008*a*), or the streamline method. The discrete voxels are converted into continuous 3D trajectories by fitting curves that attempt to follow the main eigenvectors of the voxels (Mori and van Zijl, 2002). Starting at a seed voxel, the fibre direction follows the principal eigenvector of the voxel. When the fibre enters a new voxel the direction is changed to match that of the principal eigenvector of the next voxel. Interpolation techniques are used to smooth the lines as the discrete nature of DTI can result in kinks in the trajectories (Basser *et al.*, 2000). The lines are terminated either when an area of sufficiently low anisotropy (grey matter has a typical FA of 0.05 - 0.15 and so a common stopping criterion is $FA > 0.1 - 0.30$) is reached or a sharp turn (typically defined to be between 40° and 70°) is the only option (Mukherjee *et al.*, 2008*b*; Jellison *et al.*, 2004). To automate this process for the whole brain the choice of seed points is most often chosen as the boundary between white and grey matter which is defined using FA, or every voxel in the DTI image is used as a seed point.

By only considering the main eigenvector, most of the information in the diffusion tensor is discarded. Another method uses the entire tensor to deflect the incoming fibre (Lazar *et al.*, 2003). This helps to reduce the ambiguous effect caused by crossing fibres, i.e. a tensor in the disk-like shape of an oblate spheroid. If the fibre approaches an oblate spheroid in the plane of the disk it is not deflected but is if it approaches the disk at an angle. A bootstrap approach produces many different DTI images by selecting subsets from a large pool of DWI images and computes streamline tractography for each of these. The different fibre images can be combined so as to reduce the effect of noisy DTI (Mori, 2007, Ch.9). There are many other advanced fibre tracking techniques but as streamline tractography is the most widely used, these other techniques will not be considered in this work.

Although fibre tracking is a relatively new technique it has already found many applications, both clinical and in neuroscience research (Heiervang *et al.*, 2006). It has allowed clinicians and researchers to isolate and delineate major white matter pathways in vivo in individual brains (Johansen-Berg and Behrens, 2009, Ch.15). It allows clinicians to locate a pathway of interest and take quantitative measures along it, for example measuring the overlap of lesions and tract involvement (Ciccarelli *et al.*, 2008). The insights that tractography has offered into white matter anatomy and connectivity in the brain has allowed researchers to explain the symptoms of lesions. Another potential use of tractography is to image adaptive changes in the brain such as those that can occur after a stroke (Ciccarelli *et al.*, 2008). It is also used to predict the effects of surgery in epilepsy patients and to evaluate structural changes caused by this surgery. Another main area where fibre tracking is used clinically is in neurosurgical planning. Researchers have used fibre images to develop detailed white matter atlases (Mori *et al.*, 2008; O'Donnell and Westin, 2007) as well as for cortical parcellation (Anwander *et al.*, 2007). As tractography shows the connectivity between areas of the brain (Mori and Zhang, 2006), researchers are using it as a tool to better understand cortical functions with some studies combining tractography and functional MRI (Schlösser *et al.*, 2007).

Although the new images have found many applications and are proving to be extremely useful, fibre tracking has many limitations and short comings. DTI images are prone to noise and this noise creates errors that accumulate in the tracking process (Mori, 2007, Ch.9). This accumulation of error is due to the integration involved in the tracking process (Johansen-Berg and Behrens, 2009, Ch.15) and thus tracking results are greatly affected by small errors. The errors are more frequent in areas of low FA. Fibre tracts

are thus most reliable in the core of thick bundles and far less reliable at the fringes toward the grey matter border (Johansen-Berg and Behrens, 2009, Ch.15). Deterministic fibre tracking algorithms provide no measure of the uncertainty that underlies their creation such as the assumption that all fibres within a voxel are aligned with the principal eigenvector (Leemans, 2010). False positive fibres can be generated due to unrelated fibres sharing a DTI voxel. Axonal bundles exhibit branching and anastomosis which tracked fibres cannot. DTI cannot model fibre crossing and this translates into problems in tractography. Fibres either prematurely terminate at regions of fibre crossing (false negatives (Ciccarelli *et al.*, 2008)), or they can switch from one fibre to the crossing fibre. Due to these physical limitations and assumptions, fibre tracking only approximates reality. It also relies on user defined parameters such as termination conditions (Klein *et al.*, 2010*b*). Even though streamline methods are the most common, there is no consensus on a best method of tractography nor on a best practice for choosing parameters and as there is no gold standard (Johansen-Berg and Behrens, 2009, Ch.16) to compare the in vivo images against, there is much disagreement amongst researchers (Ciccarelli *et al.*, 2008).

2.3 Image Registration

Registration is the process of transforming an image to be as spatially aligned to a reference image as possible (Hill *et al.*, 2001). A widely used tool in image processing in general, registration is particularly useful in medical imaging where it finds a variety of applications. Registration algorithms define a mapping from one coordinate space to another and this mapping is stored in a transformation matrix. An optimization algorithm then iteratively finds the parameters needed for the transformation matrix such that when it is applied to the source image, it results in as similar as possible an image to the reference image. This similarity can be defined in many ways such as the absolute or square difference of the voxel intensities, the cross correlation of the images or via information theoretic approaches such as mutual information (Maintz and Viergever, 1998; Crum *et al.*, 2003). Feature-based registration can even use ordinary distance metrics.

There are three images associated with any one registration. These are the source image, the reference image and the output image. The source image, also called the input image or the moving image, is the image that is to be transformed, or registered, or warped to resemble the reference image. The reference image which is also known as the target image or the stationary image, is the goal of registration. The output image is the transformed or warped version of the source image that the registration procedure produces as an output. The output image is aligned with the reference image. Technically speaking, the output of registration is the transformation matrix. This only produces an output image when applied to the source image, but as the transformation matrix is of negligible use aside from being applied to the source image, this chapter will treat the application of the transformation matrix to the source image producing the output image as the final step of the registration procedure. The next chapters however, will consider the transformation as the output of registration. Figure 2.8 illustrates registration by showing the three images.

Registration can be classified according to the application as well as the nature of the process (Maintz and Viergever, 1998). This list demonstrates some of these distinctions:

Intra-subject or inter-subject: Images of the same subject taken at different times,

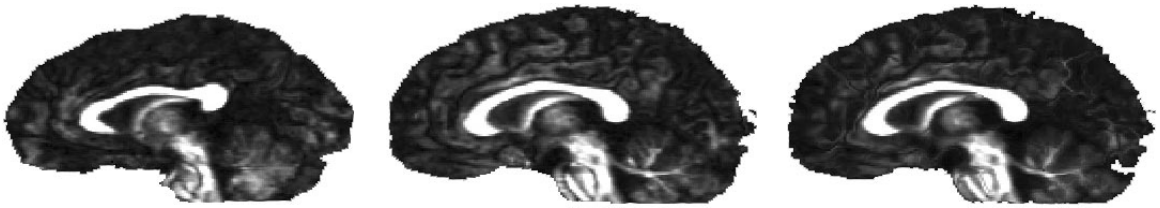

(a) (b) (c)

Figure 2.8: An example of nonlinear registration showing (a) the source image, (b) the reference image and (c) the output image.

such as those used to monitor tumour growth or the different direction DWI images needed to create a DTI image (Rohde, 2005) are cases where intra-subject registration is used. Registration of the same image taken of different subjects is known as inter-subject registration. It is less common but finds applications such as digital atlas creation (O'Donnell and Westin, 2007) or population morphology studies (Rohde, 2005).

Intra-modality or inter-modality: Registration is intra-modal when the source and target are the same type of image, however registering a CT scan with MRI is a common example of inter-modal registration. Inter-modal, or multi-modal, registrations are usually performed on images taken of the same scene using different sensors (Zitova, 2003). Intra-modal registrations often use voxel intensity difference as a similarity measure where inter-modal algorithms are more likely to employ mutual information or correlation.

Feature-based or voxel intensity-based: Feature or landmark based registration computes the similarity of the two images based on a sparse selection of anatomical landmarks (Maintz and Viergever, 1998). These landmarks can either be defined interactively or can be detected automatically. Voxel intensity-based methods use every voxel of the image to compute similarity and are completely automated. Unlike the feature based methods, these methods calculate the similarity directly from the voxel values (Hill *et al.*, 2001).

Affine or nonlinear: Affine registration defines a 12 parameter mapping[1]. The transformation is restricted to translation, rotation, scaling and shearing. Nonlinear registration has far more parameters ranging up to one parameter for every voxel of the image. Technically speaking, affine transformations are also not linear and it would be more correct to refer to this sort of registration as non-affine but by convention they are referred to as nonlinear. Sometimes rigid body registration is considered as a third class. It is a special case of affine registration which only allows translation and rotation. Figure 2.9 compares these modes of registration. Figure 2.14 in Section 2.3.4 illustrates the difference between affine and nonlinear registration in terms of brain MRI images.

The first application of registration in medical imaging was the alignment of 3D images taken of a patient using different modalities such as CT, MRI and nuclear medicine techniques (Hill *et al.*, 2001). Since then intra-modal, intra-subject registration has become common for both research and clinical use such as the registration of a series of

[1] Affine registration has 12 parameters only for 3D images

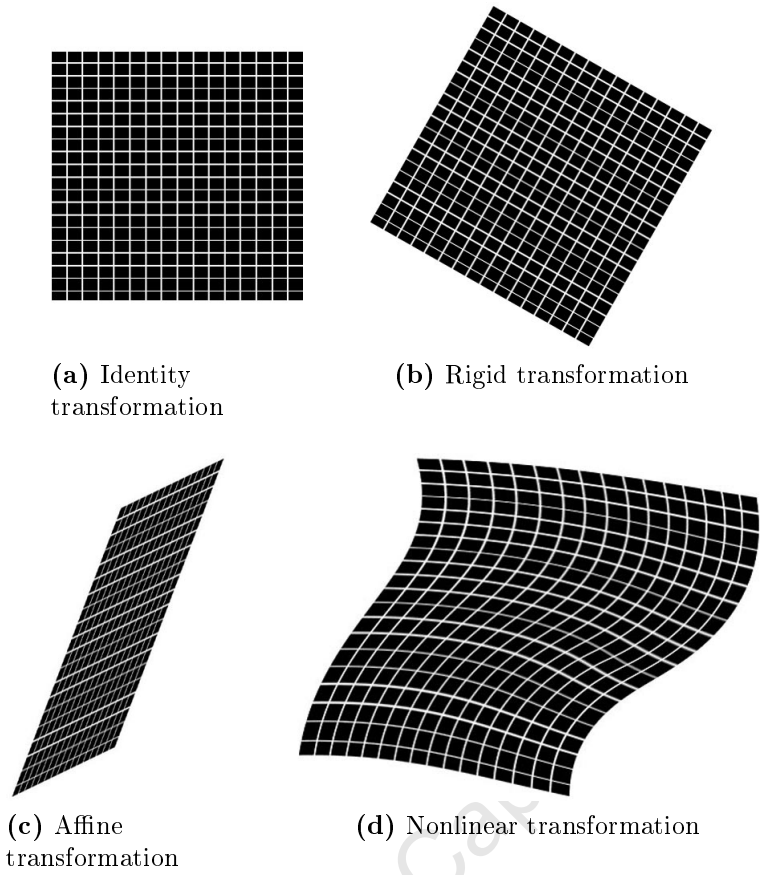

(a) Identity transformation

(b) Rigid transformation

(c) Affine transformation

(d) Nonlinear transformation

Figure 2.9: Examples of different types of transformations applied to a grid.

images taken over time. This could be over a short time such as in functional MRI or over a long time such as in monitoring tumour growth. In both cases the changes between the images can be very subtle and registration facilitates the inspection of such changes. Affine registration is usually sufficient for these applications as the changes in the images result from patient motion and sensor misalignments. Nonlinear registration methods have been useful in propagating segmentation through a series of images such as the intra-subject case of studying developmental growth of a structure or the inter-subject case of automatically identifying a structure. Inter-subject normalization is standard in neuroscience research as it highlights population variability; the registration of subjects to a standard space, such as the registration of brain images to the Talairach stereotaxic space (Talairach and Tournoux, 1988), has become a regular application (Thirion *et al.*, 2006; Collins *et al.*, 1994).

From the point of view of registration, a medical image is considered to be a spatial mapping of a physical property of the tissue of a patient or subject (Hill *et al.*, 2001). Thus there is an unspoken assumption that the images that registration deals with are photometric and thus discrete. As mentioned, the transformation from a registration algorithm is a mapping from the coordinate system of the source image to that of the reference image. In order to apply this mapping to discrete images it is necessary to interpolate (Zitova, 2003). The most common interpolation method used in medical image registration is trilinear interpolation but nearest neighbour interpolation and sinc interpolation methods are also used (Hill *et al.*, 2001). Figure 2.10 compares nearest neighbour

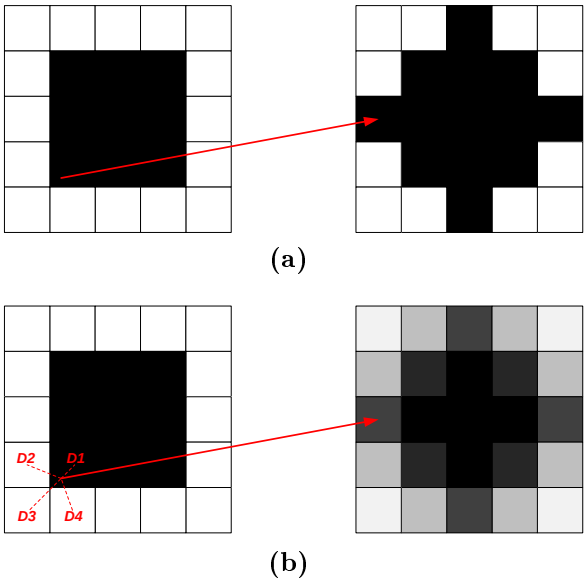

Figure 2.10: Schematic demonstrating the workings of (a) nearest neighbour and (b) bilinear interpolation. A source image consisting of a 9 pixel black square is rotated by 45°. Nearest neighbour interpolation produces jagged edges whereas bilinear interpolation blurs the image as it acts as a low pass filter (Hill *et al.*, 2001). Bilinear interpolation uses the inverse of the distances D1 - D4 as weights to combine the 4 neighbouring pixels of the continuous point, i.e. the vector tail, on the source image to find an intensity for the pixel on the output image at the vector head. Bilinear interpolation is easily generalized to three dimensions, i.e. to trilinear interpolation, the only difference being that each point has 8 neighbouring voxels as opposed to the 4 neighbouring pixels shown here.

and trilinear[2] interpolation as they would be applied to an image in a transformation. A vector showing the transformation of a voxel has its head at a discrete voxel coordinate on the output image, and its tail at a continuous point, i.e. between voxels, on the source image thus necessitating interpolation. This vector is present in nonlinear registration and implied in affine registration by multiplying the output voxel coordinates with the affine transform and drawing a vector between the new and old coordinates.

As ubiquitous a tool as registration has become in medical imaging, it is not without its shortfalls and limitations (Rohde, 2005). The dependence on interpolation methods, particularly with trilinear interpolation, leads to a bias of registration algorithms toward blurred images. Many nonlinear registration algorithms are too slow for clinical use (Crum, 2004). Registration algorithms are often not general solutions to medical imaging problems. Medical imaging technology is improving rapidly and thus the nature of images needed to be registered is also changing. A registration implementation that is optimized for one imaging modality might no longer be optimal when that modality is advanced. This can be problematic if the registration algorithms are not changing with the imaging techniques and devices (Crum, 2004). Another problem is that there is no standard method of evaluating or comparing registration implementations. The problem of validation is presented in detail in Section 2.3.4. Many of these shortcomings stem from the fact that the definition of biological homology, a concept central to the goals of registration, is highly debated. Maudgil *et al.* (1998) defines homologous features as those that "are structurally and functionally equivalent between different organisms" but points

[2]The figure actually shows bilinear interpolation as the 2D image is simpler to follow on paper. The concept of trilinear interpolation is identical but with a third dimension.

out that it is difficult to define these equivalences in the cerebral cortex. Homology is an underlying assumption of registration as registration aims at a spatial correspondence of homologous features. As homology is not strictly defined, registration is based on only a partially understood assumption and thus is itself not fully understood.

2.3.1 Affine Registration

Affine registration is a registration that uses an affine transformation to re-map an image. An affine transformation is of the form $\vec{X}' \mapsto \mathbf{L}\vec{X} + \vec{T}$, which becomes

$$\begin{pmatrix} x' \\ y' \\ z' \end{pmatrix} = \begin{pmatrix} l_{11} & l_{12} & l_{13} \\ l_{21} & l_{22} & l_{23} \\ l_{31} & l_{32} & l_{33} \end{pmatrix} \begin{pmatrix} x \\ y \\ z \end{pmatrix} + \begin{pmatrix} t_x \\ t_y \\ t_z \end{pmatrix} \tag{2.6}$$

in the 3D case. $\vec{T}$ is a vector of the *translation* parameters. $\mathbf{L}$ is a linear transformation and its parameters control *rotation*, *scaling* and *shears*. The computational complexity of the affine transform can be reduced to a single matrix multiplication by augmenting $\mathbf{L}$ as follows

$$\begin{pmatrix} x' \\ y' \\ z' \\ 1 \end{pmatrix} = \begin{pmatrix} l_{11} & l_{12} & l_{13} & t_x \\ l_{21} & l_{22} & l_{23} & t_y \\ l_{31} & l_{32} & l_{33} & t_z \\ 0 & 0 & 0 & 1 \end{pmatrix} \begin{pmatrix} x \\ y \\ z \\ 1 \end{pmatrix} \tag{2.7}$$

which is known as the homogeneous affine transform. Equations 2.6 and 2.7 are easily proved equal by multiplying out the matrices. This report considers affine transformations in the homogenous form and treats affine transformation as $\vec{X}' \mapsto \mathbf{A}\vec{X}$, where $\mathbf{A}$ is the 4×4 augmented matrix as shown in Equation 2.7.

The 9 parameters in $\mathbf{L}$ and the 3 parameters in $\vec{T}$ gives us a 12 degrees of freedom (DOF) transformation, $\mathbf{A}$. These 12 DOF are x, y and z components of scaling, rotation, shearing and translation. Only the translation parameters are clear from inspection, the others can be found using matrix decomposition methods such as QR decomposition or polar decomposition but the results of these are still non-trivial to interpret (Shoemake and Duff, 1992). Fortunately decomposition is an unnecessary step in both registration and the application of the transformation, however, knowing the rotations and shears an image has undergone can be a useful tool in analysing a registration.

A special case of affine transformation is the rigid body transformation. It only rotates and translates and thus has 6 DOF. This has the property that the distance between any two arbitrary points remains unaltered by the transformation (Hill *et al.*, 2001). If the object being imaged can be modelled as rigid, which is often the case in medical imaging, this 6 DOF transform should be sufficient for registration. However having freedom over scaling and shearing allows for corrections due to sensor location, i.e. field of view, or sensor distortions (Hill *et al.*, 2001; Hajnal *et al.*, 2001, Ch.5) and thus affine registration is more robust and likely to provide a more general solution to the registration problem. Affine transformations do not preserve distances but do preserve parallel lines (Hill *et al.*, 2001).

Applying an affine transform to a source image to create an output image is an iterative process. The intensity of each voxel on the output image is found on the source image at a location defined by the affine transform. The coordinates of each voxel of the output image, $\vec{X}'$, are multiplied by the inverse of the affine transform, $\mathbf{A}^{-1}$, to produce the coordinates on the source image, $\vec{X}$, where the new intensity is found. $\vec{X}'$ is discrete but

$\vec{X}$ is not. Thus the source image needs to be interpolated. This interpolation is done case by case rather than on the entire image. Figure 2.10 above shows how the interpolation is done for nearest neighbour and trilinear interpolation.

2.3.2 Nonlinear Registration

6 DOF rigid registration and 12 DOF affine registration cover the majority of medical image registration applications. These methods are sufficient unless the internal structures of the object being imaged are expected to vary in size and shape. Images of brains from subject to subject show a high variability of the shapes of internal structures (Bjaalie, 2002), as do developmental images taken of one subject. In these cases, 12 DOF registration is not enough for high resolution correspondence of the images. Nonlinear registration is useful in inter-subject registrations as it can account for population variability and in intra-subject registration as it can account for the deformation of tissue over time.

Figure 2.8 above is an example of nonlinear registration. The corpus callosum of the source image has two concavities on the superior side of its body. In contrast, the superior side of the same structure in the reference image is completely convex. Both images are sagittal slices of brain images taken through the centre. This is an example of the variability in the shape of structures mentioned in the previous paragraph. The output image is aligned with the reference image, not just in the external shape of the brain, but there is also alignment of the different structures within, such as the corpus callosum which shows none of the concavity of the source image and is nearly perfectly aligned with the reference image. Correspondence of this resolution cannot be achieved using affine registration.

Nonlinear registration is the subject of active and ongoing research (Arsigny *et al.*, 2009). This has led to a wide variety of algorithms and implementations. The choice of transformation is the key difference in these implementations. The affine transform can be extended to be nonlinear by describing the transform as a linear combination of higher order polynomials or basis functions (Ashburner and Friston, 1999) which can be written as (Hajnal *et al.*, 2001, Ch.13)

$$\begin{pmatrix} x' \\ y' \\ z' \\ 1 \end{pmatrix} = \begin{pmatrix} a_{00} & \cdots & a_{0n} \\ a_{10} & \cdots & a_{1n} \\ a_{20} & \cdots & a_{2n} \\ 0 & \cdots & 1 \end{pmatrix} \begin{pmatrix} \theta_1(x,y,z) \\ \vdots \\ \theta_n(x,y,z) \\ 1 \end{pmatrix} \tag{2.8}$$

where $\theta_1(x,y,z), ..., \theta n(x,y,z)$ are the polynomials or basis functions. Other algorithms base registration on physical processes such as splines (Rohr, 2003), elasticity (Kyriacou *et al.*, 1999; Kybic and Unser, 2003), fluid flow (Chiang *et al.*, 2008) and the demons algorithm which is based on diffusion (Thirion, 1998). These implementations exhibit a range of DOF, the highest of which have a different displacement vector for every voxel (Arsigny *et al.*, 2005). A common way to represent this type of nonlinear transform, as opposed to algorithms based around Equation 2.8 or splines, is as a vector field (Hill *et al.*, 2001). This is a matrix with dimensions equivalent to the voxel dimensions as the images. Each element of the transformation corresponds to a voxel on the output image. The elements of the field each contain a displacement vector. This displacement shows where on the source image the intensity for the corresponding voxel on the output image can be found. The transformation is a vector field of displacement pointing from the source image to the output image. The tails of the displacements can fall anywhere in

continuous space whereas the heads are restricted to the discrete voxel locations of the output image. Thus interpolation of the source image is still needed. Figure 2.11 shows an example of visualizing this type of nonlinear transformation matrix, also referred to as the warp field or displacement field. The displacement vectors in the field should have their heads located at the centre of each pixel and their lengths are likely to span multiple pixels. Figure 2.12 shows a 3×3 section from a displacement field for a 2D image.

The optimization process is an important step in nonlinear registration. Many algorithms find the global optimum using local optimization methods by iteratively applying them to higher resolution versions of the problem. The images themselves are the highest resolution available. The lower resolution images are created by downsampling these. Some studies show that global optimization methods outperform these local optimization multi-resolution approaches (Jenkinson and Smith, 2001). Affine registration is normally used to provide a starting estimate (Brett *et al.*, 2002). By starting the algorithm closer to the solution, convergence time is decreased as is the chance of converging to a local optimum.

A very common procedure when dealing with inter-subject images is to register all the images to a standard space. This is known as spatial normalization. The Talairach stereotaxic space (Talairach and Tournoux, 1988) is considered to be the standard space for brain images. It presents a coordinate system so that the location and structure of regions of interest can be compared. This steroetaxic space was based on a single brain. The Talairach stereotaxic space is still the most common standard space used in neuroscience research despite its age and the numerous more representative options that have come since. For example the MNI stereotaxic space was based on MRI images of more than 250 young, normal brains and is thus more representative of the variability of the human brain (Evans *et al.*, 1992). An international consortium for brain mapping has since created a probabilistic atlas which models the variance of the human brain. It uses various forms of data collection and is based on over 7000 brains (Mazziotta *et al.*, 2001). More recently, white matter atlases have been created using the new information afforded by DTI and tractography (Mori *et al.*, 2008).

2.3.3 DTI Registration

Due to the higher dimensional nature of DTI images (Yang *et al.*, 2008), there are two additional difficulties when attempting their registration (Gee and Alexander, 2006). The first, and simpler of the two, is that the similarity measurements used on regular images do not apply to DTI images. Principal diffusion direction or the cross correlation of FA can be used for this (Alexander *et al.*, 2002*a*). A widely used option is the extension of the voxel square Euclidean difference for diffusion tensors

$$ED = \sqrt{Tr[(\mathbf{D}_1 - \mathbf{D}_2)^2]} \tag{2.9}$$

where $\mathbf{D}_1$ and $\mathbf{D}_2$ are the diffusion tensors. Pollari *et al.* (2007) compare this distance with 4 others showing that the Euclidean distance lowers the number of local minima but more consistent results were obtained using metrics based on either diffusion profiles or on the diffusion modes described by the Westin metrics.

The second, and major, complication is that of re-orientation. This is because each voxel contains a diffusion tensor (DT) which has a 3D shape and three directions associated with it. When registering a scalar image, the value at each voxel is simply reproduced in a new location defined by a transformation and only slightly altered by interpolation.

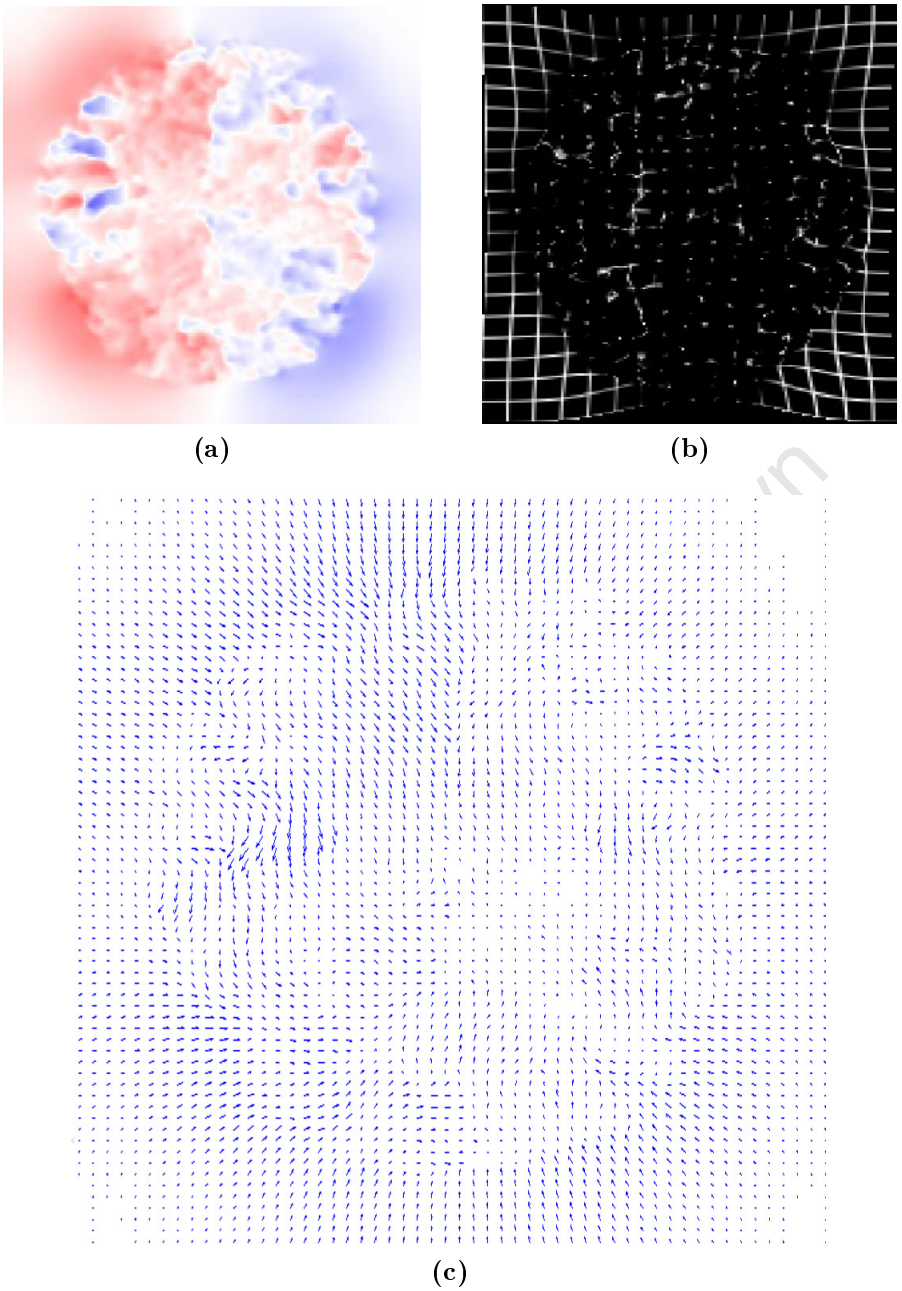

Figure 2.11: Visualization of a displacement field from a nonlinear registration of two FA images of the brain. (a) shows the magnitude of the x-component of the displacement vectors of a cross section of the displacement field, the red and blue are positive and negative displacements. This image only shows one of three components of displacement. (b) shows the effect of applying this transformation to a 3D grid. This is a convenient way to view the effect of these higher dimensional images. (c) A cross section of a displacement field which represents each vector as an arrow. This type of image is best viewed in an environment that allows the image to be rotated in 3D. The image displayed here is downsampled by 3 in the x and y directions so that the image is not too cluttered to be viewed.

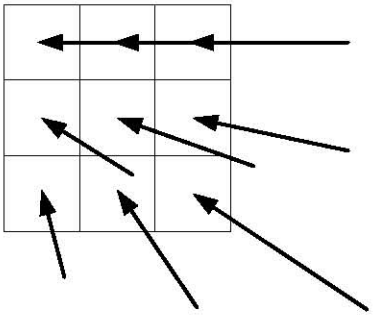

Figure 2.12: A 3×3 section of a displacement field. Note that the heads of each vector are aligned with the centre of each pixel, which correspond to the pixels of the output image. The tails fall in continuous space in between the pixels of the source image.

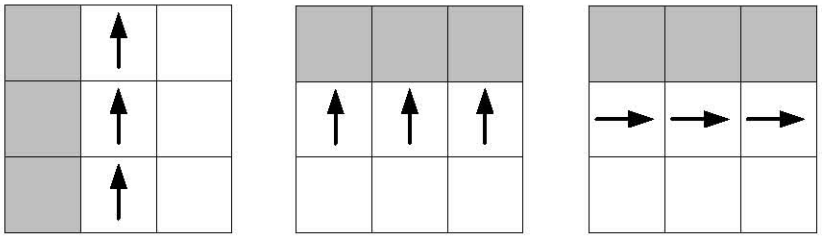

Figure 2.13: This figure shows a simplified analogue of a DTI image (a) before rotation, (b) after a 90° rotation *without* voxel re-orientation and (c) after the same rotation but with re-orientation. The grey line on the left in (a) represents an anatomical structure and also illustrates the rotation. The arrows indicate the directional nature of DTI voxels. Before registration the arrows are pointing head to tail forming a line parallel to the grey structure. After registration without reorientation the arrows form 3 parallel lines perpendicular to the structure. If the voxels are re-oriented, the line created by the arrows is preserved as is its parallel relationship to the grey structure. This illustrates the need for voxel re-orientation when transforming DTI images.

This approach does not produce satisfactory results when dealing with DTI images as the orientation of the DT of each voxel needs to be altered in order to preserve its relative orientation to the anatomical structures as well as to the DTs of each other voxel (Alexander *et al.*, 1999; Xu *et al.*, 2003). This problem, as well as how it can be solved by correctly re-orienting each DT, is demonstrated in Figure 2.13.

As the DT reflects the local tissue microstructure, it is safe to assume that the fundamental shape of each DT does not change under transformation (Xu *et al.*, 2003). Only the orientation is altered. This implies that the eigenvalues do not change, only the eigenvectors. Although this assumption does not hold in cases such as oblate spheroids being sheared (Gee and Alexander, 2006), it is taken by most methods of DTI registration.

DTI registration is still at an early stage (Gee and Alexander, 2006). Three basic methods of re-orientation of DTs are found in the current literature (Alexander *et al.*, 2002*b*; Yeo *et al.*, 2008; Gee and Alexander, 2006; Xu *et al.*, 2003). The first applies only to rigid body registration. The second two apply to affine registration and can be generalized to nonlinear registration. They are the *finite strain* (FS) method and the *preservation of principal directions* (PPD) method.

For a purely rigid transformation, the rotational component can be directly applied to each DT (Alexander *et al.*, 1999). In other words the new DTs are given by the similarity transformation (Alexander *et al.*, 2002*b*)

$$\mathbf{D}' = \mathbf{R}\mathbf{D}\mathbf{R}^T \tag{2.10}$$

where $\mathbf{R}$ is the rotation matrix, $\mathbf{D}$ is the original DT and $\mathbf{D}'$ is the re-oriented DT. Consider Figure 2.13c as an example. Here the same rigid transformation, a 90° rotation, was applied to each DT and produced the desired result. Note that translational components of the transformation need not be considered when transforming the DTs.

This does not hold for affine transformations. Simply replacing $\mathbf{R}$ in Equation 2.10 with the linear component of the affine transformation

$$\mathbf{D}' = \mathbf{L}\mathbf{D}\mathbf{L}^T \tag{2.11}$$

results in a $\mathbf{D}'$ of a different size and shape from $\mathbf{D}$. This violates the assumption that spatial transformation of a DTI image should only effect the DT orientations. The FS method uses a matrix decomposition[3] to extract the rotational component, $\mathbf{R}$, from $\mathbf{L}$ (Alexander *et al.*, 2002*b*). This rotational component is global for the image and can be applied to the DTs using Equation 2.10.

The FS method completely discards the shearing and stretching components of the transformation. The PPD method accounts for these by applying $\mathbf{L}$ to the principal diffusion direction, i.e. the principal eigenvector $\vec{e_1}$, and then uses the following equation to re-normalize it to become $\vec{n_1}$

$$\vec{n_1} = \frac{\mathbf{L}\vec{e_1}}{|\mathbf{L}\vec{e_1}|} \tag{2.12}$$

The DT is oriented such that $\vec{e_1}$ maps to $\vec{n_1}$. This is satisfactory for prolate DTs. For oblate DTs $\vec{e_2}$ must be rotated so the $\vec{n_1}$ - $\vec{n_2}$ plane is the same as the $\mathbf{L}\vec{e_1}$ - $\mathbf{L}\vec{e_2}$ plane (Alexander *et al.*, 2002*b*). Where the FS method found a global re-orientation, the PPD method finds individual local re-orientations for each voxel.

These methods generalize to suit nonlinear transformations in a straightforward way. Alexander *et al.* (2002*b*) show that the displacement of each voxel can be modelled as a local affine transformation by adding the identity matrix to the jacobian of the nonlinear transformation at the point.

Some approaches consider neighbourhoods of voxels to calculate the re-orientation (Xu *et al.*, 2003; Yang *et al.*, 2008; Xue *et al.*, 2010). This makes the registration more robust to noise as it considers the underlying fibre structure. Although this underlying fibre structure is not known, a probability distribution can be estimated using a neighbourhood of tensors (Xu *et al.*, 2003). Yang *et al.* (2008) use the Westin measures to develop rotationally invariant attributes for matching using three different sized neighbourhoods to account for local and global geometric features. They use local statistical information to preserve white matter tracts and although they show impressive results, the matching of fibre bundles is still imperfect. Recent work has shown that transformation based on anatomical images such as T_1-weighted images rather than registering the lower resolution and noise prone FA images can improve results (Zöllei *et al.*, 2010). Most methods first align the geometric features and then re-orient the tensors but new algorithms that incorporate the re-orientation directly into the cost functions are beginning to emerge (Yeo *et al.*, 2008).

[3] Shoemake and Duff (1992) provide an insightful explanation into affine transformation matrix decomposition.

The registration of DTI images is a new and active area of research. The initial results are promising and because the higher dimensionality constrains the registration, DTI registration is in fact less prone to local minima than anatomical registration (Gee and Alexander, 2006). There are not yet definitive methods for similarity metrics, interpolation or the re-orientation of tensors but promising algorithms are being published every year.

2.3.4 Methods of Validation

A major problem with image registration is the lack of a gold standard against which to assess to what degree the registration has succeeded (Rohde, 2005; Hill *et al.*, 2001; Maintz and Viergever, 1998). Validation tackles the problem of quantifying registration accuracy. This definition of validation leads directly from the definition of registration, i.e. to measure the correspondence between two images. Maintz and Viergever (1998) point out the paradox that if there was a perfect measure of this error it would be used in the registration algorithms themselves and therefore not provide any additional information if used as a tool of assessment. Regardless, such a measure does not exist for various reasons. Firstly it is difficult to know the difference between registration error and physical differences in the subjects being imaged (Zitova, 2003). Secondly there is not always a one-to-one correspondence between images, especially in inter-subject registration. This means that perfect alignment is not possible.

Visual inspection is a widely used method of validation (Crum *et al.*, 2003; Hill *et al.*, 2001). Although it does not provide a quantitative measure, it is reliable and used in clinical practice. Software tools can assist with visual validation such as a checkerboard overlay (Nett, 2001) in which each image is broken up into a number of smaller blocks. A new image is made using blocks alternating between the two images being validated. Sometimes the two alternating images are displayed in different colours to provide a more obvious visual contrast. A difference image is another useful tool (Holden *et al.*, 2000). One image is subtracted from another and this difference is plotted. A perfect registration would yield an image that is purely middle grey. Deviations toward black or white highlight areas of misalignment. Representing a difference of zero as middle grey rather than plotting the absolute error allows the direction of misalignment to be inferred directly from the difference image. Figure 2.14 shows these methods of visual validation. Each validation image is presented before registration, after affine registration and after nonlinear registration. The improvement in alignment after registration is visibly clear.

Quantitative approaches to validation include the absolute mean of the distance between images, the correlation of the images, a target registration or fiducial registration error or the distance between lines, surface or edges in the images (Hajnal *et al.*, 2001, Ch.6). Klein *et al.* (2009) used volume and surface overlaps of the whole brains as well as the structures within them.

Any of the above quantitative and visual verifications validate the registration on a case by case basis. Another important validation is of the algorithm itself. There are several approaches to this. Many registrations are needed to reveal the accuracy of a system due to variability. Statistics based on the quantitative measures of alignment gathered for many registrations are used to model these systems. A wide range of statistics are used in the literature from simple means and standard deviations to ANOVA tests (Klein *et al.*, 2009) and percentage thresholds (Hajnal *et al.*, 2001, Ch.6).

Another method to test a registration algorithm is to create a closed circuit of registrations. This requires at least three images. Image A is registered to B, B registered to

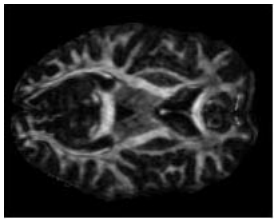

(a) Source image

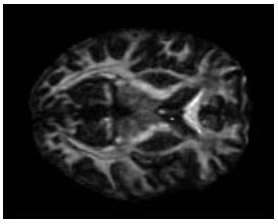

(b) Reference image

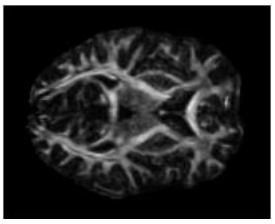

(c) Output image for affine registration

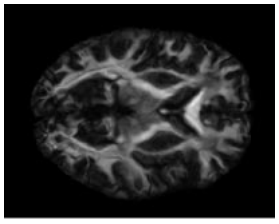

(d) Output image for nonlinear registration

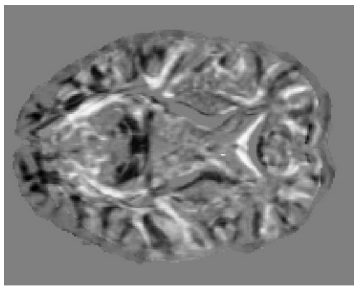

(e) Difference image of the reference and source images

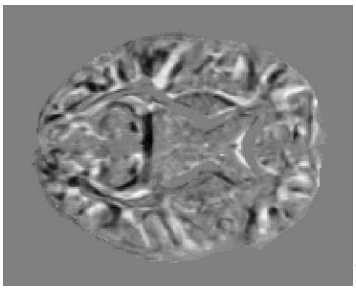

(f) Difference image of the reference and affine output images

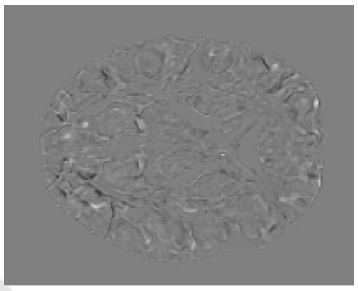

(g) Difference image of the reference and nonlinear output images

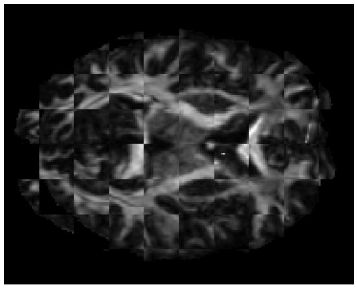

(h) Checkerboard of the reference and source images

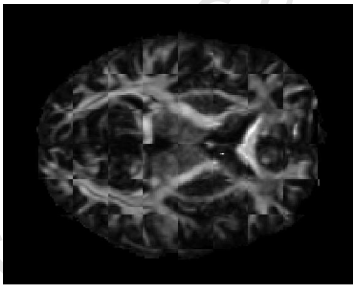

(i) Checkerboard of the reference and affine output images

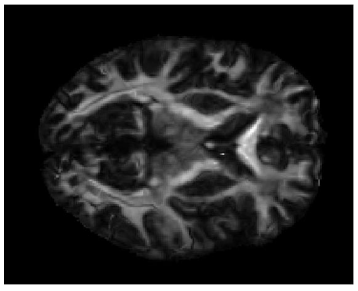

(j) Checkerboard of the reference and nonlinear output images

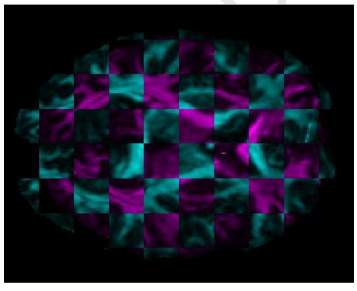

(k) Coloured checkerboard of the reference and source images

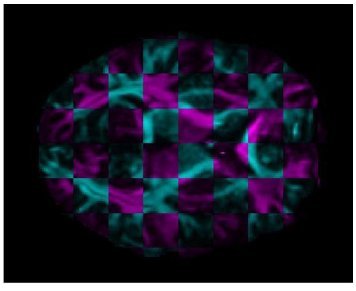

(l) Coloured checkerboard of the reference and affine output images

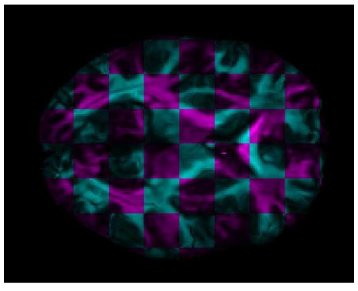

(m) Coloured checkerboard of the reference and nonlinear output images

Figure 2.14: Visual validation of registration demonstrating difference images, checkerboard images and coloured checkerboards for affine and nonlinear registration.

C and C registered to A. The product of these three transformations should result in the identity transformation (Hill *et al.*, 2001; Hajnal *et al.*, 2001, Ch.6). The deviation from this is a measure of failure.

Although there is no true gold standard, useful approximations to the concept of a gold standard can be made (Hajnal *et al.*, 2001, Ch.6). The alignment of fiducial markers, either physical or implied by the software, can be measured accurately and precisely. The difficulty is in measuring the correspondence of the markers between cases. Another problem with this approach is that physical fiducial markers for brain images such as those used by Black *et al.* (1996) are highly invasive. Phantoms provide another form of gold standard but suffer from the uncertainty and noise of the imaging process. Simulations of artificial data provide the closest approximation to a gold standard (Hill *et al.*, 2001; Hajnal *et al.*, 2001, Ch.6). These are typically created by applying a precisely known geometric transform to the source image and using this transformed image as a reference. The error in such a case can be exactly quantified. However, the use of such simulations is limited as they require accurate models and measures of variability to be fully representative (Maintz and Viergever, 1998).

The validation metric depends on the intended application, especially in the clinical world. Validation of registration is a complex task. Population variability, the lack of a true gold standard and the uncertainty of whether the error is physical or due to registration are all contributing factors. Even though the methods are not perfect, validation is still an important step to assess success or failure of registration, to test if an algorithm or implementation is of a clinical standard and to compare registration algorithms and implementations.

Chapter 3

Context

3.1 The Current State of DTI Registration and Tractography

With the ability to image the fibrous structure of white matter in vivo, tractography has applications ranging from population morphology research (Sullivan *et al.*, 2010) to radiosurgery (Koga *et al.*, 2011). The images produced are inconsequential if we lack the capability to precisely localize them with the anatomy (Bjaalie, 2002). Whether this is to compare them against other imaging modalities, to monitor growth or developmental changes in longitudinal studies or analyse the variability across subjects, registration has become a ubiquitous preprocessing step.

The vast majority of work performs registration on the DTI images *prior* to tractography. Rohde (2005) points out that although image registration is in wide spread use, it is far from an infallible process. Research into inter-subject registration is on the rise, but there are unresolved questions of homology (Maudgil *et al.*, 1998) and correspondence. Rohde (2005) further shows that the majority of image registration methods produce results biased towards blurred images rather than the optimal results. Registration of DTI images is a new and actively researched field. At this early stage in the development of the technology, many questions remain unanswered.

Despite the uncertainties of DTI registration, tractography is often applied without regard to the accuracy of this preprocessing step. In an investigation into the reproducibility of tractography, Heiervang *et al.* (2006) converted fibre bundles to volumes and showed an inter-session overlap of only 81% showing how sensitive tractography is to the noise and the inherent uncertainty of DTI. Danielian *et al.* (2010) show an average intraclass correlation of 0.85 for fibre bundle volumes in scan re-scan reliability tests, but with high coefficients of variation. They were unable to demonstrate the reliability of λ_1 measures across scans.

Tractography is not a robust process. The inherent uncertainty in the fibre tracking process is an important consideration and can easily be overlooked since fibre tracking is known as *deterministic* tractography. Although the tracking process itself may be deterministic, the data on which it is performed is based on diffusion which is a stochastic process. Even in the best of conditions, DTI may not represent reality as precisely as it is sometimes assumed to (Klein *et al.*, 2010*b*; Yamada, 2009). Deterministic tractography is based on integration and thus accumulates error. This means that even small errors introduced by registration in the diffusion tensors can have a large impact on tractography. Researchers are beginning to consider this impact, but the full extent of the effect

of registration of DTI images on the outcome of fibre tracking has not been thoroughly studied. Xu *et al.* (2003) warn that tracking fibres based on an average of spatially normalized tensor fields only reconstructs common aspects of fibre anatomy and cannot show individual deviations. Results of a comparative study by Yang *et al.* (2008) indirectly shows how vastly the outcomes of tractography can differ based on different DTI registrations, and that the results can be improved by considering the effect registration will have on tractography. For this reason it is important to research the implications of registering DTI images before tractography as well as the feasibility of registering images after tractography. This work examines the latter.

3.2 Methods of Direct Registration of Fibre Tracts

Registering tractographic fibres is a complex problem. Fibre data images are fundamentally different from scalar images or even DTI images, in that they are not voxel-based. Each fibre is represented as an ordered set of 3D position vectors. The images that result from tractography are a collection of these fibres. The position vectors themselves are in continuous space. This is the first fundamental difference as the data of scalar or DTI images are only described at discrete locations, whereas the data of fibre images are described in continuous space. The other major difference is that regular images are a *single* ordered set of points with three dimensions of ordering. The fibre image is an unordered collection of *many* ordered sets of points, with the ordering only being in one dimension, i.e. in the direction of the fibre. Figure 3.1 shows an example of a single fibre and portions of a fibre compared to voxel space.

These differences have implications for registration. Firstly, conventional distance metrics are meaningless. These must be replaced with metrics such as the mean closest distance (O'Donnell and Westin, 2007). Secondly, transformation requires 3D interpolation. The fibre data can only be meaningfully interpolated along the course of the fibre. The fibres can be thought of as infinitely thin which means the probability that the point of interpolation falls on the fibre is zero. Thus new forms of registration are required to tackle these differences.

To the best of the author's knowledge, there are currently only four publications (three of which are in conference proceedings) that directly address fibre tract image registration (Leemans *et al.*, 2006; Ziyan *et al.*, 2007; Mayer and Greenspan, 2008; Shadmi *et al.*, 2010). This is a meager number when compared with the number of publications on DTI registration in the past 5 years (Wang *et al.*, 2011; Ingalhalikar *et al.*, 2010; Zöllei *et al.*, 2010; Xue *et al.*, 2010; Jia *et al.*, 2011; Geng *et al.*, 2009; Yap *et al.*, 2009; Yang *et al.*, 2008; Yeo *et al.*, 2008; Chiang *et al.*, 2008; Pollari *et al.*, 2007; Gee and Alexander, 2006, etc), and thus it is a topic in need of further investigation and research.

Leemans *et al.* (2006) represent each fibre as a space curve using curvature and torsion. They pair each fibre on the source brain to the most similar fibre on the reference brain. This correspondence is one-to-one making the method suitable only for intra-subject registration. A further restriction is that the registration is based on a global rigid transformation (6 DOF). This is found by aggregating the local rigid transformations of each fibre pair. Mayer and Greenspan (2008) developed a method to register a single fibre bundle source to a whole brain tractography reference using affine transformations. This method is based on a modified version of the iterative closest point (ICP) algorithm finding a global affine transformation for the bundle. They show good results for both intra-subject and inter-subject registrations.

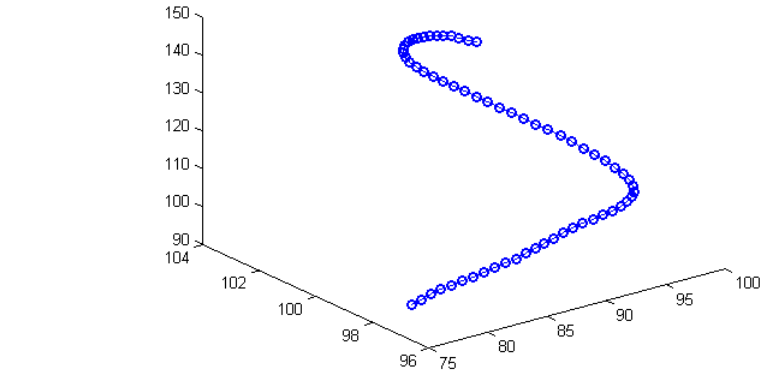

(a)

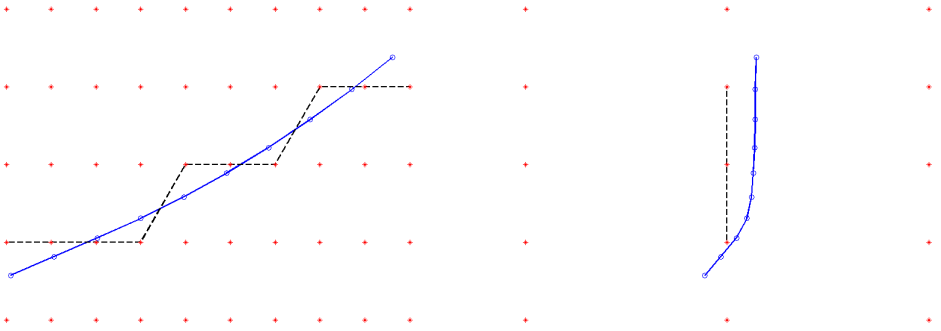

(b) (c)

Figure 3.1: An example of fibre data. (a) shows a single fibre in 3D space. (b) shows the first 10 points of a fibre projected onto the x-z-plane. The points are shown as blue open rings, the blue line shows that when the fibre data are connected in order they form a fibre, the red stars show the x-z-plane integer values, i.e. the coordinates of voxel space, and the black dashed line shows the effect of discretizing the fibre to fit voxel space. (c) shows the same image as (b) but projected onto the y-z-plane. This figure shows that the continuous nature of fibre data contains essential information that would be lost if the data were treated as discrete.

Two works have applied nonlinear transformations directly to the fibre images. Shadmi *et al.* (2010) project the fibres onto a D-dimensional feature space. This is done in such a way as to allow the registration to be considered a probability density estimation. Local affine transformations are defined during the estimation process and create a global nonlinear transformation in the form of a piecewise smooth affine transformation. They use the global affine method described by Mayer and Greenspan (2008) to provide a starting estimate and test the algorithm only using whole brain tractographies. They quote a 17% improvement on the results of the global affine method. Results only represent a global fit and give little indication of alignment of the internal structures, which is a key reason to choose a nonlinear registration. The local fit of the bottom of the brain stem is visibly improved using the nonlinear method but this is the only indication of an improvement of internal structures. As the brain stem is an exposed structure, contributing to the outer shape of the whole brain tractography, it is not an ideal choice to indicate the alignment of internal structures.

Ziyan *et al.* (2007) segment both the source and target image into corresponding fibre bundles. An affine transformation is found for each fibre bundle by first converting the

fibre bundles to probability distributions. These probability distributions are discretized to form images suitable for conventional registration. A local affine transformation is found for each bundle in this way. The local transformations are then combined to form a global nonlinear transformation using the polyaffine transformation developed by Arsigny *et al.* (2005), specifically the log-Euclidean approach (Arsigny *et al.*, 2009). This nonlinear approach allows the various internal structures of the brain to be well aligned but the local affine properties protect the integrity of the fibres. To validate the registration, the registered tracts are compared with the reference DTI images. The success of registration is equated with the plausibility that the tracts could be outcomes of the reference DTI image. The polyaffine result is compared to a global affine registration and a demons algorithm based registration, both based on the FA-images. The polyaffine approach produces better results than both the global affine and the demons approach.

Neither nonlinear algorithm is assessed by comparison of the alignment of the output fibres and the reference fibres, with that of the source fibres and the reference fibres. Both show improvements against alternative methods, but neither show the improvement when compared with no registration.

3.3 Experiments

As indicated in Chapter 1, this study addresses the following research goal: to investigate the available techniques for directly registering fibre images and to experiment with novel adaptations of these.

Ziyan *et al.* (2007) and Xue *et al.* (2010) apply nonlinear deformations directly to fibre images. Ziyan *et al.* (2007) compare their fibre registration method to the application of a nonlinear demons transformation as well as to the application of an affine transformation to fibre data. However, neither Ziyan *et al.* (2007) nor Xue *et al.* (2010) explain how the transformations, developed for scalar images, are applied to the fibre data. These transformations were developed to be applied to scalar, voxel based-images. They can be applied to DTI images by addressing the concerns of tensor re-orientation as described in Section 2.3.3, however, the application of such transformations to tractographic images is a problem that has not been addressed in literature thus far. Applying a transformation to a non-voxel-based DTI image is nontrivial. Jia *et al.* (2011) approach this problem by applying the transformations directly to the regions of interest (ROIs) used to extract the fibre tracts, and tracks new fibres based on the transformed ROIs.

The first two experiments in this project register FA images using a demons algorithm and an affine registration and then reapply the transformations to the fibre data. The interpolation problem is solved by interpolating the displacement field rather than the source image. This is done through a novel technique using Delaunay triangulation to find a suitable neighbourhood of vectors to interpolate a displacement for each fibre point. This method is presented in Section 4.4.

Ziyan *et al.* (2007) and Mayer and Greenspan (2008) use segmented fibre bundles as their experimental data rather than whole brain tractographic images, as these create a tangible way to assess the success of registration in terms of the alignment of the internal structures, unlike the method of Shadmi *et al.* (2010) which works with unlabelled, global data making the results difficult to interpret. If an image is completely labelled, the problem of correspondence is solved (Crum *et al.*, 2003). It is impossible to achieve such a complete labelling, but a partial labelling does help to assess correspondence and gives an indication of the success of a registration algorithm. Extracting ROIs is one approach to

such partial labelling and in terms of tractographic images this means extracting meaningful fibre bundles of white matter structures. For this reason, the experiments in this work make use of segmented fibre data, the details of which are presented in Section 4.1.1.

Ziyan *et al.* (2007) convert the fibre bundles to probability distributions according to the equation

$$\mathbf{P}_{b_i}(\vec{x}) = \frac{1}{Z} \sum_{t_j \in b_i} \sum_{\vec{x}_k \in t_j} \kappa(\vec{x} - \vec{x}_k) \tag{3.1}$$

where b_i is a fibre bundle, t_j is a single fibre and $\vec{x}_k$ is a point on a fibre defined as a 3D spatial vector. $\vec{x}$ is the 3D spatial coordinate of the probability distribution, i.e. the voxel coordinate, Z is a normalizing constant chosen to make the values of $\mathbf{P}_{b_i}(\vec{x})$ sum to 1 and $\kappa(\vec{x} - \vec{x}_k)$ is a Gaussian kernel centred around $\vec{x}_k$. The fibre bundles that are used in this project have on average 1300 fibres per bundle with an average of 100 points per fibre. Multiplied by the $160 \times 200 \times 160$ voxels of each DTI image, Equation 3.1 needs to calculate 0.7 trillion values to create a probability density function (PDF) for one, average fibre bundle. This is very computationally expensive. Ziyan *et al.* (2007) do not specify the time taken to perform this calculation but the results in Section 5.4.1 show it to be impractical. The third experiment tests whether satisfactory fibre bundle registrations can be found by converting the bundles to a simpler volume than the PDF described by Equation 3.1, in an attempt to reduce the computation time.

The final experiment investigates whether a global affine transformation can satisfy the alignment of the fibre bundles by combining all the bundles into one fibre image and converting this image to a volume. These new volumes are aligned using affine registration and this global affine transformation is applied to the fibre bundles. The results are compared with the volume-based local affine registrations to assess whether a simpler, faster, global affine registration produces results that are comparable to the local affine approach.

Chapter 4

Methodology

4.1 Resources

4.1.1 Experimental Data

The experiments required a collection of DTI images of the brain, each with a whole brain FA image as well as segmented fibre bundles from deterministic tractography. These data were provided by the Max Plank Institute (MPI) for Human Cognitive and Brain Sciences in Leipzig, Germany. The MPI provided scans of 10 healthy, normal adults. DWI and T_1 scans were obtained using a whole body Siemens 3-Tesla Trio scanner with an 8-channel head array coil. The DWI are produced by averaging three acquisitions to reduce random noise. Each had a $1.7mm$ isotropic resolution, and were acquired using a twice-refocused spin-echo echo-planar imaging sequence ($T_E = 100ms$, $T_R = 12s$, 128×128 image matrix, FOV $= 220mm \times 220mm$) taken from 60 directions with $b = 1000s.mm^{-1}$, GRAPPA/2 and NEX $= 3$. The T_1-weighted images were used for skull stripping and motion correction of the DWI images which were registered to the T_1 images with an isotropic resolution of $1mm$ using FSL.

Deterministic fibre tracking was performed for each DTI voxel using MedInria (Fillard *et al.*, 2007). The resulting whole brain tractography images were then manually segmented by an expert in neuroanatomy into 10 characteristic fibre bundles in the left hemisphere. Fibre bundles that are too large or have large angles in their trajectories, such as the corpus callosum, were segmented in parts, resulting in a total of 13 bundles which represent only 10 different structures per brain image. The fibre bundles are described in Table 4.1. This table shows summary statistics for each bundle and shows an example image of the bundle super imposed on a 3D rendering of the corresponding FA image. Figure 4.1 shows the variability in the number of fibres of corresponding bundles across the 10 brain images. There is clearly not a one-to-one relationship in terms of fibres.

As mentioned in Section 3.3, partially labelled images highlight correspondence and thus help to assess alignment. This is the reason for the segmented fibre bundles. The bundles allow the alignment of the internal structures to be assessed. This is important as human brains exhibit high variability not just in terms of the size and the outer shape of the brain, but also in terms of the structures within (Bjaalie, 2002). The bundles are also essential for the third experiment which finds a local affine transformation for each bundle.

Table 4.1: List of manually segmented fibre bundles including the average number of fibres per bundle and the average number of points per fibre within each bundle. The images are all of brain 9, used as the reference brain for the affine experiments.

Bundle Name	Abbreviation	Fibre Details	Image
Arcuate Fasciculus	ARC	Fibres: 898 Points: 108	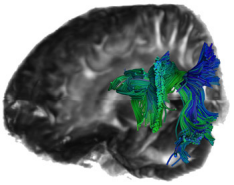
Anterior Thalamic Radiation	ATR	Fibres: 1502 Points: 93	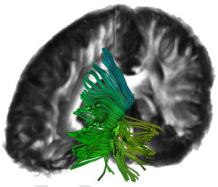
Corpus Callosum	CC1	Fibres: 3223 Points: 89	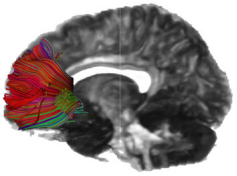
Corpus Callosum	CC2	Fibres: 4601 Points: 91	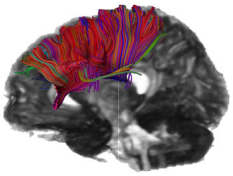
Corpus Callosum	CC3	Fibres: 3177 Points: 120	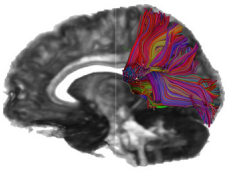
Cingulum	CIN1	Fibres: 744 Points: 83	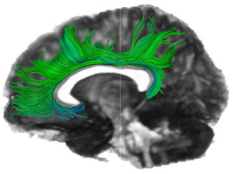
Cingulum	CIN2	Fibres: 127 Points: 72	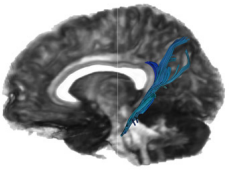

Table continues on next page

Table 4.1 continued: Details of test data.

Bundle Name	Abbreviation	Fibre Details	Image
Corticofugal Tract	CFT	Fibres: 2205 Points: 125	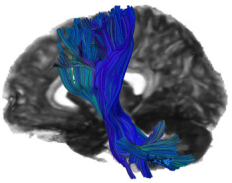
Inferior Fronto-Occipital Fasciculus	IFO	Fibres: 1532 Points: 156	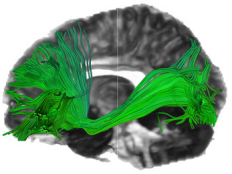
Inferior Longitudinal Fasciculus	ILF	Fibres: 1234 Points: 107	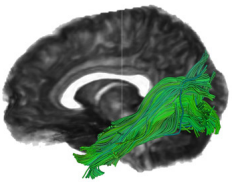
Superior Longitudinal Fasciculus	SLF	Fibres: 314 Points: 68	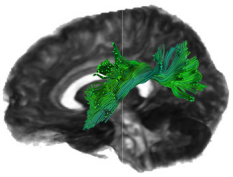
Superior Thalamic Radiation	STR	Fibres: 502 Points: 75	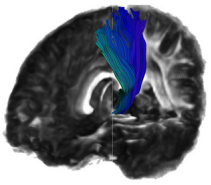
Uncinatus	UNC	Fibres: 337 Points: 79	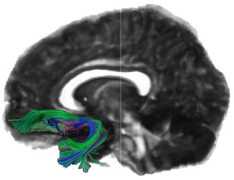

4.1.2 Computing Resources

The experiments were performed on a workstation with two Intel Xeon E5520 processors ($2.27GHz$, 4 cores, 8 threads) and $24GB$ RAM running Matlab R2009b 64 bit on Windows XP professional 64 bit. FSL, ART and MedInria (see Section 4.4.1) were run on this workstation in a 64 bit Ubuntu Linux distribution.

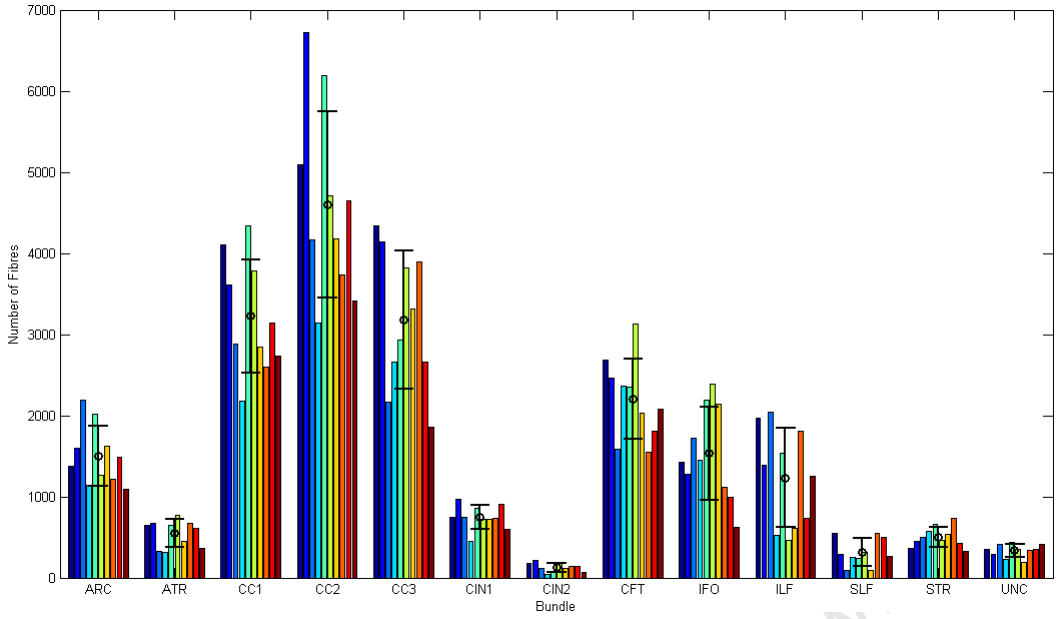

Figure 4.1: Variation of number of fibres per bundle across brain images. Error bars show the mean number of fibres per bundle as well as a single standard deviation in each direction.

4.2 Registration Techniques

Conventional registration techniques cannot be used on fibre data due to the fundamental differences between fibre images and regular images. Registration techniques are designed to work on voxel-based images. The fibre images are not represented in terms of voxels, but rather as strings of continuous 3D position vectors.

The implementation of a complete image registration algorithm is beyond the scope of this project, which reapplied transformations found using registrations of related voxel based images, referred to as the *base* registrations in this report. These base registrations are based on two types of images. The first are the FA images and the second are volumes derived from the fibre bundles themselves. A representative brain image is selected from the set of 10 brains as a reference image, rather than the use of a template image, as advised by Klein *et al.* (2010*a*).

The first two experiments use FA images for the base registration. Both the fibre images and the FA images are created from the same DTI images and are thus perfectly aligned. It is thus reasonable to assume that a transformation that aligns the FA images will also align the fibre images. The first experiment uses a nonlinear registration of the FA images as a base registration, the second uses an affine registration.

The third and fourth experiments use volumes derived from the fibre bundles for the base registrations and will be referred to as volume-based registrations. Techniques in the literature for converting fibre bundles into voxel-based images include creating binary volumes based on whether or not a voxel has a fibre point within it (Danielian *et al.*, 2010) or creating PDFs based on the points of the fibres (Ziyan *et al.*, 2007). The experiments here will use the former method as the PDF method was found to be too computationally expensive. The third experiment uses the binary volumes to find local affine transformations for each bundle. Ziyan *et al.* (2007) show that a global nonlinear transformation can be successfully created from the local affine transformations by forming a polyaffine transformation. The fourth experiment creates a single volume for each brain based on all the fibre bundles and uses this volume to find a single global affine

Table 4.2: A comparison of the experiments.

Experiment number	Registration class	Base registration	Purpose	Reference image
1	Nonlinear	FA images	Register the fibre images using a high DOF transformation in order to cope with the variability of the bundles and to provide a non-global method for comparison with experiment 3. A similar method of was implemented by Ziyan *et al.* (2007) as a means of comparison.	3
2	Global affine	FA images	A computationally simple alternative to experiment 1, this affine registration provides a base from which to compare the other methods. A similar method of was implemented by Ziyan *et al.* (2007).	9
3	Local affine	Bundle volumes	Re-examine the local affine registration performed by Ziyan *et al.* (2007) using alternatives to the computationally intensive PDF volumes.	9
4	Global affine	Combined bundle volumes	A second global affine registration provides a way to directly compare the FA-based methods with the volume-based methods by comparing against experiment 2. This also provides a computationally inexpensive alternative to experiment 3 depending on how great the loss of accuracy is.	9

transformation for each brain image. A global affine transformation would be a simpler and faster approach than finding a polyaffine transformation based on many local affine transformations. Thus experiment four will be deemed a success if the average alignment of each bundle is close to that of experiment three.

Experiments 1 - 3 are variations on fibre registrations reported by Ziyan *et al.* (2007), with the two FA-based registrations used as a basis of comparison for the volume-based local affine transformation. Experiment 4 offers an alternate form of comparison that is also volume-based, thus directly comparing local affine registration with global affine registration.

4.3 Selecting a Reference Image

To choose the most representative reference image, each of the 10 brain FA images was registered to each of the remaining 9, resulting in 90 registrations. The mean of the correlation and the mean of the mean absolute difference (MAD) was calculated for each potential reference image. The correlation and MAD are described in Section 4.8.1 and are given by Equations 4.11 and 4.12 respectively. The most representative image would be that with the highest mean correlation and lowest mean MAD.

4.4 Experiment 1: FA-based Nonlinear Registration

Figure 4.2 shows an overview of the process used for the FA-based nonlinear fibre registration. The process requires a source and a reference FA image as well as manually segmented fibre bundles from the source image. A nonlinear base registration is applied to the FA images to find a transformation. This transformation is then applied to the source fibre image to produce an output fibre image. This section first discusses the base registration used followed by a detailed explanation of the complex task of applying the transformation to a fibre image. This process is very computationally expensive and so

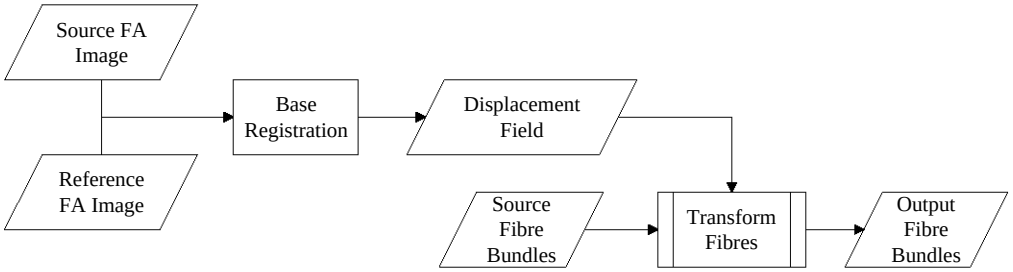

Figure 4.2: Overview of FA-based nonlinear registration of fibre images. A detailed flow chart of the *Transform Fibres* block is shown in Figure 4.7.

Table 4.3: Diffeomorphic demons parameters in used for the creation of base images in MedInria.

Parameter	Value
Interpolation	Trilinear
Use Histogram Matching	Yes
Number of Levels	4
Smooth Displacement Field	0.5
Smooth Update Field	1.00
Max. Step Length	4.00

this chapter ends by describing methods used to reduce the complexity and the time taken by the algorithm.

4.4.1 Base Registration

There is a wide variety of freely available tools that have implemented nonlinear registration algorithms specifically for use on brain MRI images. This work considers three notable implementations. These are the diffeomorphic demons algorithm implemented by MedInria (Fillard *et al.*, 2007), FNIRT by FSL (Andersson *et al.*, 2007) and 3DWarper by ART (Ardekani *et al.*, 2005). FNIRT was chosen because of the wide popularity of the FSL package as well as the use of FSL for some of the preprocessing stages, MedInria because it was used for the fibre tracking and DTI fitting, and ART because of its impressive performance as shown by Klein *et al.* (2009) in their rigourous investigation of over 14 tools. Figure 4.3 shows the results of the three tools using the experimental data for this project. It is clear from the difference images that MedInria performs best for this data and was thus the tool used to create the nonlinear base registrations. The parameters of the diffeomorphic demons tool in MedInria were adjusted based on inspection and set as shown in Table 4.3.

4.4.2 Nonlinear Fibre Registration

The transformation matrix from the diffeomorphic demons algorithm is in the form of a displacement field. The heads of the displacement vectors fall on a regular grid, i.e. the voxel locations of the output image, whereas the tails fall in continuous space and are associated with the source image. Trilinear interpolation of the source image at the location of a vector tail provides the intensity of the voxel on the output image at the vector head. Figure 4.4 illustrates this process for a single displacement vector.

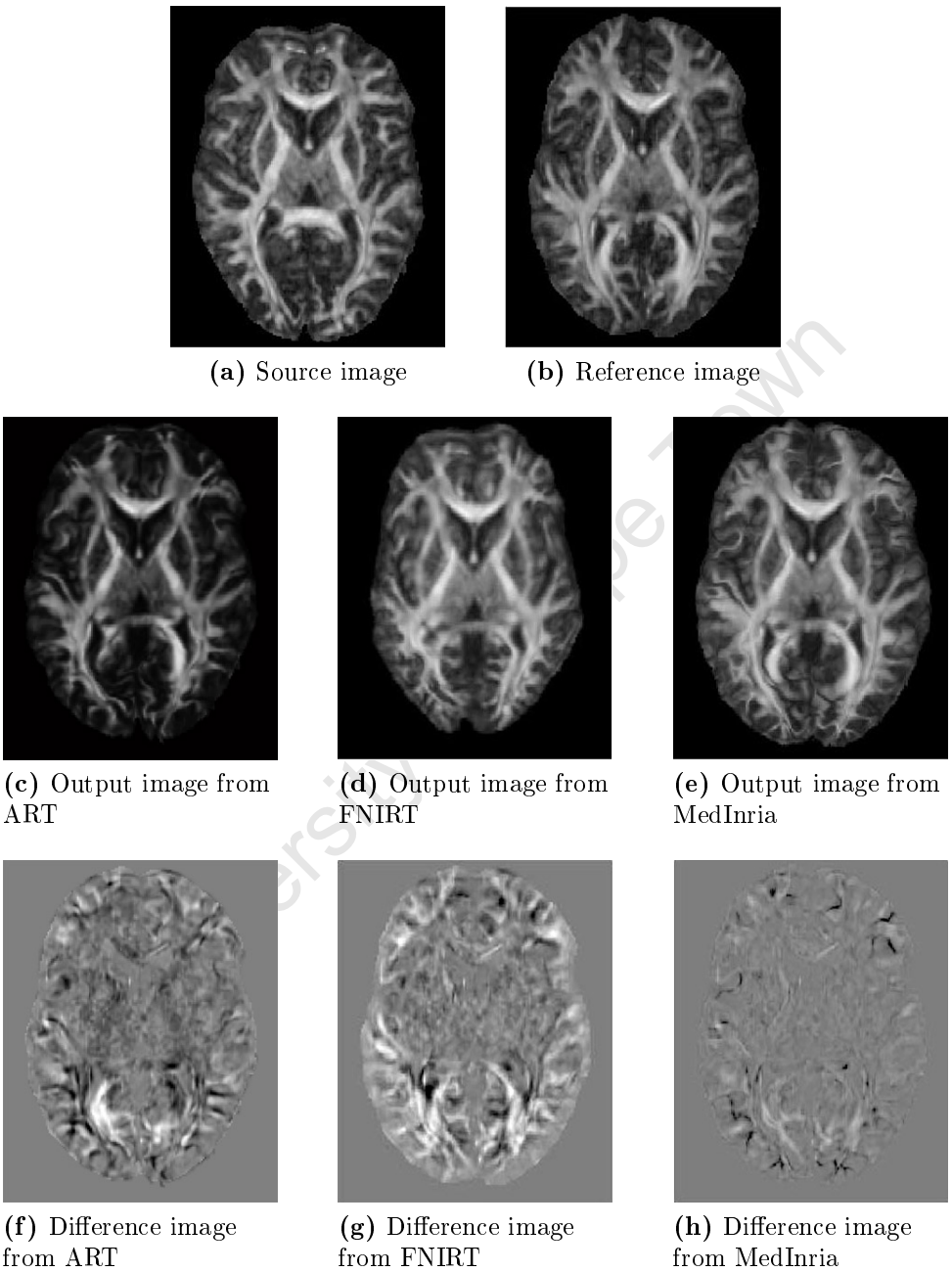

(a) Source image **(b)** Reference image

(c) Output image from ART **(d)** Output image from FNIRT **(e)** Output image from MedInria

(f) Difference image from ART **(g)** Difference image from FNIRT **(h)** Difference image from MedInria

Figure 4.3: Comparison of Nonlinear Registration Tools. Brain 1 is used as an example source image, similar results were found across the dataset. The reference image is brain 3.

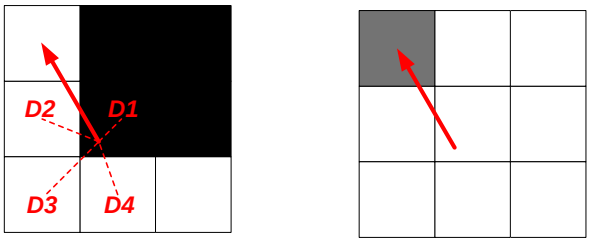

(a) Source image **(b)** Output image

Figure 4.4: An illustration of applying a single displacement vector from a demons transformation using trilinear interpolation. The head of the displacement vector falls in the centre of a voxel on the output image; the tail falls in between voxels on the source image, which necessitates interpolation.

Applying this displacement field to fibre images is a more complicated task. Fibre tracts can only be interpolated along their trajectories, thus if a vector tail falls anywhere other than exactly on the fibre path, interpolation of the fibre image is impossible. A novel solution to this problem is implemented where the displacement for each point on the fibre is found by interpolating the transformation matrix rather than the source image. This is further explained in Section 4.4.2.1.

4.4.2.1 Interpolating the Displacement Field

As the fibre images cannot be interpolated, the problem becomes that of interpolating the vector field, whose tails form an unstructured grid. The interpolation of vectors on an unstructured grid is tackled by Dovey (1995). The point of the fibre specifies the exact location required to be interpolated. A suitable neighbourhood of vectors must be identified for each point as it is impractical to interpolate using the entire field. A neighbourhood of four vectors is selected for each point by finding a Delaunay triangulation for the displacement field. Figure 4.5 shows how a neighbourhood of vectors is selected for a point on a fibre using Delaunay triangulation. The figure shown is two dimensional. The 3D images in this experiment would find four vectors creating a tetrahedron as the neighbouring vectors rather than the triangle of three vectors illustrated in the figure.

Background on Delaunay Triangulation and Barycentric Coordinates

Delaunay triangulation, in 3D, is the tetrahedral tessellation, $T(S)$, of the set of points S, within the convex hull of S, such that no point in S is within the circumsphere of any tetrahedron in $T(S)$ (Teng *et al.*, 1993). This tessellation, the dual graph of a Voronoi diagram, maximizes the minimum angle of all the tetrahedra in $T(S)$. This property makes the tetrahedra suitable neighbourhoods for the interpolation of any point within them.

The interpolation of a point within a tetrahedron is facilitated by the use of barycentric coordinates. The 2D case is used here to illustrate what barycentric coordinates are and how they are used to interpolate vectors at the vertices of an arbitrary simplex[1]. Barycentric coordinates refers to the three point coordinate system, four points in 3D, where each point is related to a vertex of a triangle. For the barycentric coordinates of a

[1] A simplex is the general term for a shape defined by the convex hull of n + 1 points in n-dimensional space. In 2 dimensions this is a triangle, in 3D it is a tetrahedron.

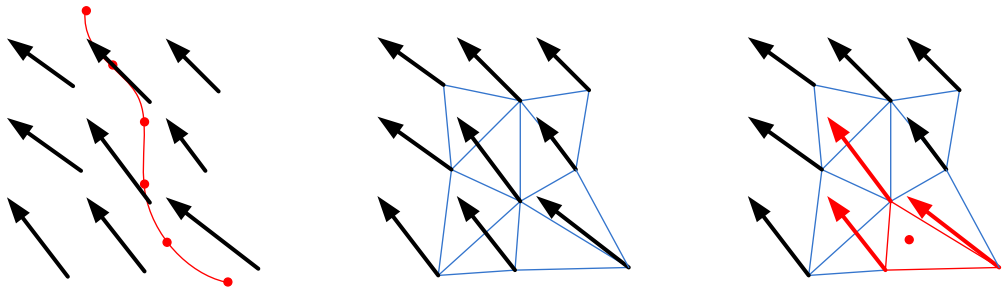

(a) The points of a fibre superimposed on a displacement field.

(b) Delaunay triangulation of the tails of a displacement field.

(c) A neighbourhood of vectors from which to interpolate the displacement of a fibre point.

Figure 4.5: Using Delaunay triangulation to find a suitable neighbourhood of vectors to interpolate for each point on a fibre. (a) shows a fibre in a displacement field. The red line indicates the trajectory along which the fibre itself can be interpolated. The displacement field is interpolated rather than the source fibre image as the tails of the vectors do not fall on this trajectory. (b) shows a Delaunay triangulation of the tails of a displacement field. Note that the heads of the vectors lie on a grid. (c) shows a point on a fibre and the correct neighbourhood of vectors (highlighted in red) from which to interpolate the displacement for that point. The vectors of this neighbourhood are those that define the vertices of the triangle, from Delaunay triangulation, in which the point of the fibre falls.

triangle ABC, an arbitrary point can be represented by the coordinates (a, b, c), such as in Figure 4.6. The value of a can be expressed as the ratio

$$a = \frac{AB - ||A - a_{AB}||}{AB} \tag{4.1}$$

where a_{AB} is the point of intersection of the line parallel to BC that passes through (a, b, c) and AB, as shown in Figure 4.6a. AC can be substituted for AB in Equation 4.1. The values of b and c can be determined in a similar fashion. Note that the values of a, b and c will lie between 0 and 1 for any point within the triangle, and $a + b + c = 1$ for any point. It is clear from Equation 4.1, that the barycentric coordinates for the vertex A are $(1, 0, 0)$. A line parallel to a side of the triangle will have a constant value for either a, b or c depending on which side it is parallel to. For example all points on a line parallel to BC will have that same a values.

The interpolation of a set of vectors at the vertices, i.e. $\vec{v}_A$, $\vec{v}_B$ and $\vec{v}_C$ to the point (a, b, c) becomes trivial and can be written as (Dovey, 1995)

$$\vec{v}_i = a\vec{v}_A + b\vec{v}_B + c\vec{v}_C \tag{4.2}$$

which easily generalizes to the interpolation of the point $(p_1, \ldots, p_n)$ in the n-dimensional simplex with vectors $\vec{v}_1, \ldots, \vec{v}_n$ at the vertices as

$$\vec{v}_i = \sum_{k=1}^{n} p_k \vec{v}_k \tag{4.3}$$

Figure 4.6b illustrates an interpolation of this type.

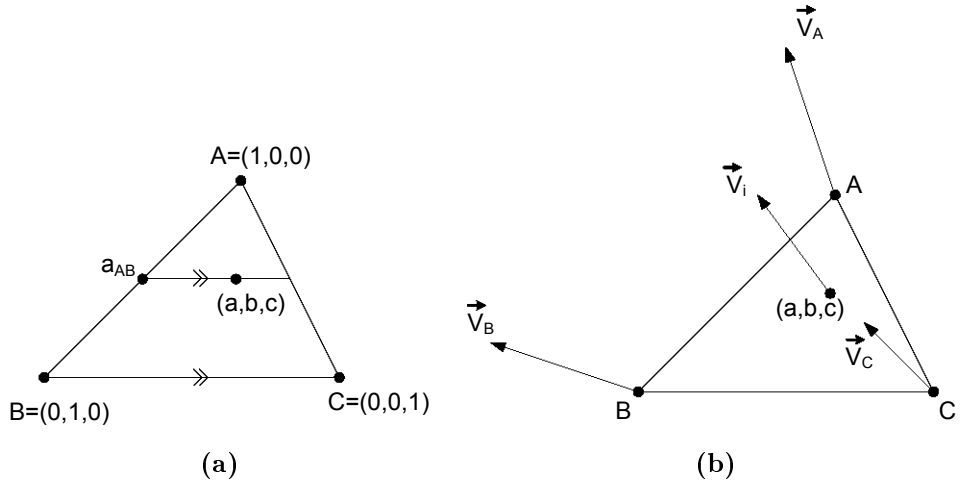

Figure 4.6: Barycentric Coordinates. (a) shows the barycentric coordinates of a triangle. Note that lines parallel to the side of a triangle have a constant value for the coordinate associated with the opposite vertex. In the image, the line shown is parallel to BC and therefore any point on the line will have the same value of a. This value can be calculated based on the ratio of how the line divides the sides it intersects with. (b) shows how barycentric coordinates can be used to interpolate vectors at the vertices of an arbitrary triangle. $\vec{v}_i$ in the image is defined by Equation 4.2.

Implementation of Displacement Field Interpolation

Figure 4.7 is a flow chart of the algorithm for the application of a transformation in the form of a displacement field to fibre images by interpolating the displacement field. A Delaunay triangulation is created from the unstructured grid of points made of the tails of the vectors in the displacement field. Each vector in the field is normalized to having its head on the origin, so it is necessary to first add the position vector of each voxel coordinate to its corresponding displacement vector. The Delaunay triangulation is computed in 3D using the `delauny3` function in Matlab based on the quickhull algorithm by Barber *et al.* (1996). Figure 4.5b shows a 2D, 3×3 example of this. The vectors are shown in black. Note that the vector heads lie on a grid. This is because they point to the output image voxel coordinates, however, they are stored as displacement vectors and thus the position vector of each voxel coordinate must be added to the corresponding vector or else the vector heads will all lie on the origin. The resulting Delaunay triangulation of the vector tails is shown in blue.

The next step is to ascertain the vertices of the tetrahedron, T, that the point, $\vec{p}$, on a fibre that is to be transformed falls into. This is done using Matlab's `tsearchn` function which outputs an index used to find the vectors at the 4 vertices, as well as the barycentric coordinates of $\vec{p}$ with respect to T. This function is illustrated in Figure 4.5c. The displacement vector at $\vec{p}$ is then interpolated using Equation 4.3. Note that the interpolation is performed on the normalized vectors, with their heads on the origin, rather than those with their position vectors added. Finally $\vec{v}_i$ is subtracted from $\vec{p}$ to give the transformed point, $\vec{p'}$. This process, illustrated in Figure 4.6b, is repeated for every point, on every fibre of every fibre bundle in the brain image.

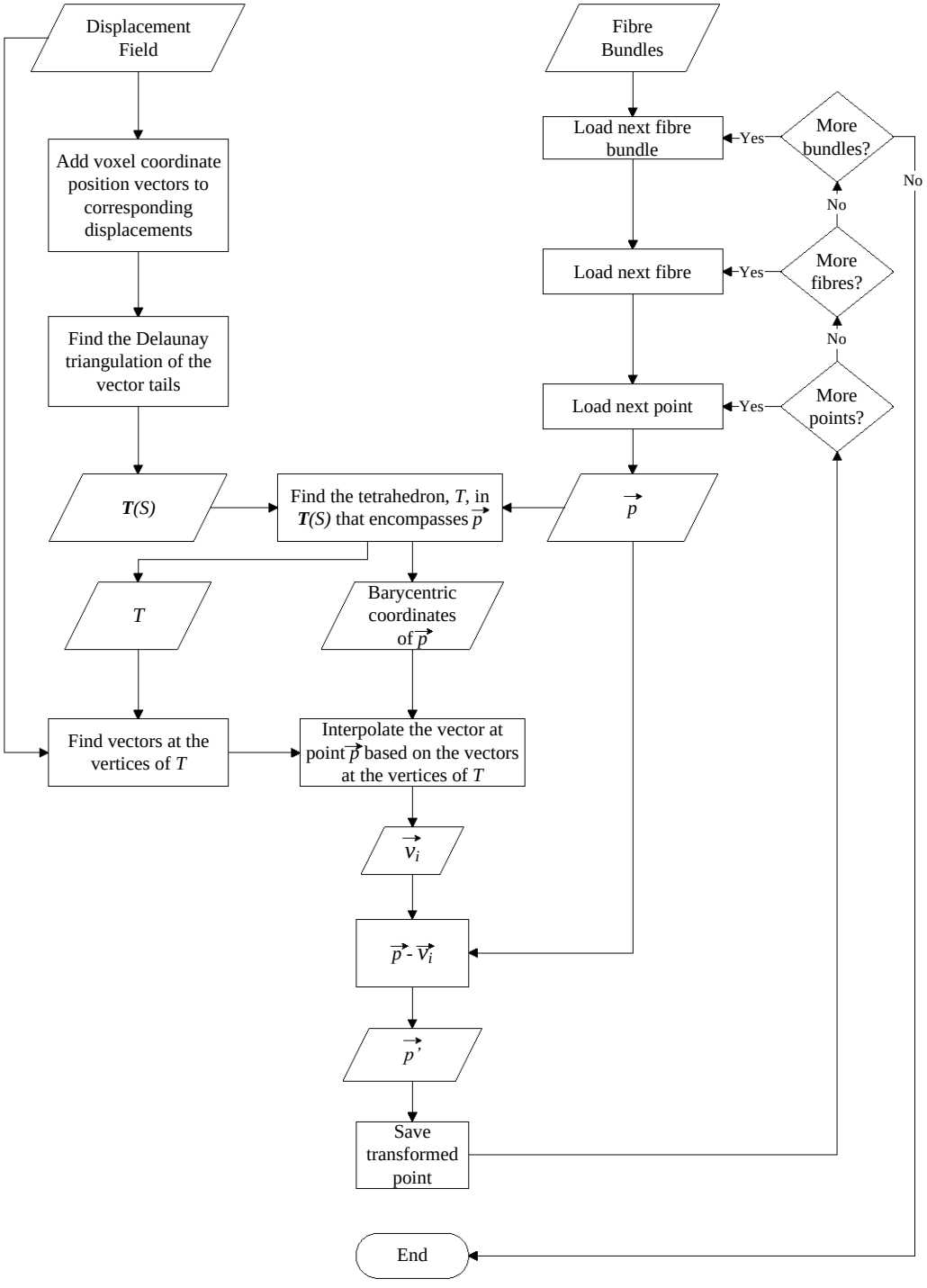

Figure 4.7: Flow chart of the algorithm used to apply a transformation in the form of a displacement field to fibre images.

4.4.2.2 Optimizing the Algorithm

Running the algorithm in Figure 4.7 for every point of every fibre takes an impractical amount of time[2] given the available computing resources described in Section 4.1.2. This section shows how the implementation was optimized to run in under 24 hours for the entire data set, using three approaches. The first is downsampling, the second is parallelization and the final approach is to break the displacement field into smaller local sections to accelerate the location of a specific tetrahedron.

Downsampling: Downsampling is applied on three fronts. The bundles are downsampled in terms of the number of fibres, the fibres are downsampled in terms of the number of points, and finally the displacement field itself is downsampled. Precedent is given for the downsampling of the fibres as well as the points in works such as that by O'Donnell and Westin (2007).

Parallelization: A further speed up is achieved through parallelization. The process described in Figure 4.7 is applied to each brain image, thus the loop that iterates through the brain images was set to run in parallel using Matlab's `parfor` function running 8 parallel workers. The reason for 8 workers, and not more, is because this is the limit for an individual Matlab workstation. The brain image iteration loop is parallelized in this experiment as it is the outer most loop, thus minimizing the overhead added due to parallelization. If this algorithm were to be run in a different setting, e.g. on a single brain image being registered, the loop that iterates through the fibre bundles could be parallelized instead. This way however, the generation of the warp fields would not benefit from the parallelization.

Sectioning the Displacement Field: Profiling the algorithm at run time shows that the majority of time is spent in Matlab's `tsearchn` function. This function searches through a list of tetrahedrons to find which one a given point lies within. The displacement fields for this dataset have dimensions of $160 \times 200 \times 160$, which after downsampling by 2 in each direction leaves 6.4×10^5 vectors. A Delanuay triangulation in 3D can result in up to $n^{3/2}$ tetrahedrons, where n is the number of points being triangulated. The reduction of this search space increases the speed of `tsearchn`. This is achieved by breaking the displacement field into smaller sections. The sections are made to overlap in order to prevent the tetrahedrons at the borders from being severed. The size of this overlap is set as the largest component of a displacement in the field. As the sections are rectangular, it is trivial to assign a point to the correct section. A separate Delaunay triangulation is found for each displacement field section. The search time of `tsearchn` is less in these sections than it is for the entire dataset.

4.5 Experiment 2: FA-Based Affine Registration

4.5.1 Base Registration

FSL's FLIRT is a widely used tool for the affine registration of brain images. Although the official documentation (Jenkinson *et al.*, 2002) does not describe the process required to apply the FLIRT transformation to the source image, a document by an author and

[2] Over 20 days per brain image.

developer of FLIRT (Jenkinson, ND) explains some of these details. The document differentiates between voxel and world coordinates, $\vec{x}_V$ and $\vec{x}_W$ according to $\vec{x}_W = \mathbf{D}\vec{x}_V$ where

$$\mathbf{D} = \begin{pmatrix} d_x & 0 & 0 & -o_x.d_x \\ 0 & d_x & 0 & -o_y.d_y \\ 0 & 0 & d_x & -o_z.d_z \\ 0 & 0 & 0 & 1 \end{pmatrix} \tag{4.4}$$

where d_x, d_y and d_z are the voxel dimensions in mm and (o_x, o_y, o_z) are the voxel coordinates of the world origin. However the document does not mention how FLIRT deals with q-forms or s-forms, i.e. the co-ordinate mappings provided in the file headers. The same output image as FLIRT cannot be produced by applying the transformation to the source image either directly or with Equation 4.4, with the centre of rotation in the corner as suggested, in the centre of the image or at the centre of mass of the image. A similar problem was encountered when trying to reapply the affine transformation from the affine registration options of MedInria, ART and SPM.

B-spline Grid, Image and Point based Registration (Kroon, 2008) is a Matlab tool available on the file exchange with the capability to perform affine registration on 3D images. Unlike the tools designed specifically for brain images, it does not consider the nifti file header. Reapplying the transformation to the source image reproduces the output image exactly. This transformation assumes the centre of rotation is at the centre of the image. This Matlab tool is used for all affine registrations, not only in this experiment but in those of Sections 4.6 and 4.7 as well.

4.5.2 Affine Fibre Registration

Applying the affine transformations, $\mathbf{A}$, produced by the base registration to the source fibre is a far simpler task than applying the nonlinear transformations. The affine transformation is global as opposed to the voxel based nonlinear transformation, and so the problem of interpolation no longer applies. A transformed output point, $\vec{p'}$, can be found by multiplying the inverse of the transformation by $\vec{p}$, a point on a fibre in the source image

$$\vec{p'} = \mathbf{A}^{-1}\vec{p} \tag{4.5}$$

The transformation matrix assumes that the centre of rotation is at the centre of the image, thus half of each image dimension, i.e. half the number of voxels that the image spans in each direction, must be subtracted from $\vec{p}$ before the transformation is applied and added after. Thus Equation 4.5 becomes

$$\vec{p'} = \mathbf{A}^{-1}(\vec{p} - \vec{N}_{1/2}) + \vec{N}_{1/2} \tag{4.6}$$

where $\vec{N}_{1/2}$ is the vector of half the number of voxels of the image in the x, y and z directions[3], i.e. $\vec{N}_{1/2} = (80, 100, 80, 1)^T$. Downsampling is unnecessary this time as this process is not computationally intensive.

[3]Note that the vectors $\vec{p}$, $\vec{N}_{1/2}$ and $\vec{p'}$ are all augmented with 1 as in Equation 2.7

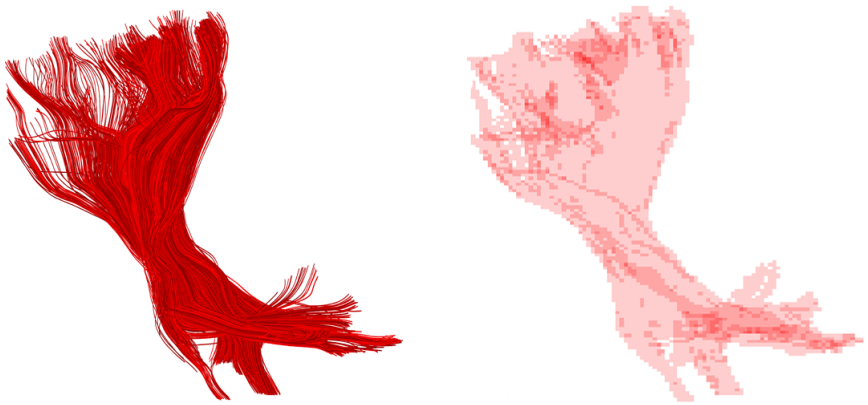

(a) Fibre Bundle **(b)** Binary Volume

Figure 4.8: A fibre volume and its corresponding binary volume.

4.6 Experiment 3: Volume-Based Local Affine Registration

4.6.1 Converting Fibres to Volumes

Ziyan *et al.* (2007) found local affine transformations by registering single fibre bundles from the source image to their corresponding fibre bundles from the reference image. To do this, the fibre bundles were converted to PDFs according to Equation 3.1, which is a highly computationally expensive procedure. This experiment aims to investigate whether converting the fibre bundles to binary volumes instead of PDFs is suitable for the base registration.

The binary volumes are composed of those voxels that contain a fibre point. No distinction is made between voxels that contain a single fibre point and those containing many points. Figure 4.8 shows a fibre bundle and the binary volume derived from it.

A brute force calculation of the PDF is slow. An extremely close approximation can be found in an eighth of the time. This is done by creating a volume, V_{b_i}, where each voxel is assigned an intensity equal to the number of points that fall in it. Equation 3.1 can then be approximated as

$$\mathbf{P}_{b_i}(\vec{x}) \approx \frac{1}{Z} \sum_{\vec{v}_j \in V_{b_i}} V_{b_i}(\vec{v}_j)\kappa(\vec{x} - \vec{v}_j) \tag{4.7}$$

where $\vec{v}_j$ is a voxel coordinate of V_{b_i}. Clearly for voxels that contain no points, $V_{b_i}(\vec{v}_j) = 0$, it is unnecessary to calculate the Gaussian kernel function in Equation 4.7. This reduces the number of kernel function calculations from the number of points in the fibre bundle down to the small number of voxels that the points fit into.

4.6.2 Base and Fibre Registrations

The base registrations use the same reference brain image as the FA-based affine registrations and are registered using the same Matlab code. However, unlike the FA-based affine registrations, each bundle of each source brain image will be registered to the corresponding bundle on the reference brain image. Thus 117 registrations[4] are required as

[4] 117 registrations are required because there are 9 images with 13 bundles each.

opposed to 9 required for the other three experiments. To reduce the time taken for the registrations, the bundle volumes are downsampled by breaking the image into sub-images of $4 \times 4 \times 4$ voxels each and treating these sub-images as a single voxel with intensity equal to the average intensity of the 64 voxels within the sub-image.

The affine transformation matrices of the downsampled images are the same as for the full sized images except for the translation parameters, which need to be scaled up by the same factor by which each image was downsampled in each direction. For example if the downsampled transformation matrix is

$$\mathbf{A}_{downsampled} = \begin{pmatrix} l_{11} & l_{12} & l_{13} & t_x \\ l_{21} & l_{22} & l_{23} & t_y \\ l_{31} & l_{32} & l_{33} & t_z \\ 0 & 0 & 0 & 1 \end{pmatrix} \tag{4.8}$$

then it must be transformed before it can be applied to a full sized image to be

$$\mathbf{A} = \begin{pmatrix} l_{11} & l_{12} & l_{13} & 4t_x \\ l_{21} & l_{22} & l_{23} & 4t_y \\ l_{31} & l_{32} & l_{33} & 4t_z \\ 0 & 0 & 0 & 1 \end{pmatrix} \tag{4.9}$$

The fibre registration can then be done by simply applying Equation 4.6 to each point of each fibre of the fibre bundle. Note that a different local affine transformation is used for each fibre bundle.

4.7 Experiment 4: Volume-Based Global Affine Registration

The binary volumes of each fibre bundle from an image are combined to create one binary volume per brain image. One such volume is shown in Figure 4.9. In other words, the volume in Figure 4.9 is a combination of the volumes created using each bundle listed in Table 4.1 for a given subject. These volumes are registered to the reference brain image using Matlab. The volumes are not downsampled prior to the registration as only 9 registrations are required. The fibre registration is done according to Equation 4.6, using the global affine transformation of each brain image for all the fibre bundles of that image.

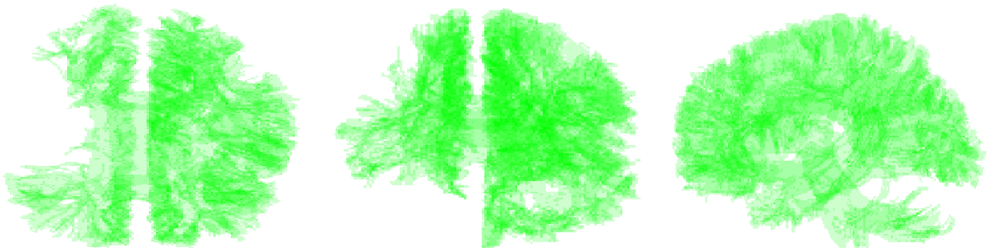

(a) x-y view **(b)** x-z view **(c)** y-z view

Figure 4.9: Binary volume from all the fibre bundles of a brain image. The asymmetry is the result of only using fibre bundles in the left hemisphere, as mention in Section 4.1.1.

4.8 Evaluation of Registrations

4.8.1 Base Registrations

Each experiment found the transformations to apply to the fibre bundles by using a conventional registration tool on scalar images. The FA-based registrations are validated visually using difference images as described in Section 2.3.4.. These registrations are also validated quantitatively using two metrics.

The first is the Pearson correlation coefficient defined as

$$R_{\mathbf{SR}} = \frac{C(\mathbf{S},\mathbf{R})}{\sqrt{C(\mathbf{S},\mathbf{S})}\sqrt{C(\mathbf{R},\mathbf{R})}} \tag{4.10}$$

where $C(\mathbf{S},\mathbf{R})$ is the covariance of the source image, $\mathbf{S}$ and the reference image, $\mathbf{R}$. In terms of discrete images Equation 4.10 can be calculated as

$$R_{\mathbf{SR}} = \frac{n\sum_{\vec{x}} s_{\vec{x}} r_{\vec{x}} - \sum_{\vec{x}} s_{\vec{x}} \sum_{\vec{x}} r_{\vec{x}}}{\sqrt{n\sum_{\vec{x}} s_{\vec{x}}^2 - \left(\sum_{\vec{x}} s_{\vec{x}}\right)^2}\sqrt{n\sum_{\vec{x}} r_{\vec{x}}^2 - \left(\sum_{\vec{x}} r_{\vec{x}}\right)^2}}. \tag{4.11}$$

where $\vec{x}$ is a vector describing the voxel coordinates and $s_{\vec{x}}$ and $r_{\vec{x}}$ are the intensities of images $\mathbf{S}$ and $\mathbf{R}$ at voxel $\vec{x}$.

The second is the mean absolute difference (MAD) of the two images and is described by the equation

$$MAD_{\mathbf{SR}} = \frac{1}{N}\sum_{\vec{x}} |s_{\vec{x}} - r_{\vec{x}}| \tag{4.12}$$

where N is the total number of voxels.

The volume-based registrations are assessed visually as well. Each registration is shown from the point of view of the x-y-plane, the x-z-plane and the y-z-plane so that the alignment can be observed in three dimensions[5]. The success of the registrations is quantified using six volume similarity metrics. These are the Pearson correlation coefficient, four different overlap measures (Klein *et al.*, 2009) and Cohen's Kappa (Landis and Koch, 1977). The choice to compare six metrics stems from the fact that there is no standard measure of volume similarity being used in the DTI literature. The four overlap metrics are the target overlap, $T_{\mathbf{SR}}$, the source overlap, $S_{\mathbf{SR}}$, the mutual overlap, $M_{\mathbf{SR}}$, and the union overlap, $U_{\mathbf{SR}}$. These are described by the following equations, which are shown visually in Figure 4.10:

$$\begin{aligned} T_{\mathbf{SR}} &= \frac{|\mathbf{S}\cap\mathbf{R}|}{|\mathbf{R}|}, & S_{\mathbf{SR}} &= \frac{|\mathbf{S}\cap\mathbf{R}|}{|\mathbf{S}|}, \\ M_{\mathbf{SR}} &= 2\frac{|\mathbf{S}\cap\mathbf{R}|}{|\mathbf{S}|+|\mathbf{R}|}, & U_{\mathbf{SR}} &= \frac{|\mathbf{S}\cap\mathbf{R}|}{|\mathbf{S}\cup\mathbf{R}|} \end{aligned} \tag{4.13}$$

Cohen's Kappa is traditionally a statistical measure of repeatability used with categorical data. Wakana *et al.* (2007) and Voineskos *et al.* (2009) describe a method to use Cohen's Kappa to measure the similarity of two fibre bundles. This is done by converting

[5]These three points of view are snapshots from 3D matlab figures. In Matlab the figures can be freely rotated facilitating excellent visual assessment of 3D alignment. The snapshots are used for display purposes only in this report as the rotatable 3D images are obviously not an option here.

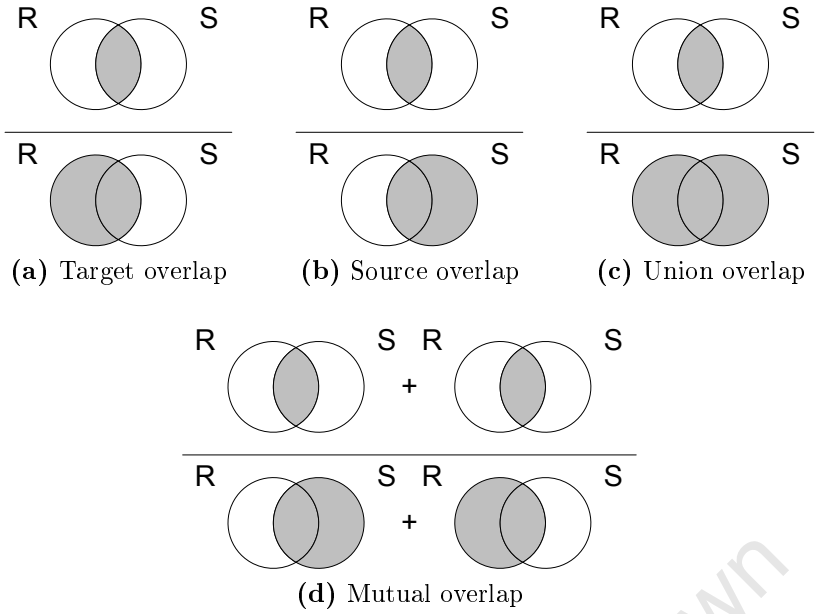

(a) Target overlap **(b)** Source overlap **(c)** Union overlap

(d) Mutual overlap

Figure 4.10: Visualization of overlap metrics.

each bundle to a binary volume exactly as described in Section 4.6.1. Voxels are divided into 4 categories namely those that are empty in both images, the sum of which defines S_{nn}, those that contain a tract in both images whose sum is S_{pp}, those that contain a tract in the source image but not the reference image, S_{np}, and those containing tracts in the reference image but not the source, S_{pn}. The number of voxels expected to be empty is then defined as $E_{nn} = (S_{nn} + S_{np})(S_{nn} + S_{pn})/N$ and the number expected to contain tracts is $E_{pp} = (S_{pp} + S_{np})(S_{pp} + S_{pn})/N$, where N is the total number of voxels in each image. Observed agreement (OA) is $(S_{nn} + S_{pp})/n \times 100$ and expected agreement (EA) is $(E_{nn} + E_{pp})/n \times 100$. Cohen's Kappa is then given as

$$\kappa = \frac{OA - EA}{100 - EA} \tag{4.14}$$

For consistency, κ will be denoted $K_{\mathbf{SR}}$ in this paper. Although Wakana *et al.* (2007) and Voineskos *et al.* (2009) use this metric to measure reproducibility in fibre bundle tracking and segmentation, it provides a method to measure the similarity of binary volumes which accounts for the probability of the volumes overlapping by chance.

4.8.2 Fibre Registrations

There is no standard metric for fibre bundle similarity. It is pointless comparing individual fibres, firstly as corresponding bundles in different brain images do not have the same number of fibres, as shown in Figure 4.1, and secondly because of the uncertainty inherent in the DTI and tractography processes the fibres only carry reliable information when considered in groups.

To assess bundle similarity, each fibre bundle is converted to a binary volume using the method described in Section 4.6.1. A similar method was used by Danielian *et al.* (2010). The similarity of these binary volume images is measured using the six metrics detailed Section 4.8.1 of this chapter.

Visual validation of alignment is performed on both the fibre bundles and the volumes derived from them. The fibre bundles are plotted in Matlab where the colour of each

fibre in the bundle is very slightly, randomly perturbed from a base colour to allow the individual fibres to be discerned. The fibre bundles are downsampled to include only 1 in every 5 fibres and the fibres downsampled to show only 1 in every 5 points, unless otherwise specified, due to memory considerations as well as ease of viewing.

Chapter 5

Results

This chapter presents the results from the experiments described in Chapter 4. The chapter begins with the results from the base registrations of the four experiments followed by the results of the fibre registrations. Further investigations into experiments 1 and 3 are undertaken based on these results. The chapter ends with tables and figures summarizing and comparing the four methods.

All registration results are presented as alignment or similarity metrics of the output images with the reference images. In all cases these results are contrasted against the alignment of the source image with the reference image. This provides an indication of the improvement of alignment that the registration has afforded against the alignment prior to registration.

The overlap metrics are calculated for the source and reference image as well as the output and reference images for each bundle of each brain. This yields over 1400 separate results for the 6 metrics applied to the 13 bundles of the 9 brains being registered. It is impractical to present such a large number of results for each experiment.

A summary of the results for each section is presented in the form of bar charts of means. For each of the base registration and the fibre registrations, a chart showing the average result of each bundle across all brains as well as a chart showing the average result of each brain across all bundles is presented. The values on the charts are of the difference of each metric applied before and after the registration. For example the correlation coefficients in the graphs are actually the difference between the correlation of the output image and the reference image with the correlation of the source image and the reference image, i.e. $R_{\mathbf{OR}} - R_{\mathbf{SR}}$. All the metrics are presented this way. Thus the graphs show the improvement of alignment after registration. The mean value for all bundles in all brains is shown on the charts for each metric as well as error bars showing one standard deviation for the data in each group of bars. The similarity metrics are indicated as follows in the graphs: R = correlation; T = target overlap; S = source overlap; M = mutual overlap; U = union overlap and K = Cohen's Kappa. Tables of the values used to create these charts are presented in Appendix A.

5.1 Base Registrations

This section presents the results of the base registrations of experiments 1 - 4. The results of the choice of reference images are presented first followed by the results of the base registrations themselves.

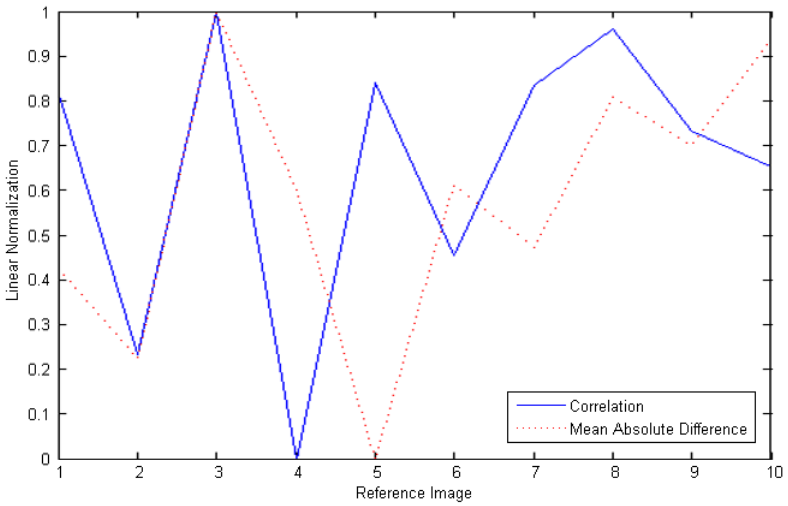

Figure 5.1: A comparison of each image used as a reference image for nonlinear registration, used to select a reference image for the experiments. Image 3 was selected.

Figure 5.1 and Figure 5.2 present the results of the method described in Section 4.3 used to choose a reference image. The data has been linearly normalized so that the lowest mean correlation is set to 0 and the highest to 1 whereas the lowest mean MAD is set to 1 and the highest to 0. This allows both measures to be easily compared on the same set of axes, with the reference image that has a value of 1 being the most successful for both metrics. Based on the results, brain image 3 was selected as the reference image for all the nonlinear registrations and brain image 9 was selected as the reference image for all the affine registrations.

Experiments 1 and 2 use FA images for the base registration. Figure 5.3 and Figure 5.4 show visualizations of the base registrations as difference images to indicate the improvement achieved with registration. Figure 5.5 shows the results of experiment 3 compared against the source images. The figure shows a single bundle as an example of the 117 registrations performed. Volumes of all the bundles are combined to form a single volume per brain image for the base registrations in experiment 4. Figure 5.6 shows a visualization of these volumes before and after registration. The results of the FA-based base registrations are quantified using correlation and MAD. These results are shown in Figure 5.7 and Figure 5.8. The base registrations of the volume-based experiments are quantified using the six metrics described in Section 4.8.2, the results of which are shown in Figure 5.9 and Figure 5.10.

5.2 Fibre Registrations

The fibre registrations are visualized by presenting a single bundle superimposed on its corresponding reference bundle for each experiment. The visualizations are shown as both volumes and as fibre bundles. The arcuate fasciculus is used as an exemplar. Figure 5.11 shows the source images for comparison with the registered images for each section. Figures 5.12 - 5.15 show visualizations for experiments 1 - 4 respectively.

Figures 5.16 - 5.19 show bar charts of the quantitative results of the fibre registrations for experiments 1 - 4 respectively.

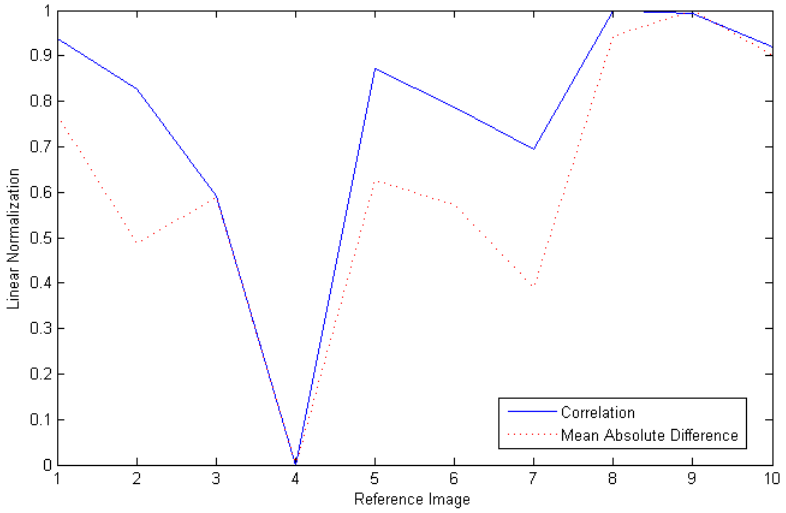

Figure 5.2: A comparison of each image used as a reference image for affine registration, used to select a reference image for the experiments. Image 9 was selected.

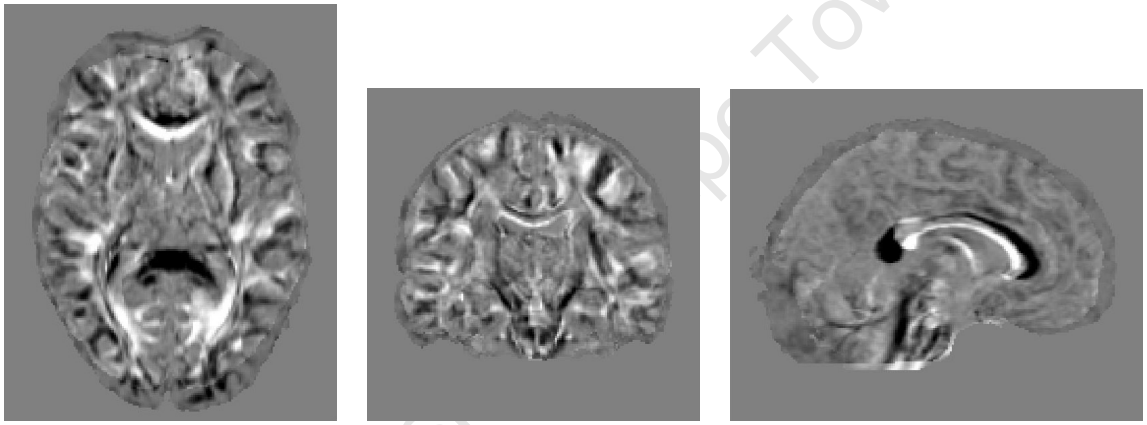

(a) Difference image of reference and source, x-y-plane

(b) Difference image of reference and source, x-z-plane

(c) Difference image of reference and source, y-z-plane

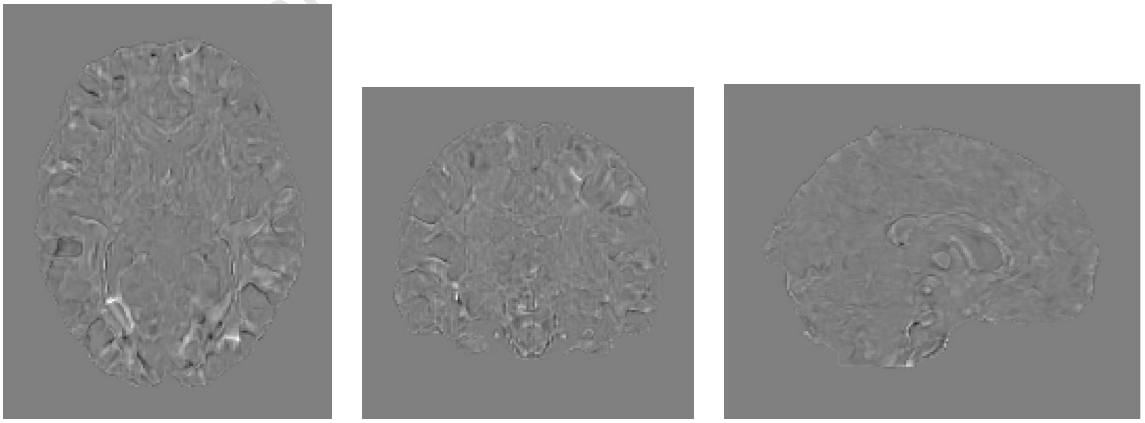

(d) Difference image of reference and output, x-y-plane

(e) Difference image of reference and output, x-z-plane

(f) Difference image of reference and output, y-z-plane

Figure 5.3: Example results of base registration for Experiment 1. Difference image of the FA reference image, brain 3, and the FA source image, brain 1, compared with difference image of the FA reference image and the FA output image from nonlinear registration.

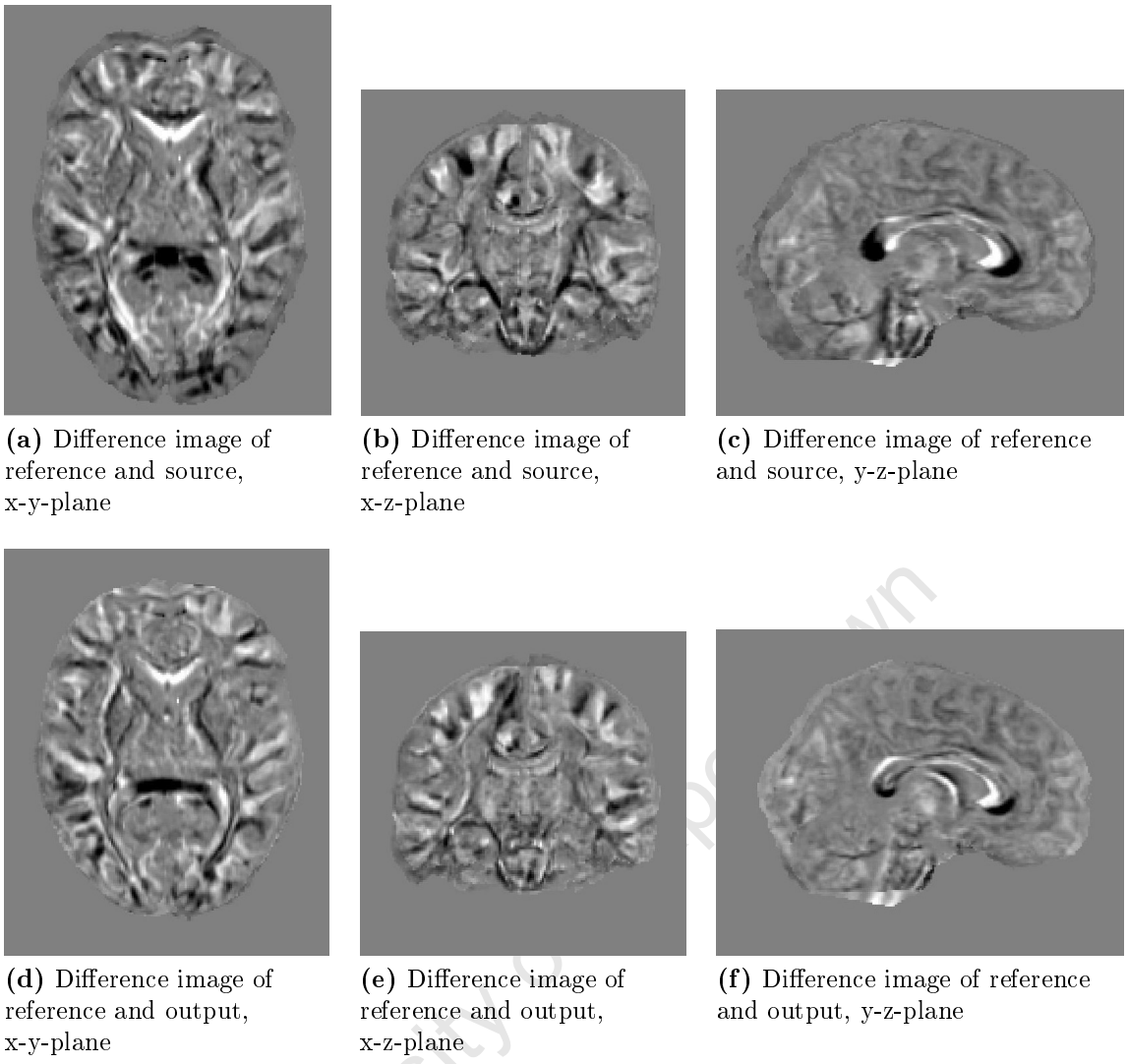

(a) Difference image of reference and source, x-y-plane

(b) Difference image of reference and source, x-z-plane

(c) Difference image of reference and source, y-z-plane

(d) Difference image of reference and output, x-y-plane

(e) Difference image of reference and output, x-z-plane

(f) Difference image of reference and output, y-z-plane

Figure 5.4: Example results of base registration for Experiment 2. Difference image of the FA reference image, brain 9, and the FA source image, brain 1, compared with difference image of the FA reference image and the FA output image from affine registration.

5.3 Further Investigations into Experiment 1

5.3.1 Results of Optimizing the Algorithm

This section presents some of the numerical results and parameters used to implement the optimization approaches described in Section 4.4.2.2.

Only one in every ten fibres is used and only one in every ten points per fibre are used, giving a total downsampling of 100. Figure 5.20 shows a fibre bundle before and after this downsampling. Although the effect of the downsampling seems severe, there are 1500 fibres on average per bundle with 95 points on the average fibre. This leaves a total of over 2 million 3D vectors per image, an unnecessarily large amount for many applications.

The displacement field is downsampled by taking every second vector in each direction, a total downsampling of 8. Figure 5.21 shows the effect of this downsampling by considering the Z component of the displacements of an x-y-plane. The images show that the sampling does not distort the field in a manner that would affect interpolation.

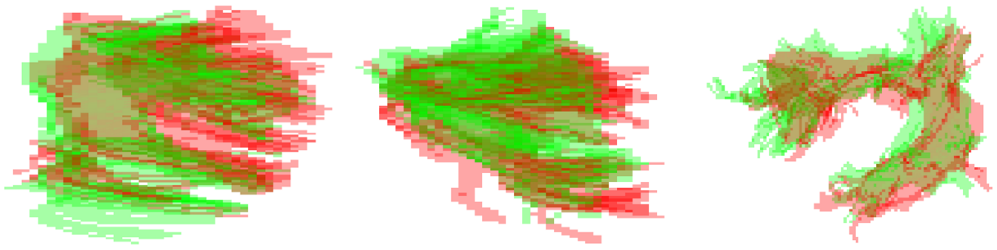

(a) $\mathbf{V}_r$ & $\mathbf{V}_s$, x-y-plane **(b)** $\mathbf{V}_r$ & $\mathbf{V}_s$, x-z-plane **(c)** $\mathbf{V}_r$ & $\mathbf{V}_s$, y-z-plane

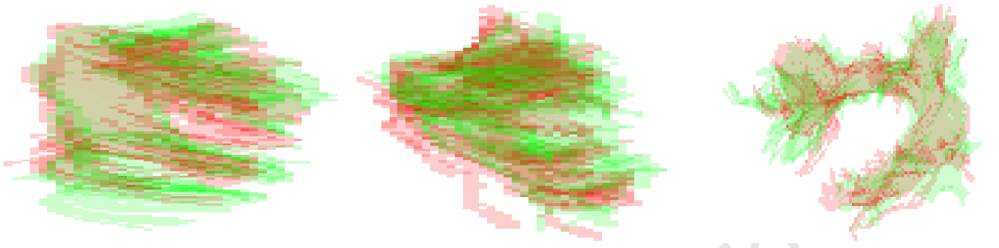

(d) $\mathbf{V}_r$ & $\mathbf{V}_o$, x-y-plane **(e)** $\mathbf{V}_r$ & $\mathbf{V}_o$, x-z-plane **(f)** $\mathbf{V}_r$ & $\mathbf{V}_o$, y-z-plane

Figure 5.5: Example results of base registration for Experiment 3. Volume-based local affine base registration output volume, $\mathbf{V}_o$, in red (brain 1), superimposed on reference volume, $\mathbf{V}_r$, in green (brain 9).

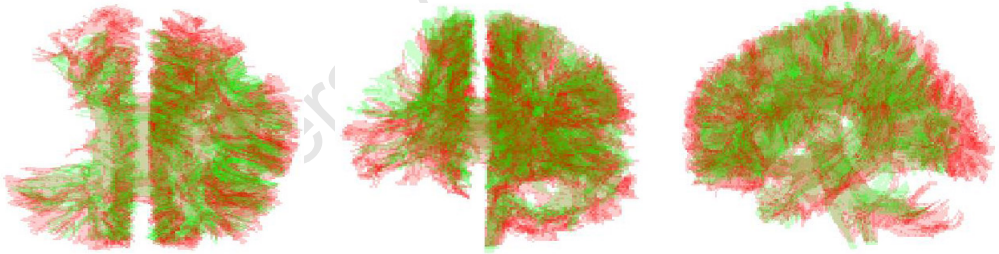

(a) $\mathbf{V}_r$ & $\mathbf{V}_s$, x-y-plane **(b)** $\mathbf{V}_r$ & $\mathbf{V}_s$, x-z-plane **(c)** $\mathbf{V}_r$ & $\mathbf{V}_s$, y-z-plane

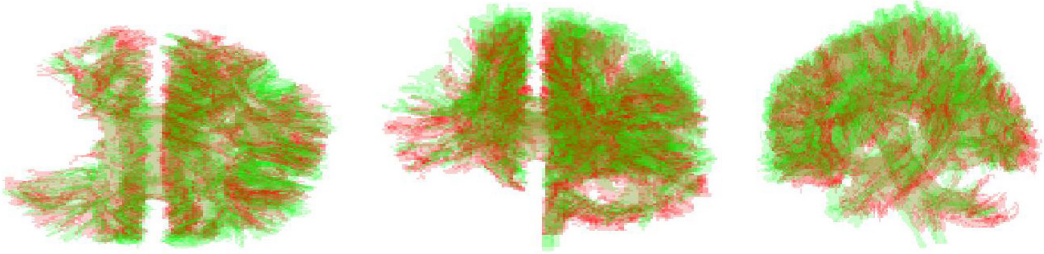

(d) $\mathbf{V}_r$ & $\mathbf{V}_o$, x-y-plane **(e)** $\mathbf{V}_r$ & $\mathbf{V}_o$, x-z-plane **(f)** $\mathbf{V}_r$ & $\mathbf{V}_o$, y-z-plane

Figure 5.6: Example results of base registration for Experiment 4. Volume-based global affine base registration output volume, $\mathbf{V}_o$, in red (brain 1) superimposed on reference volume, $\mathbf{V}_r$, in green (brain 9).

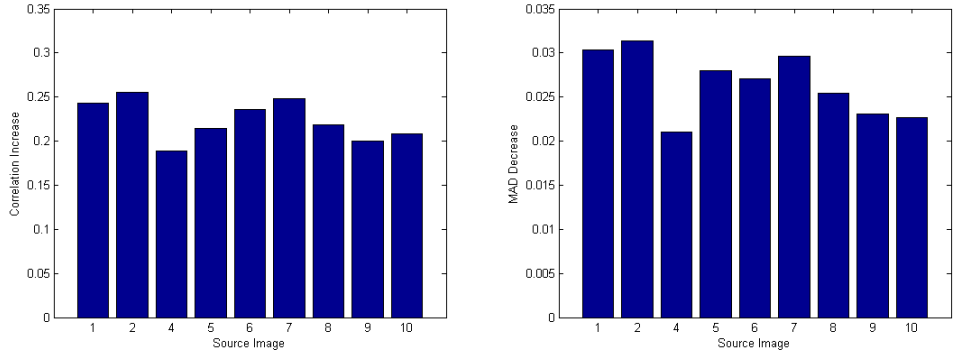

(a) (b)

Figure 5.7: Results of base registrations for Experiment 1. Improvement of FA image alignment after FA-based nonlinear base registrations. (a) shows the increase in correlation and (b) shows the decrease in mean absolute difference.

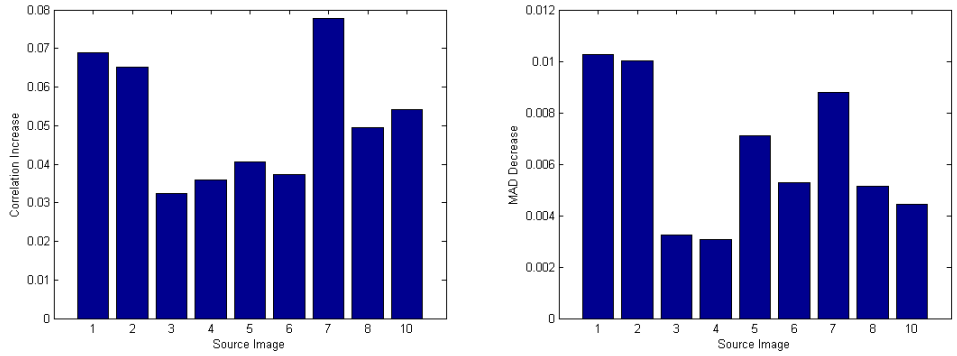

(a) (b)

Figure 5.8: Results of base registrations for Experiment 2. Improvement of FA image alignment after FA-based affine base registrations. (a) shows the increase in correlation and (b) shows the decrease in mean absolute difference.

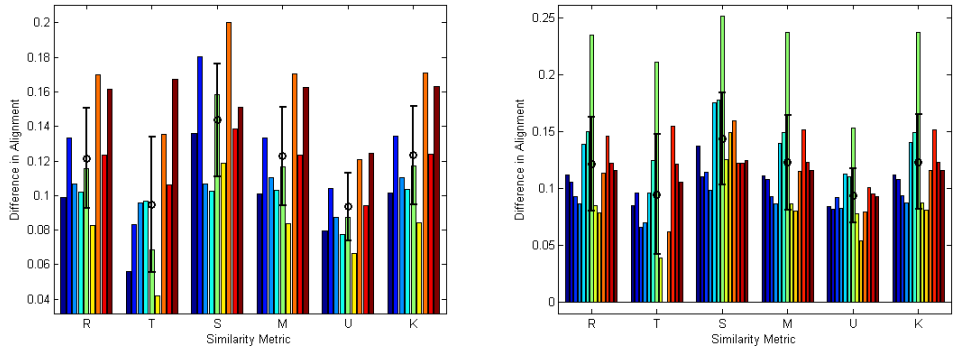

(a) (b)

Figure 5.9: Results of base registrations for Experiment 3. Improvement of bundle volume similarity after volume-based local affine base registrations. (a) shows the mean values for all bundles per brain and (b) shows the mean values for all brains per bundle.

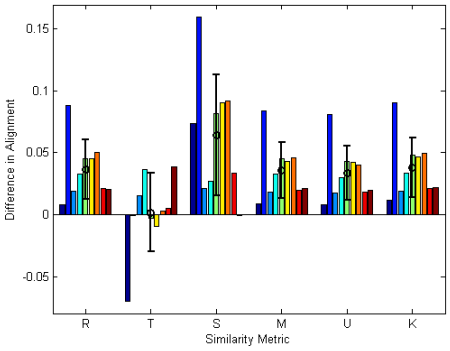

Figure 5.10: Results of base registrations for Experiment 4. Improvement of whole brain volume similarity after volume-based global affine base registrations.

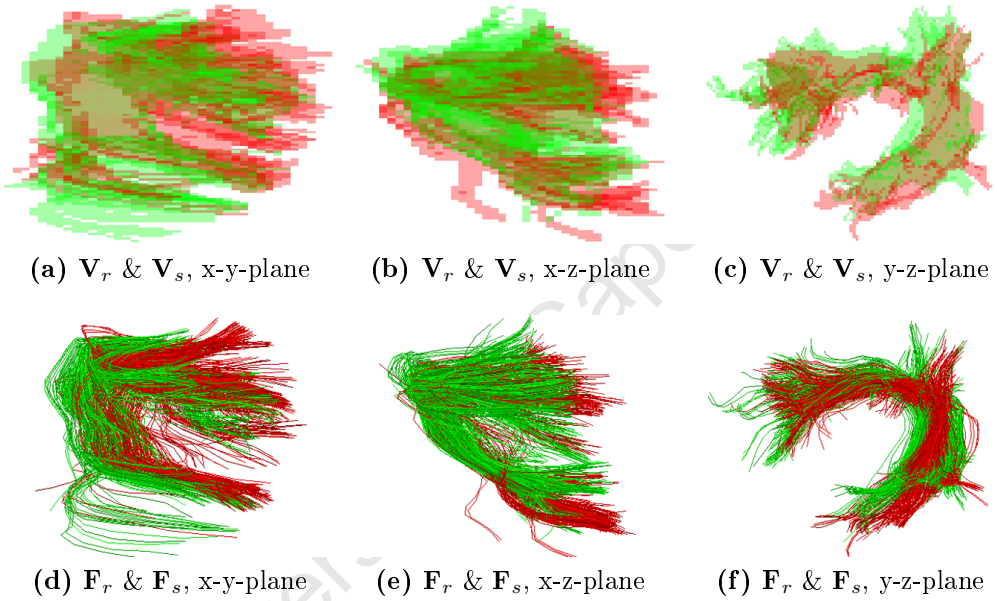

(a) $\mathbf{V}_r$ & $\mathbf{V}_s$, x-y-plane **(b)** $\mathbf{V}_r$ & $\mathbf{V}_s$, x-z-plane **(c)** $\mathbf{V}_r$ & $\mathbf{V}_s$, y-z-plane

(d) $\mathbf{F}_r$ & $\mathbf{F}_s$, x-y-plane **(e)** $\mathbf{F}_r$ & $\mathbf{F}_s$, x-z-plane **(f)** $\mathbf{F}_r$ & $\mathbf{F}_s$, y-z-plane

Figure 5.11: Source image, brain 1, fibres and volumes (red) superimposed on reference image, brain 9, fibres and volumes (green). $\mathbf{V}_r$ is the reference volume, $\mathbf{V}_s$ is the source volume, $\mathbf{F}_r$ is the reference fibre bundle and $\mathbf{F}_s$ is the source fibre bundle.

Table 5.1 shows the average time that `tsearchn` takes for the dataset breaking the displacement field into 1, 2 and 3 sections per dimension. Using 3 sections per dimension, i.e. 27 sections in total, achieves a speedup[1] of over 2.5. 27 sections is the physical limit for this dataset as anything higher results in overlaps that are larger than the sections.

This is a tradeoff between speed and memory efficiency. Sectioning the matrices this way has heavy memory costs. This is especially important as this task was done in parallel for 8 displacement fields at a time. The work station used for this had 24GB of RAM and an additional 24GB of virtual memory and this was used nearly to capacity during the calculations.

The total speedup achieved is 500, allowing the algorithm to run in two and half hours per brain image. The speedup due to downsampling is 100, to parallelization is 2 and

[1]Borrowing the term from parallel computing, *speedup* is used here to mean the time taken without the optimization approaches divided by the time taken with them. In other words the number of times faster the algorithm runs after the implementation of the optimizations.

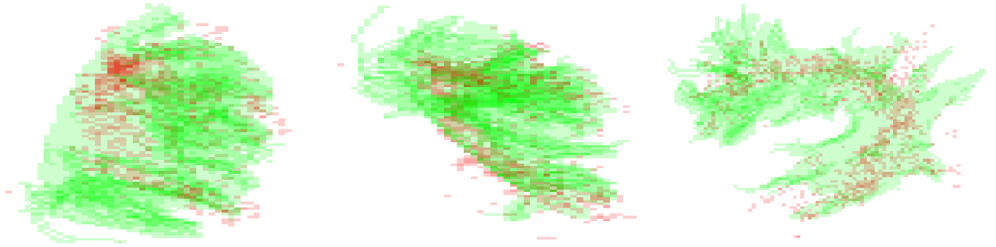

(a) $\mathbf{V}_r$ & $\mathbf{V}_o$, x-y-plane **(b)** $\mathbf{V}_r$ & $\mathbf{V}_o$, x-z-plane **(c)** $\mathbf{V}_r$ & $\mathbf{V}_o$, y-z-plane

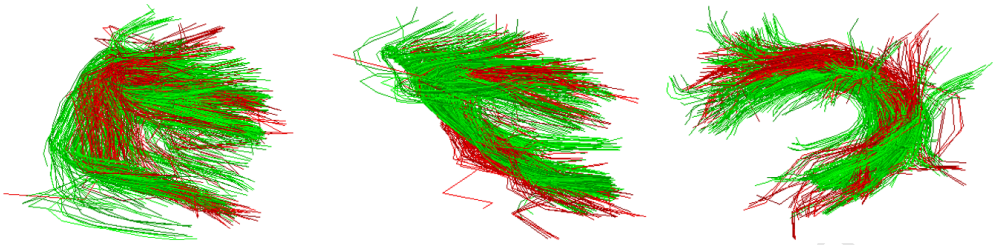

(d) $\mathbf{F}_r$ & $\mathbf{F}_o$, x-y-plane **(e)** $\mathbf{F}_r$ & $\mathbf{F}_o$, x-z-plane **(f)** $\mathbf{F}_r$ & $\mathbf{F}_o$, y-z-plane

Figure 5.12: Example results for fibre registration for Experiment 1. FA-based nonlinear fibre registration output image, brain 1, fibres and volumes (red) superimposed on reference image, brain 3, fibres and volumes (green).

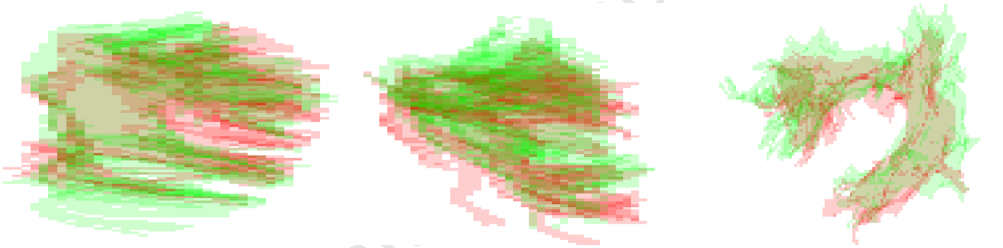

(a) $\mathbf{V}_r$ & $\mathbf{V}_o$, x-y-plane **(b)** $\mathbf{V}_r$ & $\mathbf{V}_o$, x-z-plane **(c)** $\mathbf{V}_r$ & $\mathbf{V}_o$, y-z-plane

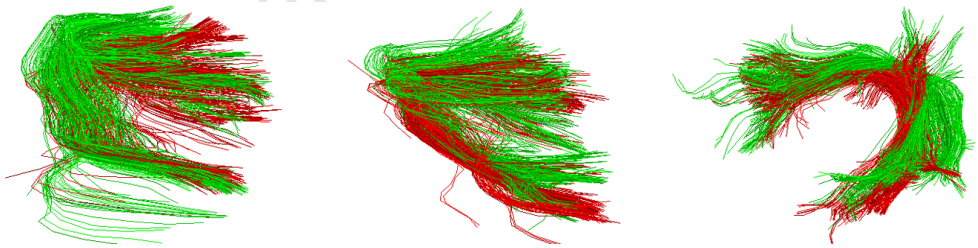

(d) $\mathbf{F}_r$ & $\mathbf{F}_o$, x-y-plane **(e)** $\mathbf{F}_r$ & $\mathbf{F}_o$, x-z-plane **(f)** $\mathbf{F}_r$ & $\mathbf{F}_o$, y-z-plane

Figure 5.13: Example results for fibre registration for Experiment 2. FA-based affine fibre registration output image, brain 1, fibres and volumes (red) superimposed on reference image, brain 9, fibres and volumes (green).

Table 5.1: Time decrease due to sectioning of the displacement field.

Total Number of Sections	Average time of `tsearchn`	Average Time per Bundle	Average Time per Brain Image
1	$5.5567s$	$147min$	$32hr$
8	$2.2376s$	$59min$	$13hr$
27	$1.9567s$	$52min$	$11hr$

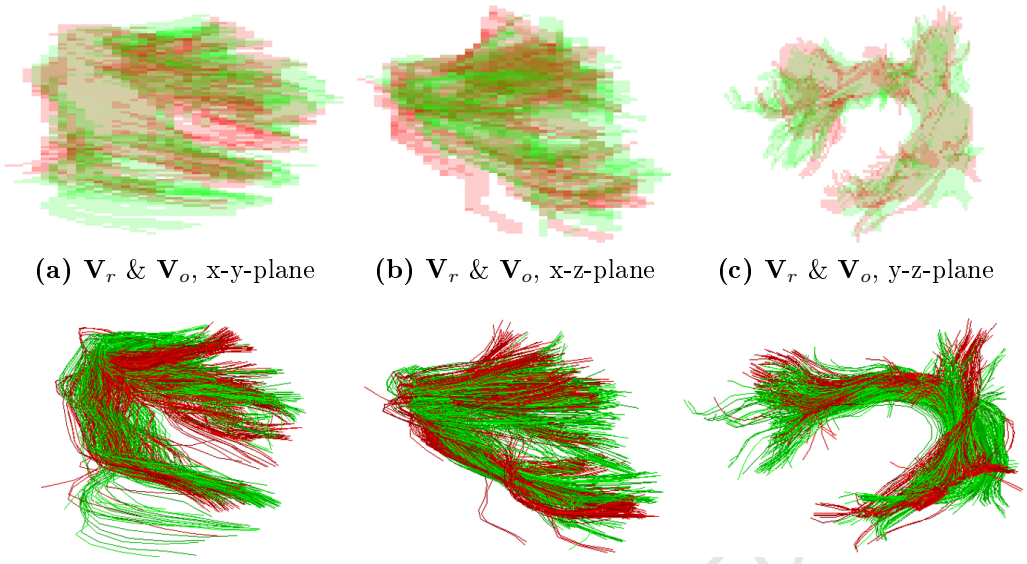

(a) $\mathbf{V}_r$ & $\mathbf{V}_o$, x-y-plane **(b)** $\mathbf{V}_r$ & $\mathbf{V}_o$, x-z-plane **(c)** $\mathbf{V}_r$ & $\mathbf{V}_o$, y-z-plane

(d) $\mathbf{F}_r$ & $\mathbf{F}_o$, x-y-plane **(e)** $\mathbf{F}_r$ & $\mathbf{F}_o$, x-z-plane **(f)** $\mathbf{F}_r$ & $\mathbf{F}_o$, y-z-plane

Figure 5.14: Example results for fibre registration for Experiment 3. Volume-based local affine fibre registration output image, brain 1, fibres and volumes (red) superimposed on reference image, brain 9, fibres and volumes (green).

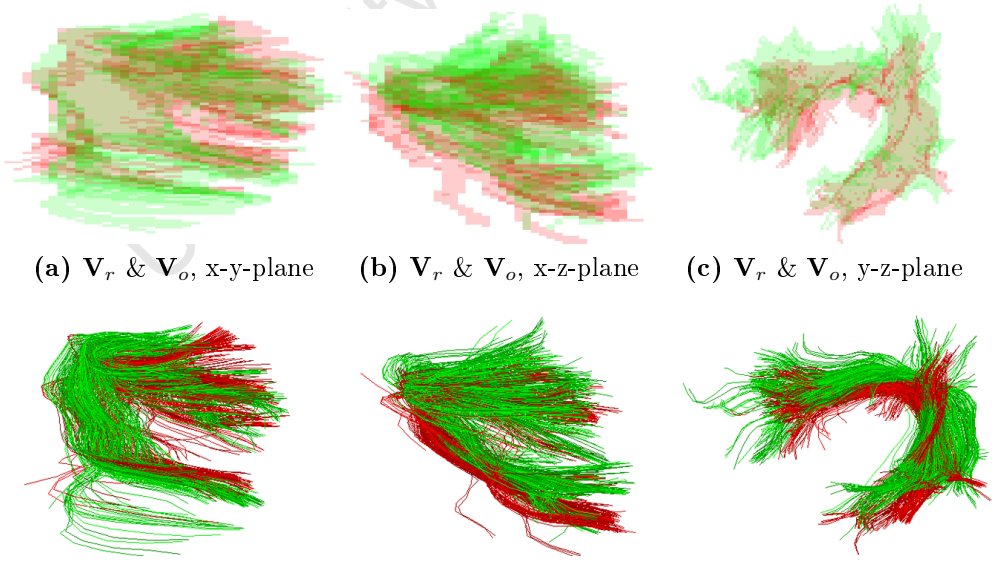

(a) $\mathbf{V}_r$ & $\mathbf{V}_o$, x-y-plane **(b)** $\mathbf{V}_r$ & $\mathbf{V}_o$, x-z-plane **(c)** $\mathbf{V}_r$ & $\mathbf{V}_o$, y-z-plane

(d) $\mathbf{F}_r$ & $\mathbf{F}_o$, x-y-plane **(e)** $\mathbf{F}_r$ & $\mathbf{F}_o$, x-z-plane **(f)** $\mathbf{F}_r$ & $\mathbf{F}_o$, y-z-plane

Figure 5.15: Example results for fibre registration for Experiment 4. Volume-based global affine fibre registration output image, brain 1, fibres and volumes (red) superimposed on reference image, brain 9, fibres and volumes (green).

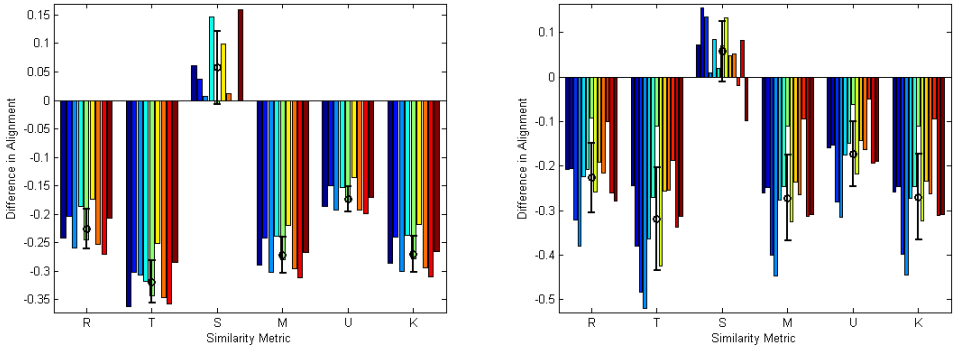

(a) (b)

Figure 5.16: Results of experiment 1. Improvement of bundle volume similarity after FA-based nonlinear fibre registrations. (a) shows the mean values for all bundles per brain and (b) shows the mean values for all brains per bundle.

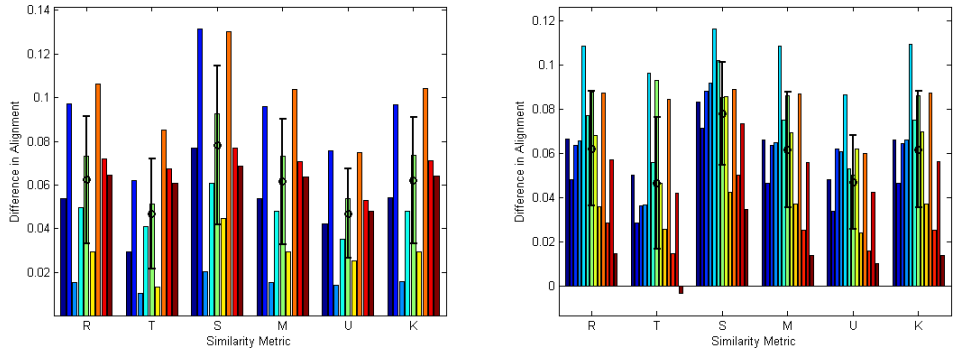

(a) (b)

Figure 5.17: Results of experiment 2. Improvement of bundle volume similarity after FA-based affine fibre registrations. (a) shows the mean values for all bundles per brain and (b) shows the mean values for all brains per bundle.

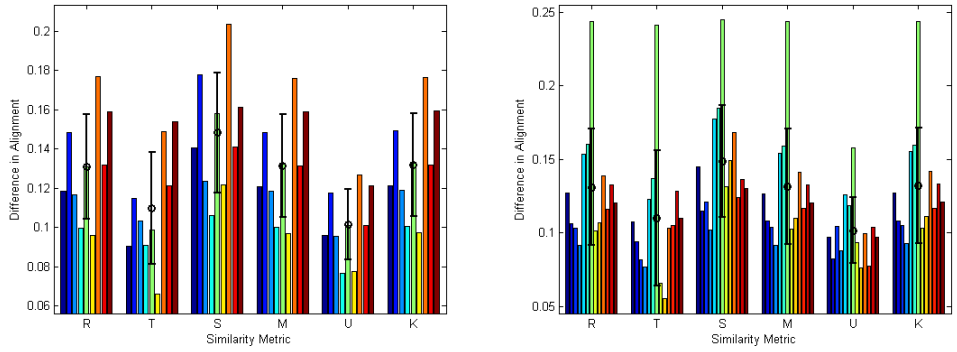

(a) (b)

Figure 5.18: Results of experiment 3. Improvement of bundle volume similarity after volume-based local affine fibre registrations. (a) shows the mean values for all bundles per brain and (b) shows the mean values for all brains per bundle.

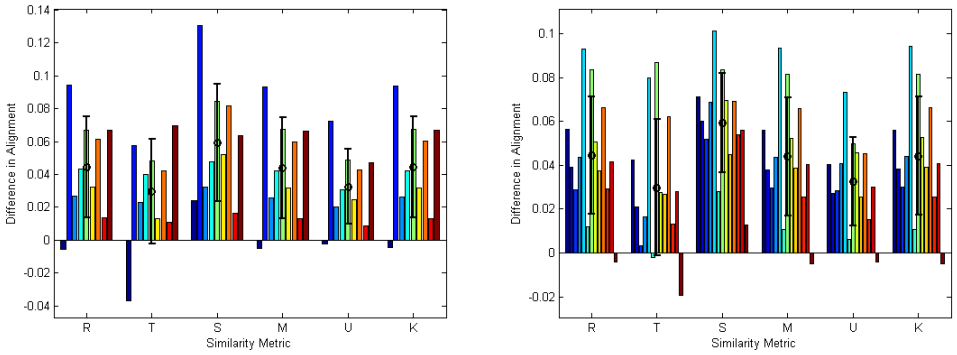

(a) (b)

Figure 5.19: Results of experiment 4. Improvement of bundle volume similarity after volume-based global affine fibre registrations. (a) shows the mean values for all bundles per brain and (b) shows the mean values for all brains per bundle.

(a) (b)

Figure 5.20: The effect of downsampling on a fibre bundle. (a) shows a bundle without downsampling and (b) shows a bundle downsampled to have one in ten fibres each with one in ten points per fibre.

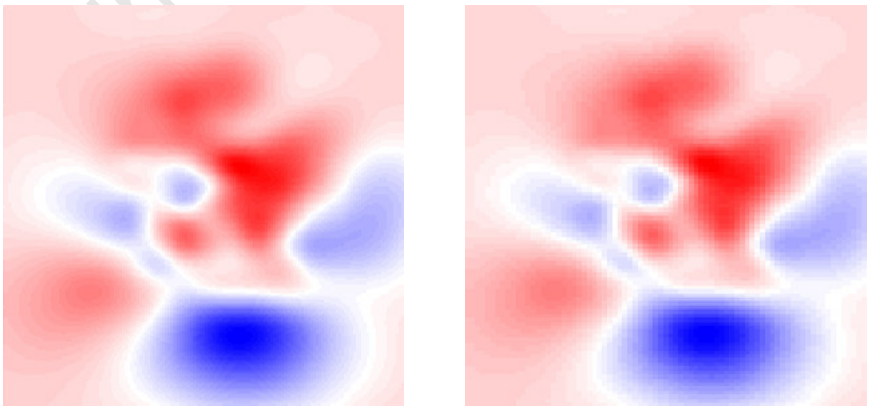

(a) (b)

Figure 5.21: The effect of downsampling on a displacement field. (a) shows a displacement field without downsampling and (b) shows a displacement field downsampled to include only every second vector in each direction. The images show the magnitude of the Z component of the displacement vector for an x-y-plane in the field.

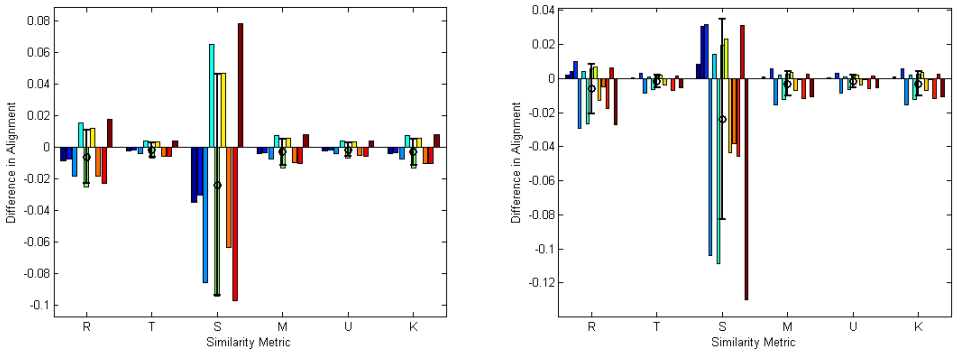

Figure 5.22: Results of fibre registrations for Experiment 1. Improvement of bundle volume similarity after FA-based nonlinear fibre registrations with the source fibres downsampled. (a) shows the mean values for all bundles per brain and (b) shows the mean values for all brains per bundle.

to sectioning is 2.5. These speedups are quoted as worst cases, in reality the speedup is higher.

5.3.2 Accounting for Downsampling

The results in Figure 5.16 suggest a large drop in the alignment of the fibre bundles after the nonlinear registration. The visualization in Figure 5.12 helps explain this puzzling result. The downsampling has made the volume encompassing the fibre points disconnected and small in comparison to the source and reference fibre images. The alignment metrics do not deal well with this vast difference in the amount of data in the images. Running the algorithm without downsampling would take months and is therefore not an option. In order to get a true reflection of whether or not the nonlinear registration has improved the alignment, the source fibres are also downsampled. The difference in alignment between the downsampled source fibres and the reference fibres with the alignment of the output fibres and the reference fibres is shown in Figure 5.22. These two alignments are now in the same order of magnitude allowing for a sensible comparison.

5.3.3 Test on Simulated Data

The FA-based nonlinear registration is the only experiment to have resulted in a lower alignment of output fibres with reference fibres than of source fibres with reference fibres. Downsampling the source fibres before comparing alignment brought the alignments to the same order of magnitude but the alignment of the output fibres with the reference fibres was still lower than that of the source fibres with the reference fibres, as shown in Tables A.4 and A.5 in the Appendix. To investigate why this is the case, the algorithm was run on simple, predictable, simulated data.

The source FA image was created by applying the affine transformation matrix

$$\mathbf{A} = \begin{pmatrix} 1 & 0 & 0 & -10 \\ 0 & 1 & 0 & -10 \\ 0 & 0 & 1 & -10 \\ 0 & 0 & 0 & 1 \end{pmatrix} \tag{5.1}$$

to the reference FA image. The transformation is a pure translation of the image by 10 voxels in each dimension. Thus the expected displacement field from the diffeomorphic registration would be a uniform vector field. The simulated transformation matrix was created by registering the source image to the reference image in MedInria using the parameters described in Section 4.4.1.

The simulated source fibres are straight lines arranged in a ramp formation spaced by 10 voxels in each of the the y and z directions. These are the red fibres in Figure 5.23. The blue fibres in the figure are the output fibres from the algorithm using the simulated transformation.

In general, the output fibres are displaced from the source fibres by approximately 10 voxels in each direction as expected. However, the fibres are no longer perfect straight lines. Visualizations of the displacement field illustrate why this is the case. Figure 5.24 shows the displacement field vectors of the midbrain planes. The fields are not uniform towards the edges of the brain or in the background of the image. This is due to the fact that the background in both the source and reference images is uniform (the voxels have a value of zero in the areas surrounding the brain). Translation is not observable in large uniform areas, as a shift of uniform voxels does not alter the image locally. This accounts for the kinks at the fringes of the output fibres, as they approach, and in some cases overlap, this uniform area. However, the fields do appear homogenous where the brain is in the image. It is difficult to observe subtle inhomogeneities in the field in this sort of visualization. Figure 5.25 shows the values of each of the X, Y and Z components of the vectors in the field separately. In these images, small fluctuations are visible throughout the image. This inhomogeneity in the displacement field is the cause of the distortions of the fibres.

This raises the question of why the displacement field is not homogenous in the areas of the image occupied by the brain. Crum *et al.* (2003) observe that if there is not a one-to-one correspondence between images, as is the case with the intra-subject images used in this study, the images will not have a unique spatial correspondence. Nonlinear registration often includes many indistinguishably good answers (Gee and Alexander, 2006). This assumes that the images are discrete, as the interpolation will allow the image to be transformed with a very high DOF. Perfect translation should result in a uniform displacement field, but as nonlinear registration has many indistinguishably good solutions based on the output image, the algorithms converge to produce the correct output image but not the expected displacement field. Interpolation allows this inhomogeneous field to result in an output image that appears to have undergone a pure translation. The continuous fibre images cannot be interpolated in the same way and become distorted as a result. Thus it is reasonable to conclude that a transformation derived from discrete images through a high DOF process with multiple optima cannot be reapplied to the thin, continuous fibres. Thus the application of a diffeomorphic demons based registration in this manner is not appropriate for fibre data.

5.4 Further Investigations into Experiment 3

5.4.1 Comparison of Binary Volumes and PDFs

Table 5.2 shows that the binary volume of a fibre bundle can be computed nearly 70000 times faster than the fast algorithm for finding the PDF. Registration of the PDFs for the corticofugal bundle show that not only does the binary volume produce a satisfactory

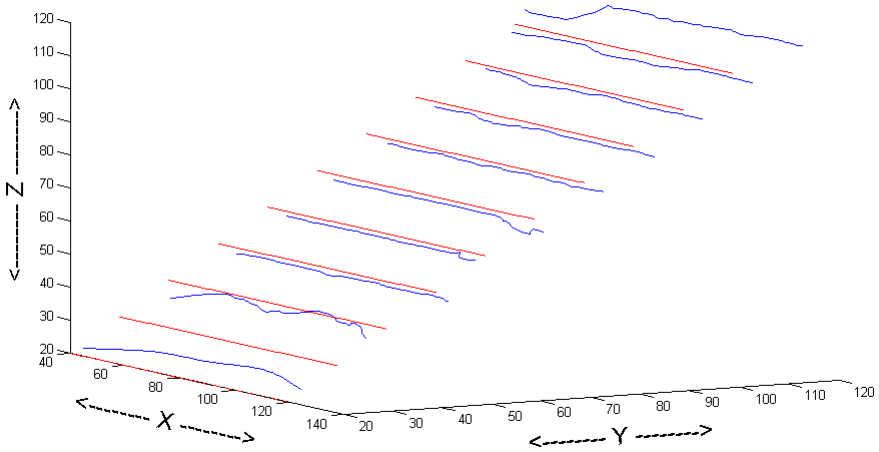

(a) 3D view

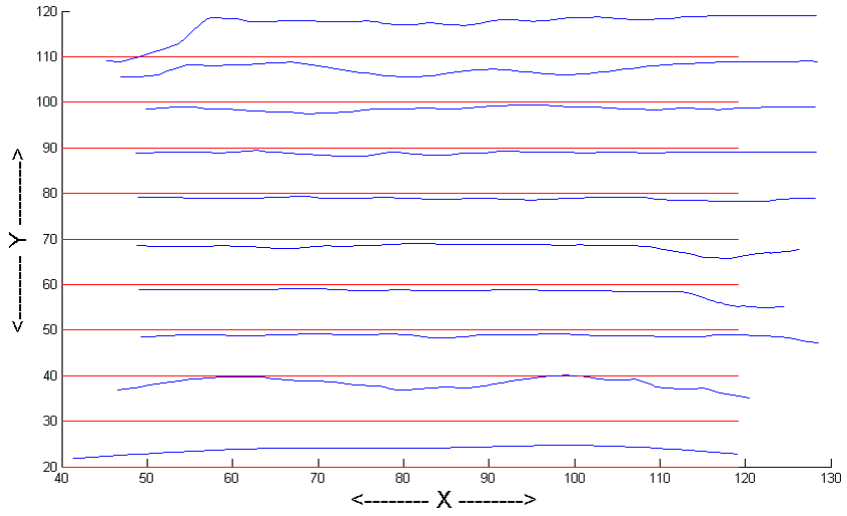

(b) x-y view

Figure 5.23: Results of FA-based nonlinear registration on simulated data. Simulated source fibres are shown in red and the output fibres in blue.

Table 5.2: Time taken to convert a fibre bundle to a volume.

Method	Average Time per Bundle	Speedup
PDF according to Equation 3.1	$32hr$	1
PDF according to Equation 4.7	$4hr$	8
Binary Volume	$0.21s$	550000

alignment in a greatly reduced time, but actually results in superior registrations. The average correlation coefficients for the experiments are $R_{\mathbf{SR}} = 0.5256$, $R_{\mathbf{O}_{PDF}\mathbf{R}} = 0.5309$ and $R_{\mathbf{O}_{Binary}\mathbf{R}} = 0.6042$; where $R_{\mathbf{SR}}$ is the correlation between the source image, $\mathbf{S}$, and the reference image, $\mathbf{R}$, as defined by equation 4.11, $\mathbf{O}_{PDF}$ is the output of fibre registration using PDF volumes for the base registration and $\mathbf{O}_{Binary}$ is the output of fibre registration using binary volumes for the base registration. Figure 5.26 shows this

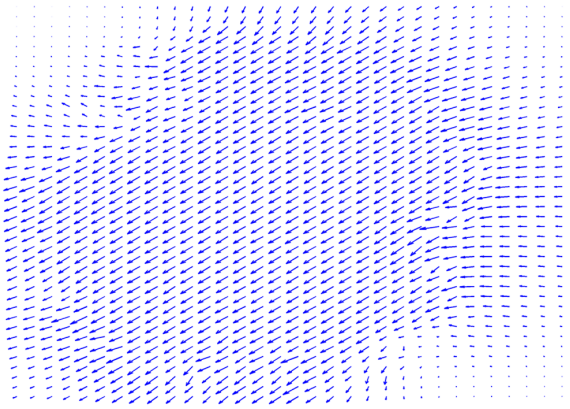

(a) Cross section

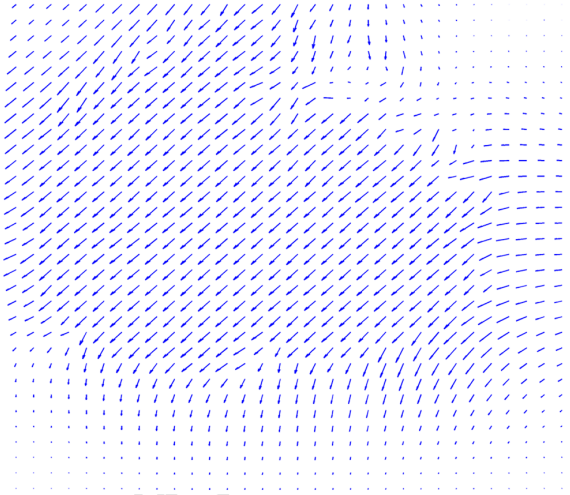

(b) Coronal section

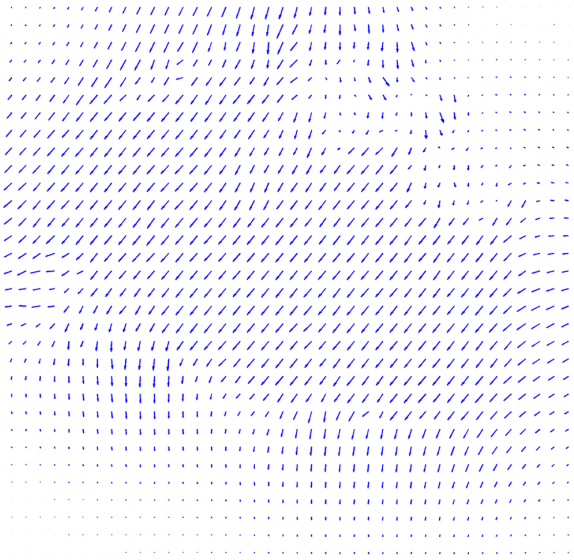

(c) Sagittal section

Figure 5.24: Displacement field vectors from simulated transformation. Only one in every five vectors is shown in each direction.

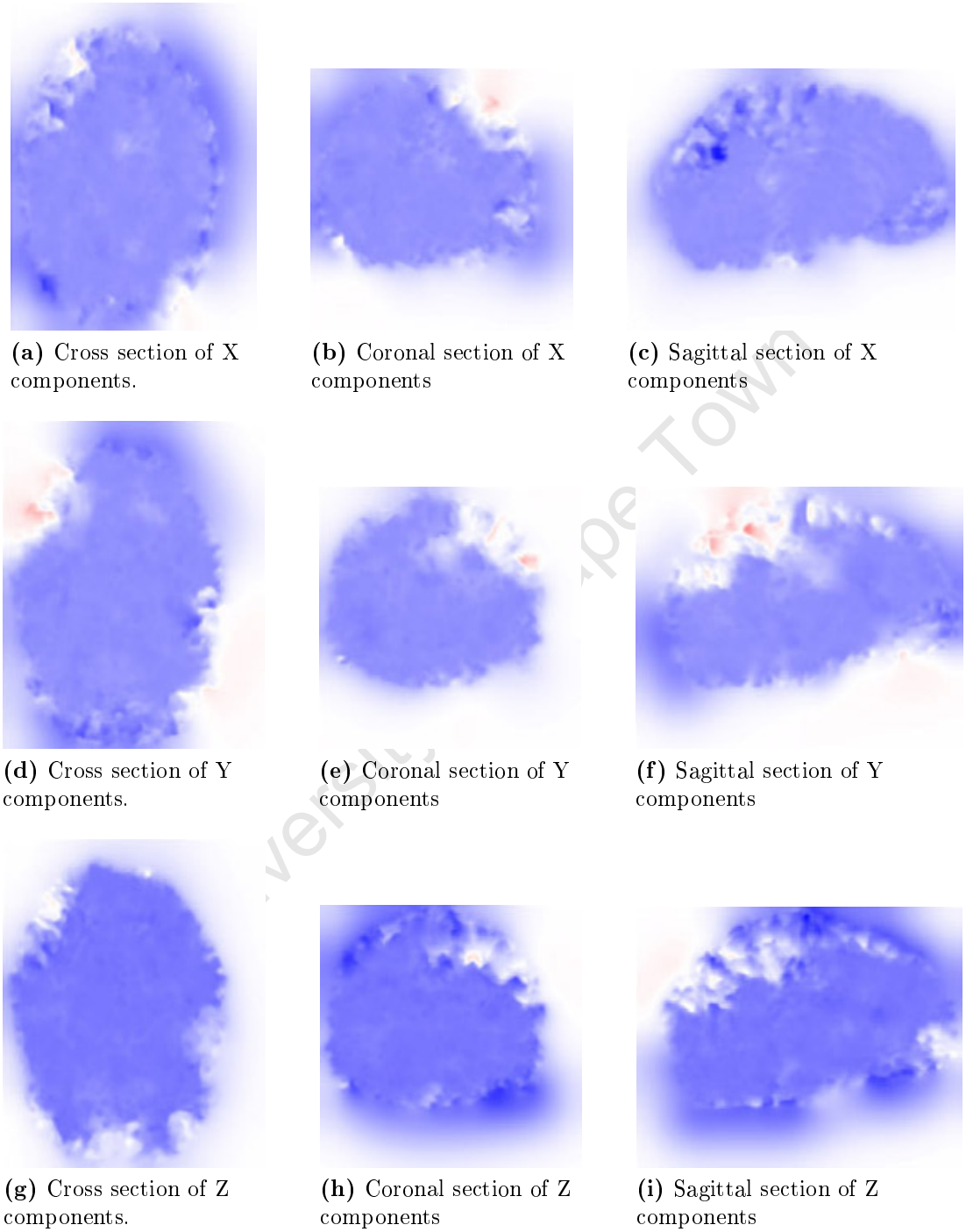

(a) Cross section of X components.

(b) Coronal section of X components

(c) Sagittal section of X components

(d) Cross section of Y components.

(e) Coronal section of Y components

(f) Sagittal section of Y components

(g) Cross section of Z components.

(h) Coronal section of Z components

(i) Sagittal section of Z components

Figure 5.25: Displacement field components from simulated transformation.

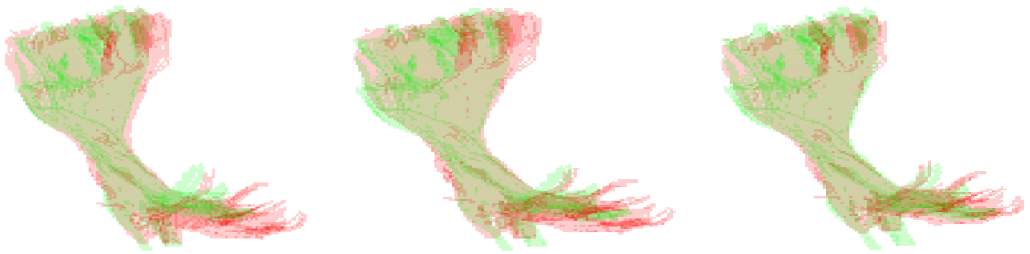

(a) Source **(b)** PDF **(c)** Binary

Figure 5.26: Comparison of output volumes from fibre registration using PDF and binary volumes as the base registration. The green volumes are from the reference fibres and the red volumes are from (a) the source fibres, (b) the output fibre from the registration of PDFs and (c) the output fibres from the registration of binary volumes. Brain 9 is used as the reference and brain 1 as the source and output.

Table 5.3: Results of a t-test testing the hypothesis that the mean alignment from volume-based local affine fibre registration is higher than the mean alignment from volume-based local affine base registration. Variance is assumed to be unequal.

	Cross Correlation	Target Overlap	Source Overlap	Mutual Overlap	Union Overlap	Cohen's Kappa
p-value	0.2446	0.1801	0.3802	0.2537	0.1911	0.2539
t-statistic	−0.7080	−0.9448	−0.3102	−0.6781	−0.8981	−0.6776
base SD	0.0291	3.9041	3.2791	2.8580	1.9694	0.0286
fibre SD	0.0268	2.8385	3.0437	2.6153	1.7817	0.0262
DOF	15.8941	14.6106	15.9120	15.8757	15.8422	15.8800

visually. The results from the PDF based registration may be improved by tweaking the parameters of the Gaussian kernel, but it is unlikely that this will surpass the binary volume results and is still far slower.

Even for binary volumes, each bundle registration takes $3313s$ on average, which is impractical as it would take four and a half days to complete all the registrations. Downsampling the binary volumes before registration as described in Section 4.6.2, decreases the average registration time to $61s$, making the time for all the registrations under two hours.

5.4.2 Test of Significance

The volume-based local affine registration, in Experiment 3, yields the peculiar result that the fibre registration outperforms the base registration. This unexpected result is most easily observed by comparing Table A.10 with Table A.12. As the fibre registration is based on the base registration, it should follow that the fibre alignments are slightly lower than the base alignments.

A one tailed t-test was performed on the data in Table A.10 and Table A.12 to ascertain if the increased mean of the alignment is statistically significant. The variances were assumed to be unequal. Table 5.3 shows the results of this test. The high p-values indicate that the differences between base and fibre registrations is not significant, for all metrics. A similar result was obtained when assuming equal variance.

Table 5.4: Mean of improvement of *fibre* registrations per method.

Experiment Number	Cross Correlation	Target Overlap	Source Overlap	Mutual Overlap	Union Overlap	Cohen's Kappa
1	−0.2262	−0.32	0.06	−0.27	−0.17	−0.2698
1 with source fibres downsampled	−0.0061	−0.00	−0.02	−0.00	−0.00	−0.0031
2	0.0623	0.05	0.08	0.06	0.05	0.0619
3	0.1309	0.11	0.15	0.13	0.10	0.1321
4	0.0445	0.03	0.06	0.04	0.03	0.0442

Table 5.5: Mean alignment per method of output images with reference image after *fibre* registration.

Experiment Number	Cross Correlation	Target Overlap	Source Overlap	Mutual Overlap	Union Overlap	Cohen's Kappa
1	0.0989	0.03	0.38	0.05	0.03	0.0506
2	0.3976	0.39	0.42	0.40	0.26	0.3941
3	0.4661	0.45	0.49	0.47	0.31	0.4643
4	0.3797	0.37	0.40	0.38	0.24	0.3764

5.5 Results Summary

This section presents tables and figures that summarize and compare the numerous results presented in this chapter. Table 5.4 shows the results of the improvement each of the methods has had on the alignment of the fibres after registration. Table 5.5 presents the alignments after registration. Figure 5.27 shows the values presented in Table 5.4 in a graphical form. Finally, Figure 5.28 shows for the source images and for the output images from each experiment, the arcuate fasciculus from each of the 10 brain images superimposed on each other. This figure illustrates the success of registration, as well aligned bundles will overlap, while poorly aligned bundles will spread more broadly across image with the coloured bundles separated from one another. The colours in Figure 5.28a and Figure 5.28b are separated as the bundles are spread out, indicating poor alignment, whereas Figure 5.28d shows the best registration as the bundles are less spread out indicating a higher degree of alignment across the bundles.

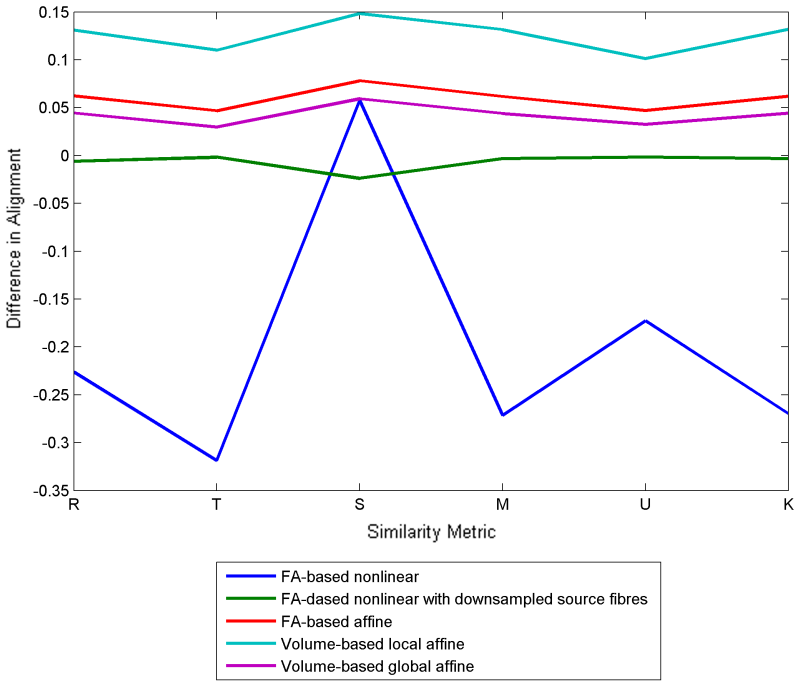

Figure 5.27: Mean of improvement of *fibre* registrations per method.

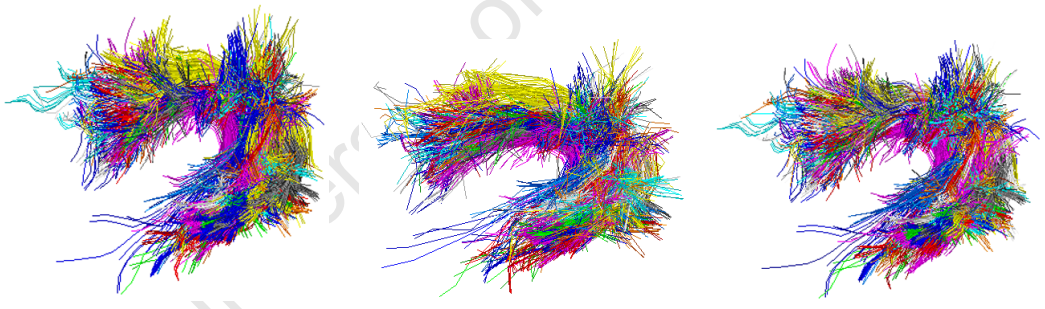

(a) Source Fibres

(b) FA-based nonlinear registered fibres

(c) FA-based affine registered fibres

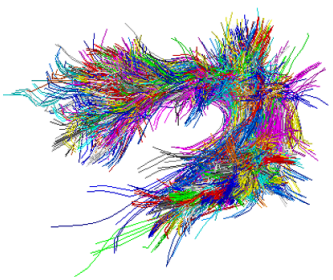

(d) Volume-based local affine registered fibres

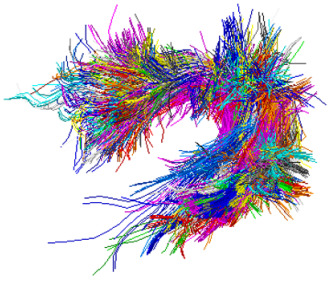

(e) Volume-based global affine registered fibres

Figure 5.28: The arcuate fasciculi for all 10 brain images superimposed over each other for the source fibres and the output fibres of each of the four methods.

Chapter 6

Discussion and Conclusion

6.1 Discussion

The experiments show that the direct registration of fibre images produces alignment of individual fibre bundles. The tracked fibres will not suffer from the accumulative error introduced by the imperfect spatial realignment and voxel re-orientation of DTI registration as the fibre tracking is performed prior to the registration.

Table 5.4 shows that the local affine registrations substantially outperform the two global affine methods (the FA-based affine and the volume-based global affine). This is shown visually in Figure 5.28, where Figure 5.28d is clearly the image with all 10 bundles most closely aligned. Variability in the size, shape and orientation of cortical structures in primates is particularly pronounced (Bjaalie, 2002). This ratifies the observation that a better alignment can be found by aligning corresponding structures separately rather than aligning the entire brain image globally. The FA-based global affine technique slightly outperformed the volume-based global affine technique. The FA-based nonlinear registration is the only method to have conclusively failed. Section 5.3.3 presented the results of running the algorithm on simple simulated data in an attempt to discover the reason for this. The high DOF of the demons based registration algorithm resulted in distortions of the fibres. The failure of the algorithm is attributed to these distortions. Such a high DOF transformation is thus not suitable for fibre data.

While the methods proposed by Ziyan *et al.* (2007) formed the basis for the experiments presented here, direct comparison with their results is not possible as their goal was DTI registration and they do not show results of the tractographic registration section of their work.

The six metrics for measuring the alignment of the fibre bundles generally agree. The source overlap seems to be the least consistent metric, as can be seen in Figure 5.27, and is thus not recommended for future use. The values for Cohen's Kappa all fall in the *moderate agreement* category as defined by Landis and Koch (1977). Cohen's Kappa is usually used as a measure of inter-rater agreement and has been used to measure alignment of fibre bundles for intra-subject, rigid transformations.

The use of binary volumes as a base registration over PDFs in the local-affine registration proved not only to be faster but also to produce registrations of a higher quality. It takes almost 70000 times longer to calculate the PDF volume of a fibre bundle as it does to find the equivalent binary volume.

6.1.1 Potential Sources of Error

An assumption in all four experiments is that there is one brain image, selected as a reference image, which is representative of the entire set. This is not necessarily the case (Klein *et al.*, 2009).

Furthermore, each experiment is based on manually segmented fibre data. The segmentations are treated as exhibiting perfect correspondence and homology. This is an unobtainable assumption no matter how skilled the segmenter. Error in the segmentation process includes not only the inherent error expected from a human interactive process, but also error from the flaws in the assumption of perfect correspondence and homology amongst humans, and will have been propagated throughout this study.

6.2 Conclusion

DTI and tractography have produced new images that are allowing the intricate structure of the white matter fibres in the brain to be studied for the first time. For inter-subject studies of population morphology or intra-subject studies exploring the relationship between cortical structure and function, precise localization across images is essential. This is achieved though image registration. Registration of DTI images is complicated by the fact that each voxel needs to be re-oriented aside from the spatial reorganization of the voxels. This process is still an open problem. Tractography is an error prone process which is not robust to changes in the DTI image. It is reasonable to assume that tractography prior to the registration of the DTI image will produce more accurate results than tracking fibres after registration. The problem of registering tractographic images has had very little attention in the literature. This project explored four methods of registering fibre images directly. The first method used a diffeomorphic demons registration on the FA images to produce a displacement field. This transformation was applied to the fibre images by interpolating the displacement field using Delaunay triangulation. The method was not successful as the high DOF of the base registration results in distorted fibres. The second method found a global affine transformation using the FA images. This method increased the correlation of the fibre tracts from 0.34 to 0.39. The third method found local affine transformations for each bundle by converting the bundles to binary volumes. The binary volumes are faster to calculate and produce superior results to PDFs as used in the literature. This method is the most successful improving the correlation by 0.13, more than twice the improvement of the next best method. The final method converted the bundles to a binary volume and found a global affine transformation for these. This method was successful but slightly less so than the FA-based global affine method. The local affine method is superior due to the high variability in the cortical structures of humans, which a global affine transformation cannot account for. The polyaffine approach by Ziyan *et al.* (2007) is an excellent compromise between the very low DOF global affine transformations and the very high DOF transformation from a diffeomorphic demons based registration.

6.3 Recommendations

Direct registration of fibre images does not suffer from the additional error introduced by registering the DTI images which is accumulated in the fibre tracking process. This work has shown that direct fibre registration is a suitable method to align fibre tracts. It

should therefore be more thoroughly compared with the registration of DTI image prior to tractography, which is currently the method of choice in the literature.

As the binary volumes are faster to calculate and produce better alignments than the PDF volumes, the polyaffine transformation described by Ziyan *et al.* (2007) should be re-examined using binary volumes as the basis for registration.

Aside from comparing these methods with the DTI registration methods, there has been no comparison of the fibre tracking methods presented by Leemans *et al.* (2006), Ziyan *et al.* (2007), Mayer and Greenspan (2008) or Shadmi *et al.* (2010). A comparison on the scale of the work by Klein *et al.* (2009) is essential for a new field such as this comparing and contrasting the many DTI registration methods with the direct fibre registration methods that are beginning to emerge.

Alternatives to using the FA images as the scalar base images can be explored. One such alternative could be the b0 image of the DWI data.

The use of manually segmented data provides a method of validating the success of registration on the internal structures of the brain images. However, manual segmentation is a flawed and laborious process. The author recommends that future works make use of automated segmentation such as the methods employed by O'Donnell and Westin (2007).

At the time of completion of this work, a new publication describes methods of direct fibre registration. Durrleman *et al.* (2011) uses a metric on currents to perform the registration. This eliminates the need for a correspondence between points or individual fibres which makes the method robust. The reader is referred to Durrleman *et al.* (2011) for a detailed explanation of this novel and promising algorithm.

References

Alexander, D., Gee, J. and Bajcsy, R. (1999). Strategies for data reorientation during non-rigid warps of diffusion tensor images. In: *Medical Image Computing and Computer-Assisted Intervention–MICCAI 99*, pp. 463–472. Springer.

Alexander, D., Gee, J. and Bajcsy, R. (2002*a*). Elastic matching of diffusion tensor MRIs. In: *Computer Vision and Pattern Recognition, 1999. IEEE Computer Society Conference on.*, vol. 1. IEEE. ISBN 0769501494.
Available at: http://ieeexplore.ieee.org/xpls/abs_all.jsp?arnumber=786946

Alexander, D., Pierpaoli, C., Basser, P. and Gee, J. (2002*b*). Spatial transformations of diffusion tensor magnetic resonance images. *IEEE Transactions on Medical Imaging*, vol. 20, no. 11, pp. 1131–1139. ISSN 0278-0062.
Available at: http://ieeexplore.ieee.org/xpls/abs_all.jsp?arnumber=963816

Anderson, A.W. (2005 November). Measurement of fiber orientation distributions using high angular resolution diffusion imaging. *Magnetic resonance in medicine : official journal of the Society of Magnetic Resonance in Medicine / Society of Magnetic Resonance in Medicine*, vol. 54, no. 5, pp. 1194–206. ISSN 0740-3194.
Available at: http://www.ncbi.nlm.nih.gov/pubmed/16161109

Andersson, J., Jenkinson, M. and Smith, S. (2007 June). Non-linear registration, aka Spatial normalisation. *FMRIB Analysis Group Technical Reports: TR07JA02.*
Available at: http://scholar.google.com/scholar?hl=en&btnG=Search&q=intitle:Non-linear+registration+aka+Spatial+normalisation#0

Andrew, E. (2009). Nuclear magnetic resonance. *Nuclear Magnetic Resonance. Cambridge Monographs on Physics.*, vol. 1.
Available at: http://adsabs.harvard.edu/abs/2009nmr..book.....A

Anwander, A., Tittgemeyer, M., Von Cramon, D.Y., Friederici, A.D. and Knösche, T.R. (2007 April). Connectivity-Based Parcellation of Broca's Area. *Cerebral cortex (New York, N.Y. : 1991)*, vol. 17, no. 4, pp. 816–25. ISSN 1047-3211.
Available at: http://www.ncbi.nlm.nih.gov/pubmed/16707738

Ardekani, B.a., Guckemus, S., Bachman, A., Hoptman, M.J., Wojtaszek, M. and Nierenberg, J. (2005 March). Quantitative comparison of algorithms for inter-subject registration of 3D volumetric brain MRI scans. *Journal of neuroscience methods*, vol. 142, no. 1, pp. 67–76. ISSN 0165-0270.
Available at: http://www.ncbi.nlm.nih.gov/pubmed/15652618

Arsigny, V., Commowick, O., Ayache, N. and Pennec, X. (2009 January). A Fast and Log-Euclidean Polyaffine Framework for Locally Linear Registration. *Journal of Mathematical Imaging and Vision*, vol. 33, no. 2, pp. 222–238. ISSN 0924-9907.
Available at: http://www.springerlink.com/index/10.1007/s10851-008-0135-9

Arsigny, V., Pennec, X. and Ayache, N. (2005). Polyrigid and polyaffine transformations: a novel geometrical tool to deal with non-rigid deformations-application to the registration of histological slices. *Medical Image Analysis*, vol. 9, no. 6, pp. 507–523. ISSN 1361-8415.
Available at: http://linkinghub.elsevier.com/retrieve/pii/S1361841505000289

Ashburner, J. and Friston, K. (1999). Nonlinear spatial normalization using basis functions. *Human Brain Mapping*, vol. 7, no. 4, pp. 254–266. ISSN 1097-0193.
Available at: http://www3.interscience.wiley.com/journal/62000342/abstract

Barber, C.B., Dobkin, D.P. and Huhdanpaa, H. (1996 December). The quickhull algorithm for convex hulls. *ACM Transactions on Mathematical Software*, vol. 22, no. 4, pp. 469–483. ISSN 00983500.
Available at: http://portal.acm.org/citation.cfm?doid=235815.235821

Basser, P., Pajevic, S., Pierpaoli, C., Duda, J. and Aldroubi, A. (2000). In vivo fiber tractography using DT-MRI data. *Magnetic Resonance in Medicine*, vol. 44, no. 4, pp. 625–632. ISSN 1522-2594.
Available at: http://www3.interscience.wiley.com/journal/73503085/abstract

Basser, P. and Pierpaoli, C. (1996). Microstructural and physiological features of tissues elucidated by quantitative-diffusion-tensor MRI. *Journal of Magnetic Resonance-Series B*, vol. 111, no. 3, pp. 209–219. ISSN 1064-1866.
Available at: http://scholar.google.com/scholar?hl=en&btnG=Search&q=intitle:Microstructural+and+Physiological+Features+of+Tissues+Elucidated+by+Quantitative-Diffusion-Tensor+MRI#0

Basser, P.J., Mattiello, J. and LeBihan, D. (1994). Estimation of the effective self-diffusion tensor from the NMR spin echo. *Journal of magnetic resonance. Series B*, vol. 103, no. 3, pp. 247–254.
Available at: http://noodle.med.yale.edu/~{}mjack/papers/basser-1994.pdf

Beaulieu, C. (2002). The basis of anisotropic water diffusion in the nervous system - a technical review. *NMR in biomedicine*, vol. 15, no. 7-8, pp. 435–55. ISSN 0952-3480.
Available at: http://www.ncbi.nlm.nih.gov/pubmed/12489094

Bernstein, M., King, K. and Zhou, X. (2004). *Handbook of MRI pulse sequences*. Academic Pr. ISBN 0120928612.

Bjaalie, J. (2002). Localization in the brain: new solutions emerging. *Nature reviews neuroscience*, vol. 3, no. 4, pp. 322–325. ISSN 1471-003X.
Available at: http://www.nature.com/nrn/journal/v3/n4/abs/nrn790.html

Black, K., Videen, T. and Perlmutter, J. (1996). A metric for testing the accuracy of cross-modality image registration: validation and application. *Journal of computer assisted tomography*, vol. 20, no. 5. ISSN 0363-8715.

Brett, M., Johnsrude, I.S. and Owen, A.M. (2002 March). The problem of functional localization in the human brain. *Nature reviews. Neuroscience*, vol. 3, no. 3, pp. 243–9. ISSN 1471-003X.
Available at: http://www.ncbi.nlm.nih.gov/pubmed/11994756

Chiang, M., Leow, A., Klunder, A., Dutton, R., Barysheva, M., Rose, S., McMahon, K., De Zubicaray, G., Toga, A. and Thompson, P. (2008). Fluid registration of diffusion tensor images using information theory. *Medical Imaging, IEEE Transactions on*, vol. 27, no. 4, pp. 442–456. ISSN 0278-0062.
Available at: http://ieeexplore.ieee.org/xpls/abs_all.jsp?arnumber=4359066

Ciccarelli, O., Catani, M., Johansen-Berg, H., Clark, C. and Thompson, A. (2008 August). Diffusion-based tractography in neurological disorders: concepts, applications, and future developments. *Lancet neurology*, vol. 7, no. 8, pp. 715–727. ISSN 1474-4422.
Available at: http://www.ncbi.nlm.nih.gov/pubmed/18635020

Collins, D., Neelin, P., Peters, T. and Evans, A. (1994). Automatic 3D intersubject registration of MR volumetric data in standardized Talairach space. *Journal of computer assisted tomography*, vol. 18, no. 2, p. 192. ISSN 0363-8715.

Crick, F. and Jones, E. (1993). Backwardness of human neuroanatomy. *Nature*, vol. 361, no. 6408, pp. 109–110. ISSN 0028-0836.
Available at: http://adsabs.harvard.edu/abs/1993Natur.361..109C

Crum, W., Griffin, L., Hill, D. and Hawkes, D. (2003 November). Zen and the art of medical image registration: correspondence, homology, and quality. *NeuroImage*, vol. 20, no. 3, pp. 1425–1437. ISSN 10538119.
Available at: http://linkinghub.elsevier.com/retrieve/pii/S1053811903004154

Crum, W.R. (2004 December). Non-rigid image registration: theory and practice. *British Journal of Radiology*, vol. 77, no. Special Issue 2, pp. S140–S153. ISSN 0007-1285.
Available at: http://bjr.birjournals.org/cgi/doi/10.1259/bjr/25329214

Danielian, L., Iwata, N., Thomasson, D. and Floeter, M. (2010). Reliability of fiber tracking measurements in diffusion tensor imaging for longitudinal study. *NeuroImage*, vol. 49, no. 2, pp. 1572–1580. ISSN 1053-8119.
Available at: http://linkinghub.elsevier.com/retrieve/pii/S1053811909009732

Dovey, D. (1995). Vector plots for irregular grids. In: *Proceedings of the 6th conference on Visualization'95*, p. 248. IEEE Computer Society. ISBN 0818671874.
Available at: http://portal.acm.org/citation.cfm?id=833878

Durrleman, D., Fillard, P., Pennec, X., Trouvé, A. and Ayache, N. (2011). Registration, atlas estimation and variability analysis of white matter fiber bundles modeled as currents. *NeuroImage*, vol. 55, no. 3, pp. 1073 – 1090. ISSN 1053-8119.
Available at: http://www.sciencedirect.com/science/article/pii/S105381191001534X

Evans, A., Collins, D. and Milner, B. (1992). An MRI-based stereotactic atlas from 250 young normal subjects. In: *Soc. neurosci. abstr*, vol. 18, p. 408.

Fillard, P., Souplet, J. and Toussaint, N. (2007). *Medical image navigation and research tool by INRIA (MedINRIA) tutorial v2.0*. Asclepios.
Available at: http://www-sop.inria.fr/asclepios/software/MedINRIA/doc/onlinehelp/ma-nual.html

Gee, J. and Alexander, D. (2006 January). Diffusion-tensor image registration. *Visualization and Processing of Tensor Fields*, vol. 11, no. 2, pp. 327–342.
Available at: http://www.springerlink.com/index/x714w846857p46r1.pdf

Geng, X., Ross, T.J., Zhan, W., Gu, H., Chao, Y.-P., Lin, C.-P., Christensen, G.E., Schuff, N. and Yang, Y. (2009 January). Diffusion MRI registration using orientation distribution functions. *Information processing in medical imaging : proceedings of the ... conference*, vol. 21, pp. 626–37. ISSN 1011-2499.
Available at: http://www.ncbi.nlm.nih.gov/pubmed/19694299

Hajnal, J., Hawkes, D. and Hill, D. (2001). *Medical image registration*. CRC. ISBN 0849300649.

Hashemi, R., Bradley, W. and Lisanti, C. (2010). *MRI: the basics*. Lippincott Williams & Wilkins. ISBN 1608311155.

Heiervang, E., Behrens, T.E.J., Mackay, C.E., Robson, M.D. and Johansen-Berg, H. (2006 November). Between session reproducibility and between subject variability of diffusion MR and tractography measures. *NeuroImage*, vol. 33, no. 3, pp. 867–77. ISSN 1053-8119.
Available at: http://www.ncbi.nlm.nih.gov/pubmed/17000119

Hill, D.L., Batchelor, P.G., Holden, M. and Hawkes, D.J. (2001 March). Medical image registration. *Physics in medicine and biology*, vol. 46, no. 3, pp. R1–45. ISSN 0031-9155.
Available at: http://www.ncbi.nlm.nih.gov/pubmed/11277237

Hodaie, M., Quan, J. and Chen, D.Q. (2010 April). In vivo visualization of cranial nerve pathways in humans using diffusion-based tractography. *Neurosurgery*, vol. 66, no. 4, pp. 788–95; discussion 795–6. ISSN 1524-4040.
Available at: http://www.ncbi.nlm.nih.gov/pubmed/20305498

Holden, M., Hill, D.L., Denton, E.R., Jarosz, J.M., Cox, T.C., Rohlfing, T., Goodey, J. and Hawkes, D.J. (2000 February). Voxel similarity measures for 3-D serial MR brain image registration. *IEEE transactions on medical imaging*, vol. 19, no. 2, pp. 94–102. ISSN 0278-0062.
Available at: http://www.ncbi.nlm.nih.gov/pubmed/10784281

Ingalhalikar, M., Yang, J., Davatzikos, C. and Verma, R. (2010 May). DTI-DROID: Diffusion tensor imaging-deformable registration using orientation and intensity descriptors. *International Journal of Imaging Systems and Technology*, vol. 20, no. 2, pp. 99–107. ISSN 08999457.
Available at: http://doi.wiley.com/10.1002/ima.20232

Jacobs, J.M. and Love, S. (1985 December). Qualitative and quantitative morphology of human sural nerve at different ages. *Brain : a journal of neurology*, vol. 108, no. 4, pp. 897–924. ISSN 0006-8950.
Available at: http://www.ncbi.nlm.nih.gov/pubmed/4075078

Jellison, B.J., Field, A.S., Medow, J., Lazar, M., Salamat, M.S. and Alexander, A.L. (2004 March). Diffusion tensor imaging of cerebral white matter: a pictorial review of physics, fiber tract anatomy, and tumor imaging patterns. *AJNR. American journal of neuroradiology*, vol. 25, no. 3, pp. 356–69. ISSN 0195-6108.
Available at: http://www.ncbi.nlm.nih.gov/pubmed/15037456

Jenkinson, M. (ND). Coordinate transformation conventions for spatial registration.
Available at: http://users.fmrib.ox.ac.uk/~mark/files/coordtransforms.pdf

Jenkinson, M., Bannister, P., Brady, M. and Smith, S. (2002 October). Improved Optimization for the Robust and Accurate Linear Registration and Motion Correction of Brain Images. *NeuroImage*, vol. 17, no. 2, pp. 825–841. ISSN 10538119.
Available at: http://linkinghub.elsevier.com/retrieve/pii/S1053811902911328

Jenkinson, M. and Smith, S. (2001 June). A global optimisation method for robust affine registration of brain images. *Medical image analysis*, vol. 5, no. 2, pp. 143–56. ISSN 1361-8415.
Available at: http://www.ncbi.nlm.nih.gov/pubmed/11516708

Jia, H., Yap, P., Wu, G., Wang, Q. and Shen, D. (2011 January). Intermediate Templates Guided Groupwise Registration of Diffusion Tensor Images. *NeuroImage*, vol. 54, no. 2, pp. 928–939. ISSN 1053-8119.
Available at: http://linkinghub.elsevier.com/retrieve/pii/S1053811910012000

Johansen-Berg, H. and Behrens, T. (2009). *Diffusion MRI: from quantitative measurement to in-vivo neuroanatomy*. Academic Pr. ISBN 0123747090.

Johansen-Berg, H. and Behrens, T.E.J. (2006 August). Just pretty pictures? What diffusion tractography can add in clinical neuroscience. *Current opinion in neurology*, vol. 19, no. 4, pp. 379–85. ISSN 1350-7540.
Available at: http://www.ncbi.nlm.nih.gov/pubmed/16914977

Klein, A., Andersson, J., Ardekani, B.a., Ashburner, J., Avants, B., Chiang, M.-C., Christensen, G.E., Collins, D.L., Gee, J., Hellier, P., Song, J.H., Jenkinson, M., Lepage, C., Rueckert, D., Thompson, P., Vercauteren, T., Woods, R.P., Mann, J.J. and Parsey, R.V. (2009 July). Evaluation of 14 nonlinear deformation algorithms applied to human brain MRI registration. *NeuroImage*, vol. 46, no. 3, pp. 786–802. ISSN 1095-9572.
Available at: http://www.ncbi.nlm.nih.gov/pubmed/19195496

Klein, A., Ghosh, S.S., Avants, B., Yeo, B.T.T., Fischl, B., Ardekani, B., Gee, J.C., Mann, J.J. and Parsey, R.V. (2010 May*a*). Evaluation of volume-based and surface-based brain image registration methods. *NeuroImage*, vol. 51, no. 1, pp. 214–20. ISSN 1095-9572.
Available at: http://www.ncbi.nlm.nih.gov/pubmed/20123029

Klein, J., Grötsch, A., Betz, D., Barbieri, S., Friman, O., Stieltjes, B., Hildebrandt, H. and Hahn, H.K. (2010*b*). Qualitative and quantitative analysis of probabilistic and deterministic fiber tracking. *Progress in biomedical optics and imaging*, vol. 11, no. 33.
Available at: http://link.aip.org/link/PSISDG/v7623/i1/p76232A/s1&Agg=doi

Koga, T., Maruyama, K., Kamada, K., Ota, T., Shin, M., Itoh, D., Kunii, N., Ino, K., Terahara, A., Aoki, S., Masutani, Y. and Saito, N. (2011 January). Outcomes of Diffusion Tensor Tractography-Integrated Stereotactic Radiosurgery. *International journal of radiation oncology, biology, physics*, vol. In Press. ISSN 1879-355X.
Available at: http://www.ncbi.nlm.nih.gov/pubmed/21277103

Kroon, D.-J. (2008). B-spline grid, image and point based registration.
Available at: http://www.mathworks.com/matlabcentral/fileexchange/20057-b-spline-grid-image-and-point-based-registration

Kybic, J. and Unser, M. (2003 January). Fast parametric elastic image registration. *IEEE transactions on image processing : a publication of the IEEE Signal Processing Society*, vol. 12, no. 11, pp. 1427–42. ISSN 1057-7149.
Available at: http://www.ncbi.nlm.nih.gov/pubmed/18244700

Kyriacou, S.K., Davatzikos, C., Zinreich, S.J. and Bryan, R.N. (1999 July). Nonlinear elastic registration of brain images with tumor pathology using a biomechanical model. *IEEE transactions on medical imaging*, vol. 18, no. 7, pp. 580–92. ISSN 0278-0062.
Available at: http://www.ncbi.nlm.nih.gov/pubmed/10504092

Landis, J. and Koch, G. (1977). The measurement of observer agreement for categorical data. *Biometrics*, vol. 33, no. 1, p. 159. ISSN 0006-341X.
Available at: http://ukpmc.ac.uk/abstract/MED/843571

Lazar, M., Weinstein, D.M., Tsuruda, J.S., Hasan, K.M., Arfanakis, K., Meyerand, M.E., Badie, B., Rowley, H.a., Haughton, V., Field, A. and Alexander, A.L. (2003 April). White matter tractography using diffusion tensor deflection. *Human brain mapping*, vol. 18, no. 4, pp. 306–21. ISSN 1065-9471.
Available at: http://www.ncbi.nlm.nih.gov/pubmed/12632468

Le Bihan, D., Mangin, J.F., Poupon, C., Clark, C.A., Pappata, S., Molko, N. and Chabriat, H. (2001 April). Diffusion tensor imaging: concepts and applications. *Journal of magnetic resonance imaging : JMRI*, vol. 13, no. 4, pp. 534–46. ISSN 1053-1807.
Available at: http://www.ncbi.nlm.nih.gov/pubmed/11276097

Leemans, A. (2010). Theory and applications of diffusion MRI. In: *Biomedical Imaging: From Nano to Macro, 2010 IEEE International Symposium on*, pp. 628–631. IEEE. ISSN 1945-7928.
Available at: http://ieeexplore.ieee.org/xpls/abs_all.jsp?arnumber=5490100

Leemans, a., Sijbers, J., De Backer, S., Vandervliet, E. and Parizel, P. (2006 June). Multiscale white matter fiber tract coregistration: a new feature-based approach to align diffusion tensor data. *Magnetic resonance in medicine : official journal of the Society of Magnetic Resonance in Medicine / Society of Magnetic Resonance in Medicine*, vol. 55, no. 6, pp. 1414–23. ISSN 0740-3194.
Available at: http://www.ncbi.nlm.nih.gov/pubmed/16685732

Lindberg, P.v.G., Skejø, P.H.B., Rounis, E., Nagy, Z., Schmitz, C., Wernegren, H., Bring, A., Engardt, M., Forssberg, H. and Borg, J. (2007). Wallerian degeneration of the corticofugal tracts in chronic stroke: a pilot study relating diffusion tensor imaging, transcranial magnetic stimulation, and hand function. *Neurorehabilitation and neural repair*, vol. 21, no. 6, pp. 551–60. ISSN 1545-9683.
Available at: http://www.ncbi.nlm.nih.gov/pubmed/17507645

Maddah, M., Zollei, L., Grimson, W.E.L., Westin, C.-F. and Wells, W.M. (2008). A mathematical framework for incorporating anatomical knowledge in DT-MRI analysis. In: *5th IEEE Internation Symposium on Biomedical Imaging: From Nano to Macro*, 1, pp. 105–108.

Maintz, J. and Viergever, M.a. (1998 March). A survey of medical image registration. *Medical Image Analysis*, vol. 2, no. 1, pp. 1–36. ISSN 13618415.
Available at: http://linkinghub.elsevier.com/retrieve/pii/S1361841501800268

Mamata, H., Mamata, Y., Westin, C.-F., Shenton, M.E., Kikinis, R., Jolesz, F.a. and Maier, S.E. (2002 January). High-resolution line scan diffusion tensor MR imaging of white matter fiber tract anatomy. *AJNR. American journal of neuroradiology*, vol. 23, no. 1, pp. 67–75. ISSN 0195-6108.
Available at: http://www.pubmedcentral.nih.gov/articlerender.fcgi?artid=2845164&tool=pmcentrez&rendertype=abstract

Maudgil, D.D., Free, S.L., Sisodiya, S.M., Lemieux, L., Woermann, F.G., Fish, D.R. and Shorvon, S.D. (1998 November). Identifying homologous anatomical landmarks on reconstructed magnetic resonance images of the human cerebral cortical surface. *Journal of anatomy*, vol. 193, no. 4, pp. 559–71. ISSN 0021-8782.
Available at: http://www.pubmedcentral.nih.gov/articlerender.fcgi?artid=1467881&tool=pmcentrez&rendertype=abstract

Mayer, A. and Greenspan, H. (2008 May). Bundles of interest based registration of white matter tractographies. *2008 5th IEEE International Symposium on Biomedical Imaging: From Nano to Macro*, pp. 919–922.
Available at: http://ieeexplore.ieee.org/lpdocs/epic03/wrapper.htm?arnumber=4541147

Mazziotta, J., Toga, A., Evans, A., Fox, P., Lancaster, J., Zilles, K., Woods, R., Paus, T., Simpson, G., Pike, B., Holmes, C., Collins, L., Thompson, P., MacDonald, D., Iacoboni, M., Schormann, T., Amunts, K., Palomero-Gallagher, N., Geyer, S., Parsons, L., Narr, K., Kabani, N., Le Goualher, G., Boomsma, D., Cannon, T., Kawashima, R. and Mazoyer, B.

(2001 August). A probabilistic atlas and reference system for the human brain: International Consortium for Brain Mapping (ICBM). *Philosophical transactions of the Royal Society of London. Series B, Biological sciences*, vol. 356, no. 1412, pp. 1293–322. ISSN 0962-8436.
Available at: http://www.ncbi.nlm.nih.gov/pubmed/11545704

Merhof, D., Hastreiter, P., Soza, G., Stamminger, M. and Nimsky, C. (2004). Non-linear integration of DTI-based fiber tracts into standard 3D MR data. In: *Proc. Vision, Modeling, and Visualization (VMV)*, pp. 371–377.
Available at: http://sirl.stanford.edu/~{}bob/pdf/DTI/Methods/Merhof_epi_t1_warping_ProcVisModViz04.pdf

Mori, S. (2007). *Introduction to diffusion tensor imaging*. Elsevier Science Ltd. ISBN 0444528288.

Mori, S., Kaufmann, W., Davatzikos, C., Stieltjes, B., Amodei, L., Fredericksen, K., Pearlson, G., Melhem, E., Solaiyappan, M., Raymond, G. and Others (2002). Imaging cortical association tracts in the human brain using diffusion-tensor-based axonal tracking. *Magnetic resonance in medicine*, vol. 47, no. 2, pp. 215–223. ISSN 1522-2594.
Available at: http://onlinelibrary.wiley.com/doi/10.1002/mrm.10074/full

Mori, S., Oishi, K., Jiang, H., Jiang, L., Li, X., Akhter, K., Hua, K., Faria, A.V., Mahmood, A., Woods, R., Toga, A.W., Pike, G.B., Neto, P.R., Evans, A., Zhang, J., Huang, H., Miller, M.I., van Zijl, P. and Mazziotta, J. (2008 April). Stereotaxic white matter atlas based on diffusion tensor imaging in an ICBM template. *NeuroImage*, vol. 40, no. 2, pp. 570–82. ISSN 1053-8119.
Available at: http://www.pubmedcentral.nih.gov/articlerender.fcgi?artid=2478641&tool=pmcentrez&rendertype=abstract

Mori, S. and van Zijl, P.C.M. (2002). Fiber tracking: principles and strategies - a technical review. *NMR in biomedicine*, vol. 15, no. 7-8, pp. 468–80. ISSN 0952-3480.
Available at: http://www.ncbi.nlm.nih.gov/pubmed/12489096

Mori, S. and Zhang, J. (2006 September). Principles of diffusion tensor imaging and its applications to basic neuroscience research. *Neuron*, vol. 51, no. 5, pp. 527–39. ISSN 0896-6273.
Available at: http://www.ncbi.nlm.nih.gov/pubmed/16950152

Mukherjee, P., Berman, J.I., Chung, S.W., Hess, C.P. and Henry, R.G. (2008 April*a*). Diffusion tensor MR imaging and fiber tractography: theoretic underpinnings. *AJNR. American journal of neuroradiology*, vol. 29, no. 4, pp. 632–41. ISSN 1936-959X.
Available at: http://www.ncbi.nlm.nih.gov/pubmed/18339720

Mukherjee, P., Chung, S.W., Berman, J.I., Hess, C.P. and Henry, R.G. (2008 May*b*). Diffusion tensor MR imaging and fiber tractography: technical considerations. *AJNR. American journal of neuroradiology*, vol. 29, no. 5, pp. 843–52. ISSN 1936-959X.
Available at: http://www.ncbi.nlm.nih.gov/pubmed/18339719

Müller, H.-P., Unrath, A., Riecker, A., Pinkhardt, E.H., Ludolph, A.C. and Kassubek, J. (2009 April). Intersubject variability in the analysis of diffusion tensor images at the group level: fractional anisotropy mapping and fiber tracking techniques. *Magnetic resonance imaging*, vol. 27, no. 3, pp. 324–34. ISSN 1873-5894.
Available at: http://www.ncbi.nlm.nih.gov/pubmed/18701228

Nett, J. (2001). *The study of MS using MRI, image processing, and visualization*. Master's thesis, University of Louisville.

O'Donnell, L.J. and Westin, C.-F. (2007 November). Automatic tractography segmentation using a high-dimensional white matter atlas. *IEEE transactions on medical imaging*, vol. 26, no. 11, pp. 1562–75. ISSN 0278-0062.
Available at: http://www.ncbi.nlm.nih.gov/pubmed/18041271

Okada, T., Mikuni, N., Miki, Y., Kikuta, K.-I., Urayama, S.-I., Hanakawa, T., Fushimi, Y., Yamamoto, A., Kanagaki, M., Fukuyama, H., Hashimoto, N. and Togashi, K. (2006 September). Corticospinal tract localization: integration of diffusion-tensor tractography at 3-T MR imaging with intraoperative white matter stimulation mapping–preliminary results. *Radiology*, vol. 240, no. 3, pp. 849–57. ISSN 0033-8419.
Available at: http://www.ncbi.nlm.nih.gov/pubmed/16857980

Pasternak, O., Assaf, Y., Intrator, N. and Sochen, N. (2008 October). Variational multiple-tensor fitting of fiber-ambiguous diffusion-weighted magnetic resonance imaging voxels. *Magnetic resonance imaging*, vol. 26, no. 8, pp. 1133–44. ISSN 0730-725X.
Available at: http://www.ncbi.nlm.nih.gov/pubmed/18524529

Pollari, M., Neuvonen, T., Lilja, M. and Lotjonen, J. (2007). Comparative evaluation of voxel similarity measures for affine registration of diffusion tensor MR images. In: *Biomedical Imaging: From Nano to Macro, 2007. ISBI 2007. 4th IEEE International Symposium on*, pp. 768–771. IEEE. ISBN 1424406722.
Available at: http://ieeexplore.ieee.org/xpls/abs_all.jsp?arnumber=4193399

Reid, C. (1996). *A primer of human neuroanatomy*. 3rd edn. J. L. Van Schaik Academic, Pretoria, South Africa.

Rilling, J.K., Glasser, M.F., Preuss, T.M., Ma, X., Zhao, T., Hu, X. and Behrens, T.E.J. (2008 April). The evolution of the arcuate fasciculus revealed with comparative DTI. *Nature neuroscience*, vol. 11, no. 4, pp. 426–8. ISSN 1097-6256.
Available at: http://www.ncbi.nlm.nih.gov/pubmed/18344993

Rohde, G. (2005). *Registration Methods for Quantitative Imaging*. PhD Dissertation, University of Maryland.
Available at: http://hdl.handle.net/1903/2938

Rohr, K. (2003 May). Spline-based elastic image registration: integration of landmark errors and orientation attributes. *Computer Vision and Image Understanding*, vol. 90, no. 2, pp. 153–168. ISSN 10773142.
Available at: http://linkinghub.elsevier.com/retrieve/pii/S1077314203000481

Schlösser, R.G.M., Nenadic, I., Wagner, G., Güllmar, D., von Consbruch, K., Köhler, S., Schultz, C.C., Koch, K., Fitzek, C., Matthews, P.M., Reichenbach, J.R. and Sauer, H. (2007 January). White matter abnormalities and brain activation in schizophrenia: a combined DTI and fMRI study. *Schizophrenia research*, vol. 89, no. 1-3, pp. 1–11. ISSN 0920-9964.
Available at: http://www.ncbi.nlm.nih.gov/pubmed/17085018

Shadmi, R., Mayer, A., Sochen, N. and Greenspan, H. (2010). Piecewise smooth affine registration of point-sets with application to DT-MRI brain fiber-data. *2010 IEEE International Symposium on Biomedical Imaging: From Nano to Macro*, pp. 528–531.
Available at: http://ieeexplore.ieee.org/lpdocs/epic03/wrapper.htm?arnumber=5490292

Sherwood, L. (2005). *Fundamentals of physiology: a human perspective*. 3rd edn. Thomson Brooks/Cole.

Shoemake, K. and Duff, T. (1992). Matrix animation and polar decomposition. In: *Proceedings of the conference on Graphics interface*, vol. 92, pp. 258–264. Citeseer.
Available at: http://scholar.google.com/scholar?hl=en&btnG=Search&q=intitle:Matrix+Animation+and+Polar+Decomposition#0

Sullivan, E.V., Rohlfing, T. and Pfefferbaum, A. (2010 March). Quantitative fiber tracking of lateral and interhemispheric white matter systems in normal aging: relations to timed performance. *Neurobiology of aging*, vol. 31, no. 3, pp. 464–81. ISSN 1558-1497.
Available at: http://www.pubmedcentral.nih.gov/articlerender.fcgi?artid=2815144&tool=pmcentrez&rendertype=abstract

Sundgren, P.C., Dong, Q., Gómez-Hassan, D., Mukherji, S.K., Maly, P. and Welsh, R. (2004 May). Diffusion tensor imaging of the brain: review of clinical applications. *Neuroradiology*, vol. 46, no. 5, pp. 339–50. ISSN 0028-3940.
Available at: http://www.ncbi.nlm.nih.gov/pubmed/15103435

Talairach, J. and Tournoux, P. (1988). *Co-planar stereotaxic atlas of the human brain: 3-dimensional proportional system: an approach to cerebral imaging*. Thieme. ISBN 0865772932.

Teng, Y., Sullivan, F., Beichl, I. and Puppo, E. (1993). A data-parallel algorithm for three-dimensional Delaunay triangulation and its implementation. In: *Proceedings of the 1993 ACM/IEEE conference on Supercomputing*, pp. 112–121. ACM. ISBN 0818643404.
Available at: http://portal.acm.org/citation.cfm?id=169667

Thirion, B., Flandin, G., Pinel, P., Roche, A., Ciuciu, P. and Poline, J.-B. (2006 August). Dealing with the shortcomings of spatial normalization: multi-subject parcellation of fMRI datasets. *Human brain mapping*, vol. 27, no. 8, pp. 678–93. ISSN 1065-9471.
Available at: http://www.ncbi.nlm.nih.gov/pubmed/16281292

Thirion, J.-P. (1998 September). Image matching as a diffusion process: an analogy with Maxwell's demons. *Medical Image Analysis*, vol. 2, no. 3, pp. 243–260. ISSN 13618415.
Available at: http://linkinghub.elsevier.com/retrieve/pii/S1361841598800224

Tournier, J.-D., Calamante, F., Gadian, D.G. and Connelly, A. (2004 November). Direct estimation of the fiber orientation density function from diffusion-weighted MRI data using spherical deconvolution. *NeuroImage*, vol. 23, no. 3, pp. 1176–85. ISSN 1053-8119.
Available at: http://www.ncbi.nlm.nih.gov/pubmed/15528117

Tuch, D.S. (2004 December). Q-ball imaging. *Magnetic resonance in medicine : official journal of the Society of Magnetic Resonance in Medicine / Society of Magnetic Resonance in Medicine*, vol. 52, no. 6, pp. 1358–72. ISSN 0740-3194.
Available at: http://www.ncbi.nlm.nih.gov/pubmed/15562495

Voineskos, A.N., Donnell, L.J.O., Lobaugh, N.J., Markant, D., Ameis, S.H., Niethammer, M., Mulsant, B.H., Pollock, B.G., Kennedy, J.L., Westin, C.-F. and Shenton, M.E. (2009). NeuroImage Quantitative examination of a novel clustering method using magnetic resonance diffusion tensor tractography. *NeuroImage*, vol. 45, no. 2, pp. 370–376. ISSN 1053-8119.
Available at: http://dx.doi.org/10.1016/j.neuroimage.2008.12.028

Wakana, S., Caprihan, A., Panzenboeck, M., Fallon, J., Perry, M., Gollub, R., Hua, K., Zhang, J., Jiang, H., Dubey, P. and Others (2007). Reproducibility of quantitative tractography methods applied to cerebral white matter. *Neuroimage*, vol. 36, no. 3, pp. 630–644. ISSN 1053-8119.
Available at: http://linkinghub.elsevier.com/retrieve/pii/S1053811907001383

Wakana, S., Jiang, H., Nagae-Poetscher, L., Van Zijl, P.C.M. and Mori, S. (2004). Fiber Tract–based Atlas of Human White Matter Anatomy. *Radiology*, vol. 230, no. 1.

Wang, Y., Gupta, A., Liu, Z., Zhang, H., Escolar, M.L., Gilmore, J.H., Gouttard, S., Fillard, P., Maltbie, E., Gerig, G. and Styner, M. (2011 January). DTI registration in atlas based fiber analysis of infantile Krabbe disease. *NeuroImage*, vol. 19, pp. 1–10. ISSN 1095-9572.
Available at: http://www.ncbi.nlm.nih.gov/pubmed/21256236

Westin, C., Maier, S., Mamata, H., Nabavi, a., Jolesz, F. and Kikinis, R. (2002 June). Processing and visualization for diffusion tensor MRI. *Medical Image Analysis*, vol. 6, no. 2, pp. 93–108. ISSN 13618415.
Available at: http://linkinghub.elsevier.com/retrieve/pii/S1361841502000531

Xu, D., Mori, S., Shen, D., van Zijl, P.C.M. and Davatzikos, C. (2003 July). Spatial normalization of diffusion tensor fields. *Magnetic resonance in medicine : official journal of the Society of Magnetic Resonance in Medicine / Society of Magnetic Resonance in Medicine*, vol. 50, no. 1, pp. 175–82. ISSN 0740-3194.
Available at: http://www.ncbi.nlm.nih.gov/pubmed/12815692

Xue, Z., Li, H., Guo, L. and Wong, S.T.C. (2010 August). A local fast marching-based diffusion tensor image registration algorithm by simultaneously considering spatial deformation and tensor orientation. *NeuroImage*, vol. 52, no. 1, pp. 119–30. ISSN 1095-9572.
Available at: http://www.pubmedcentral.nih.gov/articlerender.fcgi?artid=2883676&tool=pmcentrez&rendertype=abstract

Yamada, K. (2009 February). Diffusion tensor tractography should be used with caution. *Proceedings of the National Academy of Sciences of the United States of America*, vol. 106, no. 7, p. E14; author reply E15. ISSN 1091-6490.
Available at: http://www.pubmedcentral.nih.gov/articlerender.fcgi?artid=2650181&tool=pmcentrez&rendertype=abstract

Yang, J., Shen, D., Davatzikos, C. and Verma, R. (2008 January). Diffusion tensor image registration using tensor geometry and orientation features. *Medical Image Computing and Computer-Assisted Intervention–MICCAI 2008*, vol. 11, no. Pt 2, pp. 905–13.
Available at: http://www.ncbi.nlm.nih.gov/pubmed/18982691

Yap, P., Wu, G., Zhu, H., Lin, W. and Shen, D. (2009). Fast Tensor Image Morphing for Elastic Registration. *Medical Image Computing and Computer-Assisted Intervention*, vol. 5761, pp. 721–729.
Available at: http://www.springerlink.com/index/8P132536156235T6.pdf

Yeo, B.T., Vercauteren, T., Fillard, P., Pennec, X., Golland, P., Ayache, N. and Clatz, O. (2008 May). DTI registration with exact finite-strain differential. *2008 5th IEEE International Symposium on Biomedical Imaging: From Nano to Macro*, vol. 3, no. 1, pp. 700–703.
Available at: http://ieeexplore.ieee.org/lpdocs/epic03/wrapper.htm?arnumber=4541092

Zitova, B. (2003 October). Image registration methods: a survey. *Image and Vision Computing*, vol. 21, no. 11, pp. 977–1000. ISSN 02628856.
Available at: http://linkinghub.elsevier.com/retrieve/pii/S0262885603001379

Ziyan, U., Sabuncu, M., O'Donnell, L. and Westin, C. (2007). Nonlinear registration of diffusion MR images based on fiber bundles. In: *Proceedings of the 10th international conference on Medical image computing and computer-assisted intervention-Volume Part I*, pp. 351–358. Springer-Verlag. ISBN 3540757562.
Available at: http://portal.acm.org/citation.cfm?id=1780201.1780249

Zöllei, L., Stevens, A., Huber, K., Kakunoori, S. and Fischl, B. (2010 May). Improved tractography alignment using combined volumetric and surface registration. *NeuroImage*, vol. 51, no. 1, pp. 206–13. ISSN 1095-9572.
Available at: http://www.pubmedcentral.nih.gov/articlerender.fcgi?artid=2847021&tool=pmcentrez&rendertype=abstract

Appendix A

Further Results

Experiment 1: FA-Based Nonlinear Registrations

Table A.1: Experiment 1: Improvement of FA image alignment after FA-based nonlinear base registration.

Brain	Cross Correlation	Mean Absolute Difference
1	0.24332	−0.030387
2	0.25546	−0.031387
3	0.18875	−0.021080
4	0.21440	−0.027975
5	0.23547	−0.027104
6	0.24779	−0.029577
7	0.21801	−0.025380
8	0.20052	−0.023120
10	0.20849	−0.022655
Mean	0.22358	−0.026519

Table A.2: Experiment 1: Improvement of bundle volume similarity after FA-based non-linear fibre registration. Mean values for all brains per bundle.

Bundle	Cross Correlation	Target Overlap	Source Overlap	Mutual Overlap	Union Overlap	Cohen's Kappa
ARC	−0.2075	−24.32%	07.23%	−26.06%	−15.79%	−0.2584
ATR	−0.2046	−37.91%	15.48%	−24.73%	−15.20%	−0.2466
CC1	−0.3208	−48.34%	13.48%	−39.99%	−28.12%	−0.3974
CC2	−0.3808	−51.91%	00.87%	−44.78%	−31.58%	−0.4442
CC3	−0.2242	−36.29%	08.53%	−27.64%	−17.56%	−0.2729
CIN1	−0.2075	−27.14%	02.04%	−24.63%	−14.78%	−0.2453
CIN2	−0.0922	−10.93%	07.07%	−11.10%	−06.14%	−0.1106
CFT	−0.2573	−42.50%	13.31%	−32.42%	−21.77%	−0.3222
IFO	−0.1912	−25.61%	04.87%	−23.68%	−14.24%	−0.2342
ILF	−0.2161	−25.41%	05.15%	−26.47%	−16.21%	−0.2630
SLF	−0.1003	−18.78%	−1.84%	−09.34%	−04.98%	−0.0930
STR	−0.2593	−33.76%	08.26%	−31.25%	−19.40%	−0.3116
UNC	−0.2787	−31.37%	−9.73%	−30.87%	−18.93%	−0.3080
Mean	−0.2262	−31.87%	05.75%	−27.15%	−17.28%	−0.2698

Table A.3: Experiment 1: Improvement of bundle volume similarity after FA-based non-linear fibre registration. Mean values for all bundles per brain.

Brain	Cross Correlation	Target Overlap	Source Overlap	Mutual Overlap	Union Overlap	Cohen's Kappa
1	−0.2415	−36.22%	06.13%	−28.83%	−18.61%	−0.2865
2	−0.2037	−30.10%	03.73%	−24.16%	−14.97%	−0.2397
4	−0.2587	−30.57%	00.77%	−30.14%	−19.29%	−0.3000
5	−0.1854	−31.78%	14.65%	−23.87%	−15.25%	−0.2369
6	−0.2454	−34.24%	−0.59%	−27.97%	−17.78%	−0.2780
7	−0.1728	−25.14%	09.99%	−21.97%	−13.54%	−0.2178
8	−0.2531	−34.60%	01.20%	−29.60%	−19.17%	−0.2944
9	−0.2694	−35.71%	−0.12%	−31.17%	−19.95%	−0.3101
10	−0.2059	−28.44%	15.97%	−26.65%	−17.01%	−0.2649
Mean	−0.2262	−31.87%	05.75%	−27.15%	−17.28%	−0.2698

Table A.4: Experiment 1: Improvement of bundle volume similarity after FA-based non-linear fibre with the source images downsampled. Mean values for all brains per bundle.

Bundle	Cross Correlation	Target Overlap	Source Overlap	Mutual Overlap	Union Overlap	Cohen's Kappa
ARC	0.0022	0.06%	0.83%	0.11%	0.06%	0.0011
ATR	0.0040	−0.01%	3.08%	0.01%	−0.01%	0.0001
CC1	0.0097	0.30%	3.14%	0.55%	0.30%	0.0055
CC2	−0.0295	−0.84%	−10.39%	−1.55%	−0.84%	−0.0156
CC3	0.0040	0.11%	1.44%	0.21%	0.11%	0.0021
CIN1	−0.0265	−0.66%	−10.87%	−1.24%	−0.65%	−0.0124
CIN2	0.0056	0.14%	1.96%	0.27%	0.13%	0.0027
CFT	0.0067	0.19%	2.30%	0.35%	0.19%	0.0035
IFO	−0.0129	−0.38%	−04.34%	−0.70%	−0.38%	−0.0071
ILF	−0.0049	−0.04%	−03.82%	−0.08%	−0.04%	−0.0008
SLF	−0.0174	−0.68%	−04.58%	−1.17%	−0.59%	−0.0117
STR	0.0063	0.13%	3.12%	0.25%	0.13%	0.0025
UNC	−0.0269	−0.57%	−12.97%	−1.08%	−0.56%	−0.0108
Mean	−0.0061	−0.17%	−02.39%	−0.31%	−0.16%	−0.0031

Table A.5: Experiment 1: Improvement of bundle volume similarity after FA-based non-linear fibre registration with the source images downsampled. Mean values for all bundles per brain.

Brain	Cross Correlation	Target Overlap	Source Overlap	Mutual Overlap	Union Overlap	Cohen's Kappa
1	−0.0088	−0.23%	−3.50%	−0.42%	−0.22%	−0.0042
2	−0.0075	−0.20%	−3.01%	−0.37%	−0.19%	−0.0037
4	−0.0180	−0.41%	−8.56%	−0.77%	−0.41%	−0.0077
5	0.0152	0.38%	6.49%	0.72%	0.38%	0.0072
6	−0.0251	−0.71%	−9.42%	−1.31%	−0.70%	−0.0131
7	0.0121	0.31%	4.65%	0.59%	0.31%	0.0059
8	−0.0183	−0.55%	−6.30%	−1.00%	−0.53%	−0.0100
9	−0.0226	−0.57%	−9.69%	−1.05%	−0.55%	−0.0105
10	0.0179	0.42%	7.80%	0.79%	0.41%	0.0079
Mean	−0.0061	−0.17%	−2.39%	−0.31%	−0.16%	−0.0031

Experiment 2: FA-Based Affine Registrations

Table A.6: Experiment 2: Improvement of FA image alignment after FA-based affine base registration.

Brain	Cross Correlation	Mean Absolute Difference
1	0.068812	−0.010262
2	0.065238	−0.010018
3	0.032330	−0.0032388
4	0.036002	−0.0030810
5	0.040629	−0.0071099
6	0.037230	−0.0052972
7	0.077872	−0.0087864
8	0.049517	−0.0051358
10	0.054084	−0.0044275
Mean	0.051302	−0.0063729

Table A.7: Experiment 2: Improvement of bundle volume similarity after FA-based affine fibre registration. Mean values for all brains per bundle.

Bundle	Cross Correlation	Target Overlap	Source Overlap	Mutual Overlap	Union Overlap	Cohen's Kappa
ARC	0.0667	5.01%	08.33%	06.61%	4.85%	0.0664
ATR	0.0484	2.86%	07.14%	04.67%	3.38%	0.0468
CC1	0.0638	3.65%	08.84%	06.40%	6.20%	0.0645
CC2	0.0657	3.68%	09.20%	06.51%	6.10%	0.0660
CC3	0.1084	9.62%	11.63%	10.85%	8.64%	0.1095
CIN1	0.0772	5.59%	10.20%	07.51%	5.31%	0.0753
CIN2	0.0878	9.32%	08.52%	08.63%	5.03%	0.0863
CFT	0.0683	4.68%	08.58%	06.94%	6.20%	0.0699
IFO	0.0360	2.59%	04.27%	03.71%	2.42%	0.0373
ILF	0.0873	8.47%	08.92%	08.69%	6.00%	0.0872
SLF	0.0287	1.47%	05.05%	02.53%	1.60%	0.0253
STR	0.0571	4.22%	07.35%	05.61%	4.26%	0.0562
UNC	0.0149	−0.30%	03.47%	01.40%	1.03%	0.0140
Mean	0.0623	4.68%	07.81%	06.16%	4.70%	0.0619

Table A.8: Experiment 2: Improvement of bundle volume similarity after FA-based affine fibre registration. Mean values for all bundles per brain.

Brain	Cross Correlation	Target Overlap	Source Overlap	Mutual Overlap	Union Overlap	Cohen's Kappa
1	0.0539	2.96%	07.68%	05.38%	4.21%	0.0542
2	0.0971	6.23%	13.16%	09.60%	7.57%	0.0966
3	0.0155	1.03%	02.01%	01.55%	1.43%	0.0156
4	0.0496	4.09%	06.09%	04.80%	3.53%	0.0482
5	0.0730	5.15%	09.26%	07.33%	5.38%	0.0737
6	0.0295	1.34%	04.49%	02.93%	2.55%	0.0295
7	0.1061	8.54%	13.02%	10.38%	7.50%	0.1043
8	0.0718	6.74%	07.69%	07.08%	5.29%	0.0711
10	0.0645	6.07%	06.86%	06.38%	4.81%	0.0640
Mean	0.0623	4.68%	07.81%	06.16%	4.70%	0.0619

Experiment 3: Volume-Based Local Affine Registrations

Table A.9: Experiment 3: Improvement of bundle volume similarity after volume-based local affine base registration. Mean values for all brains per bundle.

Bundle	Cross Correlation	Target Overlap	Source Overlap	Mutual Overlap	Union Overlap	Cohen's Kappa
ARC	0.1117	08.50%	13.74%	11.12%	08.40%	0.1117
ATR	0.1057	09.56%	11.03%	10.79%	08.18%	0.1081
CC1	0.0924	06.61%	11.46%	09.31%	09.24%	0.0938
CC2	0.0862	07.00%	09.80%	08.63%	08.22%	0.0874
CC3	0.1389	09.58%	17.57%	13.93%	11.29%	0.1407
CIN1	0.1504	12.42%	17.75%	14.93%	11.02%	0.1496
CIN2	0.2347	21.11%	25.17%	23.75%	15.31%	0.2376
CFT	0.0848	03.90%	12.52%	08.64%	07.78%	0.0870
IFO	0.0782	−0.01%	14.94%	07.98%	05.38%	0.0807
ILF	0.1134	06.15%	15.92%	11.53%	07.95%	0.1158
SLF	0.1458	15.50%	12.19%	15.16%	10.04%	0.1516
STR	0.1225	12.16%	12.23%	12.26%	09.53%	0.1228
UNC	0.1155	10.55%	12.45%	11.58%	09.25%	0.1159
Mean	0.1216	09.46%	14.37%	12.28%	09.35%	0.1233

Table A.10: Experiment 3: Improvement of bundle volume similarity after volume-based local affine base registration. Mean values for all bundles per brain.

Brain	Cross Correlation	Target Overlap	Source Overlap	Mutual Overlap	Union Overlap	Cohen's Kappa
1	0.0991	05.60%	13.60%	10.10%	07.95%	0.1015
2	0.1334	08.31%	18.02%	13.36%	10.44%	0.1343
3	0.1065	09.60%	10.66%	11.03%	08.75%	0.1106
4	0.1018	09.69%	10.26%	10.33%	07.74%	0.1036
5	0.1158	06.89%	15.85%	11.66%	08.72%	0.1172
6	0.0826	04.18%	11.86%	08.39%	06.64%	0.0844
7	0.1700	13.56%	20.04%	17.03%	12.11%	0.1710
8	0.1234	10.62%	13.87%	12.33%	09.40%	0.1238
10	0.1614	16.74%	15.13%	16.28%	12.44%	0.1631
Mean	0.1216	09.46%	14.37%	12.28%	09.35%	0.1233

Table A.11: Experiment 3: Improvement of bundle volume similarity after volume-based local affine fibre registration. Mean values for all brains per bundle.

Bundle	Cross Correlation	Target Overlap	Source Overlap	Mutual Overlap	Union Overlap	Cohen's Kappa
ARC	0.1269	10.73%	14.51%	12.66%	09.68%	0.1271
ATR	0.1064	09.42%	11.46%	10.79%	08.20%	0.1081
CC1	0.1033	08.17%	12.06%	10.39%	10.42%	0.1047
CC2	0.0915	07.68%	10.19%	09.16%	08.76%	0.0926
CC3	0.1535	12.30%	17.76%	15.38%	12.60%	0.1553
CIN1	0.1603	13.69%	18.48%	15.91%	11.85%	0.1594
CIN2	0.2434	24.08%	24.49%	24.35%	15.79%	0.2436
CFT	0.1011	06.57%	13.11%	10.25%	09.36%	0.1032
IFO	0.1070	05.52%	14.93%	11.01%	07.59%	0.1108
ILF	0.1389	10.32%	16.79%	14.11%	09.93%	0.1416
SLF	0.1160	10.48%	12.37%	11.66%	07.72%	0.1166
STR	0.1326	12.83%	13.60%	13.26%	10.36%	0.1329
UNC	0.1205	11.01%	13.01%	12.06%	09.68%	0.1207
Mean	0.1309	10.98%	14.83%	13.15%	10.15%	0.1321

Table A.12: Experiment 3: Improvement of bundle volume similarity after volume-based local affine fibre registration. Mean values for all bundles per brain.

Brain	Cross Correlation	Target Overlap	Source Overlap	Mutual Overlap	Union Overlap	Cohen's Kappa
1	0.1187	09.06%	14.06%	12.06%	09.61%	0.1212
2	0.1483	11.48%	17.80%	14.86%	11.75%	0.1493
3	0.1166	10.33%	12.35%	11.85%	09.57%	0.1189
4	0.0997	09.08%	10.63%	10.02%	07.65%	0.1005
5	0.1310	09.87%	15.83%	13.22%	10.09%	0.1328
6	0.0960	06.62%	12.18%	09.71%	07.76%	0.0975
7	0.1768	14.89%	20.36%	17.59%	12.66%	0.1766
8	0.1319	12.13%	14.10%	13.16%	10.10%	0.1321
10	0.1588	15.41%	16.15%	15.90%	12.14%	0.1594
Mean	0.1309	10.98%	14.83%	13.15%	10.15%	0.1321

Experiment 4: Volume-Based Global Affine Registrations

Table A.13: Experiment 4: Improvement of bundle volume similarity after volume-based global affine base registration.

Brain	Cross Correlation	Target Overlap	Source Overlap	Mutual Overlap	Union Overlap	Cohen's Kappa
1	0.0081	−6.97%	07.33%	0.89%	0.83%	0.0118
2	0.0878	−0.04%	15.92%	8.39%	8.07%	0.0901
3	0.0189	1.54%	02.09%	1.81%	1.72%	0.0189
4	0.0331	3.65%	02.71%	3.25%	2.98%	0.0334
5	0.0453	−0.32%	08.14%	4.49%	4.31%	0.0483
6	0.0449	−0.97%	09.01%	4.30%	4.21%	0.0464
7	0.0502	0.32%	09.15%	4.56%	4.00%	0.0493
8	0.0211	0.54%	03.38%	1.99%	1.81%	0.0213
10	0.0202	3.87%	−0.07%	2.14%	2.00%	0.0215
Mean	0.0366	0.18%	6.41%	3.54%	3.33%	0.0379

Table A.14: Experiment 4: Improvement of bundle volume similarity after volume-based global affine fibre registration. Mean values for all brains per bundle.

Bundle	Cross Correlation	Target Overlap	Source Overlap	Mutual Overlap	Union Overlap	Cohen's Kappa
ARC	0.0565	04.22%	07.11%	05.58%	04.04%	0.0561
ATR	0.0393	02.09%	06.00%	03.80%	02.72%	0.0381
CC1	0.0290	00.35%	05.19%	02.96%	02.84%	0.0300
CC2	0.0437	01.64%	06.87%	04.35%	04.10%	0.0442
CC3	0.0929	07.97%	10.13%	09.35%	07.35%	0.0944
CIN1	0.0120	−0.20%	02.81%	01.08%	00.63%	0.0108
CIN2	0.0834	08.68%	08.35%	08.16%	04.96%	0.0817
CFT	0.0508	02.78%	06.96%	05.21%	04.57%	0.0525
IFO	0.0377	02.68%	04.49%	03.89%	02.55%	0.0391
ILF	0.0661	06.22%	06.91%	06.60%	04.51%	0.0663
SLF	0.0293	01.34%	05.41%	02.55%	01.53%	0.0255
STR	0.0414	02.82%	05.60%	04.05%	03.00%	0.0406
UNC	−0.0041	−1.94%	01.29%	−0.50%	−0.42%	−0.0050
Mean	0.0445	02.97%	05.93%	04.39%	03.26%	0.0442

Table A.15: Experiment 4: Improvement of bundle volume similarity after volume-based global affine fibre registration. Mean values for all bundles per brain.

Brain	Cross Correlation	Target Overlap	Source Overlap	Mutual Overlap	Union Overlap	Cohen's Kappa
1	−0.0053	−3.71%	02.43%	−0.49%	−0.23%	−0.0046
2	0.0943	05.78%	13.08%	09.31%	07.25%	0.0937
3	0.0268	02.30%	03.25%	02.59%	02.03%	0.0260
4	0.0431	03.98%	04.75%	04.23%	03.05%	0.0424
5	0.0672	04.80%	08.45%	06.74%	04.90%	0.0677
6	0.0325	01.30%	05.22%	03.17%	02.49%	0.0320
7	0.0613	04.25%	08.16%	06.00%	04.25%	0.0603
8	0.0136	01.08%	01.66%	01.32%	00.87%	0.0134
10	0.0668	06.96%	06.39%	06.66%	04.73%	0.0667
Mean	0.0445	02.97%	05.93%	04.39%	03.26%	0.0442